UNIVERSITÀ
DEGLI STUDI
DI PADOVA

Sede Amministrativa: Università degli Studi di Padova

Dipartimento di Ingegneria Industriale

SCUOLA DI DOTTORATO DI RICERCA IN INGEGNERIA INDUSTRIALE
INDIRIZZO: INGEGNERIA CHIMICA, DEI MATERIALI E MECCANICA
CICLO XXIX

X-ray computed tomography for coordinate metrology and industrial applications

Direttore della Scuola: Ch.mo Prof. Paolo Colombo
Coordinatore d'indirizzo: Ch.mo Prof. Giovanni Meneghetti
Supervisore: Ch.mo Prof. Simone Carmignato
Co-supervisore: Ch.mo Prof. Enrico Savio

Dottorando: Filippo Zanini

Tre anni

Three years

Abstract

X-ray computed tomography (CT) has emerged as innovative measuring technique for dimensional metrology in industry over the last years. Thanks to unique capabilities, CT provides several advantages in comparison with other well-established coordinate measuring systems (CMSs). In particular, CT allows obtaining a holistic three-dimensional model of the scanned workpiece and performing non-destructive and non-contact measurements of outer as well as inner features and geometries difficult to access. However, important drawbacks limit a wider acceptance of this technology in industry. One of the most critical problems is the complexity of metrological traceability establishment due to difficulties in evaluating the task-specific uncertainty, as well as specification and determination of metrological performances of CT systems. In fact, a dedicated international standard for CT acceptance test and performance verification is still under development.

In this thesis, experimental activities were mainly oriented at evaluating and improving CT metrological performances. The material influence on length measurement errors was studied by investigations based on two reference objects: aluminium hole plate, with significant material effect and ruby ball plate, with negligible material influence. The obtained results contributed to the test survey organized on this topic by the ISO working group that is developing the future ISO standard for CT.

The image quality of the 2D projections acquired by CT is fundamental for achieving a good reconstruction quality. It is directly connected to the image blurring content and, consequently, to the focal spot quality. In this thesis, new methods developed to assess the focal spot drift and size are presented.

Considering the entire CT measurement procedure, an important metrological characteristic to be evaluated is the metrological structural resolution (MSR). Despite several methods for MSR evaluation have been proposed, a standard test to be included in the ISO standard for CT has still to be defined. In this thesis, the 'Hourglass' method – developed by the University of Padova– was selected to evaluate the MSR. The method was improved by measuring a high number of distances and by applying a definition of

MSR similar to the one proposed by the guideline VDI/VDE 2617-13. Moreover, the method concept was compared with concepts of other proposed methods. Finally, the main influence quantities affecting the method were identified and evaluated.

Since CT is a multi-purpose measuring technique, it has become attractive for many industrial applications. However, the accuracy of CT measurement results is often unknown. For this reason, the evaluation of CT accuracy for specific measurement tasks as well as the comparison with other well-established evaluation methods is crucial for the acceptance of CT in industry. In this thesis, two industrial case studies were addressed: (i) porosity analysis for metal additive manufactured parts and (ii) wear evaluation of polymeric prosthetic components. In the first study, CT was compared with other inspection techniques such as Archimedes method, gas pycnometry and microscopic analysis of cross-sections. A multisensory CMM was used as well in order to get reliable reference area values for pores lying on selected cut sections. In the second study, the proposed CT-based method was validated through comparison with the gravimetric method, which is the current reference method used for wear assessment.

Sommario

La tomografia computerizzata a raggi-X (CT) si è affermata negli ultimi anni come tecnologia di misura innovativa per la metrologia dimensionale nel settore industriale. L'utilizzo di un sistema CT industriale comporta una serie di importanti vantaggi nei confronti di altri sistemi di misura a coordinate (CMSs). In particolare, il CT consente di ottenere un modello tridimensionale completo dell'oggetto scansionato e di condurre misure non distruttive e non a contatto di geometrie e caratteristiche sia esterne sia interne e di difficile accesso. Tuttavia, alcuni svantaggi rilevanti limitano una più estesa diffusione di questa tecnologia nel settore industriale. Uno dei problemi più critici risiede nella riferibilità metrologica delle misure CT, complicata dalla difficoltà nel determinare l'incertezza di misura e nel valutare le prestazioni metrologiche dei sistemi CT. Inoltre, uno standard internazionale dedicato ai test per l'accettazione e per la verifica delle prestazioni dei sistemi CT è tuttora in via di sviluppo.

Le attività sperimentali presentate in questo lavoro di tesi sono state focalizzate principalmente sulla valutazione e sul miglioramento delle prestazioni metrologiche del CT. L'influenza del materiale sugli errori di misura di lunghezza è stata studiata mediante indagini basate su due campioni di riferimento: una *hole plate* di alluminio, caratterizzata da un'influenza significativa del materiale e una *ball plate* di rubino, caratterizzata da un'influenza del materiale trascurabile. I risultati ottenuti hanno contribuito alla campagna sperimentale incentrata su questo argomento organizzata dal *working group* dedicato allo sviluppo del futuro standard ISO per il CT.

La qualità d'immagine delle proiezioni radiografiche bidimensionali acquisite mediante CT è fondamentale per ottenere una buona qualità nella ricostruzione del modello tridimensionale dell'oggetto scansionato. Essa è connessa al concetto di *blurring* o sfocatura dell'immagine e, di conseguenza, alla qualità della macchia focale da cui viene emesso il fascio di raggi X. All'interno di questa tesi vengono descritti nuovi metodi sviluppati per valutare l'effettiva dimensione della macchia focale e l'eventuale *drift* che essa può subire durante una scansione tomografica.

Considerando l’intera procedura di misura CT, una caratteristica metrologica molto importante da considerare è la risoluzione strutturale metrologica (MSR). Nonostante siano stati proposti diversi metodi per la valutazione della MSR, un test univoco da includere nel futuro standard ISO dedicato al CT deve ancora essere definito. In questa tesi, il metodo ‘Hourglass’ – sviluppato dall’Università di Padova - è stato selezionato per valutare la MSR. Questo metodo è stato migliorato mediante la misura di un elevato numero di distanze e applicando una definizione di MSR simile a quella proposta dalla linea guida tedesca VDI/VDE 2617-13. Inoltre, il concetto alla base di tale metodo è stato confrontato con quello di altri metodi e i principali fattori che possono influenzarne i risultati sono stati identificati e valutati.

Essendo la tomografia computerizzata a raggi-X una tecnica di misura molto versatile, il suo potenziale può essere sfruttato da un gran numero di applicazioni industriali. Tuttavia, l’accuratezza dei risultati di misura CT è spesso ignota. Per questa ragione, la determinazione dell’accuratezza di misura e il confronto con altri metodi di misura consolidati sono cruciali per una piena accettazione del CT in ambito industriale. In questa tesi sono stati affrontati due casi di rilevanza industriale: (i) analisi di porosità su componenti metallici realizzati mediante produzione additiva e (ii) determinazione dell’usura di componenti protesiche in polietilene. Per quanto riguarda il primo studio, il CT è stato confrontato con altre tecniche d’indagine: metodo di Archimede, picnometro a gas e analisi microscopica di sezioni di taglio. In aggiunta, una macchina di misura a coordinate (CMM) multi-sensore è stata utilizzata per ottenere valori di riferimento per l’area di un certo numero di pori distribuiti su alcune sezioni di taglio selezionate. Nel secondo studio, il metodo CT proposto è stato validato mediante confronto con il metodo gravimetrico, che è l’attuale metodo di riferimento utilizzato per la determinazione del grado di usura.

List of contents

Chapter 1

Introduction

This chapter provides a brief introduction of X-ray Computed Tomography (CT), an innovative measuring technique which has become widely used for dimensional metrology in industry. Furthermore, the main objectives of the PhD project were presented, followed by description of the used instrumentation. Finally, the thesis structure is outlined.

1.1 Brief introduction on X-ray computed tomography

In the current industrial environment, advanced and innovative manufacturing technologies such as additive manufacturing of high-complex customized parts, production of composite materials and micro-manufacturing are growing fast. This is elevating the requirements for production engineering in terms of quality and precision. In this context, metrology has the fundamental role to provide adequate instruments and procedures for quality control, necessary for the establishment of the aforementioned technologies. In particular, specific measurement tests are fundamental for a complete assessment of parts functionalities, e.g. measurement of internal geometries and features, detection and evaluation of internal defect volume and distribution, fiber length, orientation and distribution in composite materials, analysis of assembly. For these reasons, quality control is still a major challenge that has to be overcome, for example by new measuring solutions and technologies. X-ray computed tomography (CT), developed in the 1970s for medical application and then employed in non-destructive testing of materials, has recently emerged as advanced measuring technique used for geometrical and dimensional metrology. Thanks to its unique capabilities, CT has a series of important advantages allowing performing analyses that are difficult or impossible to be performed by means of other well-established measuring instruments, such as tactile and optical coordinate measuring systems (CMSs). In particular, CT has the capability of measuring internal not accessible features and geometries, freeform surfaces and complex geometries, undercuts, contact surfaces of assembled parts, samples of any material (even transparent or reflective), delicate or fragile parts and objects that cannot be measured by means of contact devices. However, CT systems are still far to be wide accepted in industry for quality control and dimensional measurement applications, because of some relevant limitations. The main critical aspects are: (i) CT measurement accuracy is affected by many influence factors which are often difficult to be assessed, (ii) the metrological traceability establishment is still challenging and (iii) high costs in terms of measuring equipment and software for data reconstruction and elaboration.

1.2 PhD project

The general aim of this PhD research project was to carry out studies in the field of industrial Computed Tomography (CT) for coordinate metrology to contribute to a wider acceptance in industry of CT as innovative tool for industrial dimensional quality control, as well as to overcome some existing limitations, through experimental research and international collaborations.

The PhD project was financed by the “Precision manufacturing engineering group” operating at the University of Padova. The CT system used during the entire project was a Nikon X-Tek MCT225, installed at Te.Si. Lab. (University of Padova). The main scientific domains of the lab are: geometrical metrology, additive manufacturing, injection molding and micro-injection molding, precision and micro-machining. In this context, the project could benefit of collaborations with other researchers working at the University of Padova, with manufacturing companies and with other national and international institutions.

1.3 Problem identification

CT is recently emerging as innovative tool in the field of coordinate metrology, featuring relevant advantages in comparison with conventional measuring systems. Nevertheless, CT has still important limitations. In first place, the accuracy of CT data is affected by many influence quantities, whose impact on measurement results is often difficult to be quantified. This fact, combined with the versatility of CT as measuring technique, causes the task-specific uncertainty to be difficult to be properly determined by the users. In addition, verification and improvement of metrological performance is of great importance, but a CT-dedicated international standardization is still under development. Consequently, metrological traceability of CT to the length unit is still a challenge. The first need is to make a step forward toward the accomplishment of an international standard, by means of specific tests oriented at improving acceptance and verification tests as well as the understanding of influence quantities. With this view, this project has dealt with experimental tests aimed at assessing the material influence on length measurement errors. Moreover, metrological structural resolution is a characteristic that will be included in the future ISO standard for CT, but a standard procedure for its evaluation has not been defined yet. In this thesis, the ‘Hourglass’ method - developed at the University of Padova – was studied and improved to be a valid proposal worth to be considered for the standard. As said above, CT is a versatile multi-purpose system allowing the most disparate analysis to be addressed, with attractive outcomes for several industrial fields. However, the accuracy of such results as well as the CT comparability with other well-established techniques are often difficult to be assessed. On one side, accuracy and comparability concerning simple dimensional measurements (lengths, diameters) can be studied in a relative simple way, e.g. by means of calibrated reference objects. On the other side, for more complex measurements both accuracy and comparability with other techniques are more challenging. This is, for example, the case of volume measurements that are often performed with CT, e.g. when measuring pores/voids volume or wear rate. In this project, two applications requiring volume measurements are investigated: (i) porosity analysis of additive manufactured parts and (ii) wear evaluation of prosthetic hip joint inserts. The first study concerns the accuracy of CT porosity analysis, assessed through comparison with Archimedes method and microscopic analysis of cross-sections. The second study proposes a CT-based method for wear evaluation, validated through comparison with the gravimetric method. In this case, CT was selected as the most suited technique able to provide both volumetric wear assessment and local distribution of wear without inducing any damage or deformation to the object.

1.4 Instrumentation used

1.4.1 Hardware

Nikon X-Tek MCT225

The Nikon X-Tek MCT225 [1] is a metrological micro-CT system which was used during the entire PhD project. A metrological system has the possibility to combine non-destructive material evaluations and accurate dimensional measurements. This is made possible by specific hardware and software improvements, such as the thermally-controlled cabinet, the presence of high-precision guideways, the higher stability over time, the liquid-cooled X-ray gun and the accuracy specification stated by the manufacturer. The main specs of the MCT225 are reported in Figure 1.1.

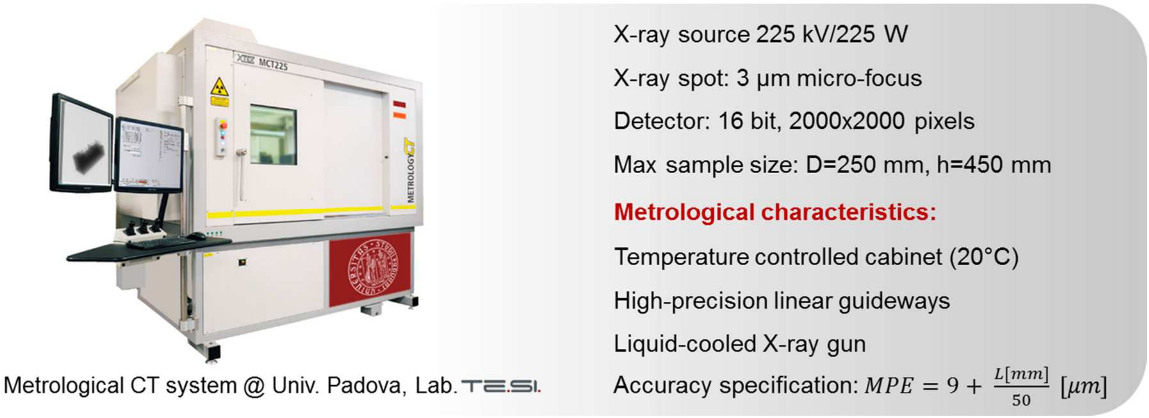

Metrological CT system @ Univ. Padova, Lab. TE.SI.

X-ray source 225 kV/225 W

X-ray spot: 3 µm micro-focus

Detector: 16 bit, 2000x2000 pixels

Max sample size: D=250 mm, h=450 mm

Metrological characteristics:

Temperature controlled cabinet (20°C)

High-precision linear guideways

Liquid-cooled X-ray gun

Accuracy specification: $MPE = 9 + \frac{L[mm]}{50}\ [\mu m]$

Figure 1.1: Technical specifications of Nikon X-Tek MCT225 installed at the University of Padova.

1.4.2 Software

CT data reconstruction was performed using the software CT Pro 3D provided by Nikon Metrology with the system.

CT data elaborations were conducted by means of the commercially available software VGStudio MAX (Volume Graphics GmbH, Austria) [2]. This is the most used software capable of treating directly voxel volumes, with no need of a surface model (e.g. STL format) to be extracted. This is important, since the extraction procedure can introduce additional errors to the measurement. Several modules are available: coordinate measurements, nominal/actual comparison, wall thickness analysis, defect detection and fiber orientation analysis, covering most of the industrial needs.

Simulations of CT scans were performed with Scorpius XLab (Fraunhofer IIS, Germany) [3].

1.5 Thesis structure

In the following, the content of each chapter of this thesis is briefly described:

- **Chapter 2** introduces the historical background of X-ray Computed Tomography for dimensional measurements, describes the main hardware components, the measurement procedure of a typical industrial CT system and presents an overview of industrial applications.

- **Chapter 3** discusses metrological traceability of CT. In particular, current tests for CT performance verification and methods for uncertainty determination are presented. Moreover, descriptions of the main factors influencing CT performances and of reference objects suited for CT are provided.

- **Chapter 4** presents tests conducted within the ISO TC 213 WG 10 experimental study on material influence in dimensional computed tomography. The main intent of this study is to demonstrate if there are major additional length measurement errors resulting from material effect that are not covered by the current testing procedure using hole plate measurements.

- **Chapter 5** deals with the image quality of 2D acquired projection images and with the metrological structural resolution (MSR). In particular, focal spot drift and size were evaluated and the 'Hourglass' method for MSR evaluation was improved and compared with other proposed methods. Finally, influence factors affecting the 'Hourglass' method were identified and quantified.

- **Chapter 6** concerns an experimental research work done in collaboration with the University of Twente, Netherland. Experimental analysis performed on Ti6Al4V SLM specimens were aimed at evaluating the accuracy of CT porosity analysis through comparison with well-established inspection techniques, such as Archimedes method, gas pycnometer and microscopic analysis of cross-sections. Influence factors affecting CT porosity analysis were identified and sphericity was investigated as morphology descriptor.

- **Chapter 7** presents an experimental research work done in collaboration with the "Istituto Ortopedico Rizzoli" (IOR), orthopedic institute in Bologna, Italy. The main objective was to develop a CT-based method for wear evaluation of polyethilene's hip joint prosthetic components.

- **Chapter 8** reports the main conclusions and final remarks about the PhD project.

Chapter 2

X-ray computed tomography for dimensional measurements

This chapter introduces the historical background of X-ray Computed Tomography for dimensional measurements, describes the main hardware components and the measurement procedure of a typical industrial CT system and presents and overview of the most typical industrial applications.

2.1 Historical background of computed tomography

In late 1895, a German physicist, W. C. Roentgen was working on experiments with accelerated electrons. After creating the vacuum inside a cathode ray tube, he passed a high electric voltage through it, producing a fluorescent glow on a phosphored screen located at a short distance from the tube. He realized that he had discovered radiation with the ability to penetrate optically opaque objects, which he named X-rays [4]. Roentgen experiments proved that X-rays can pass through biological tissue, showing bones and tissues in the human body. The first X-ray image (radiograph) was generated one year after by Michael Pupin [5]. X-ray radiation is of electromagnetic nature and its wavelength ranges between 0.01 nm and 10 nm (Figure 2.1). The energy of each photon E is proportional to its frequency f, so a smaller wavelength corresponds to a higher energy:

$$E = h \cdot f = \frac{h \cdot c}{\lambda} \tag{2.1}$$

where h is Planck's constant (6.63 × 10–34 Js), c is the speed of light (3 × 108 ms^{-1}), and λ is the wavelength of the X-ray [6].

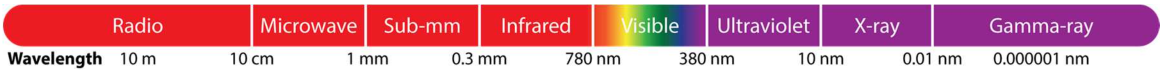

Figure 2.1: Electromagnetic spectrum.

The conventional X-ray imaging (radiography technique), applied especially in the medical field, suffered from the intrinsic drawback of producing two-dimensional (2D) projections of a three-dimensional (3D) object. This results in a reduction in spatial information, which limits clinical diagnostic capability.

In the 1920s, several scientific discoveries allow overcoming this limitation and led to the first tomographic concept: the cross sectional imaging of a sample can be derived from data obtained from many different angular directions. The term *tomography* derived from two Greek words: *tomos* which means section or cutting and *graphien* which means to write. As visible in Figure 2.2, the history of Computed Tomography (CT) started very recently. In 1917, an Australian mathematicians, J. Radon proved that an object can be reproduced by a set of its own projections (Radon's transformation). In 1967, the filtered backprojection algorithm (see Section 2.3) was introduced by Bracewell and Riddle. Hounsfield and Cormack in 1970 were able to replace X-ray sensitive films by an electric

X-ray detector [7]. Thanks to developments in sensor technology, the first clinical CT scanner was realized by EMI Laboratories in 1972 and named *EMI Scanner*. The first scan of an entire human body was achieved in 1976 [8].

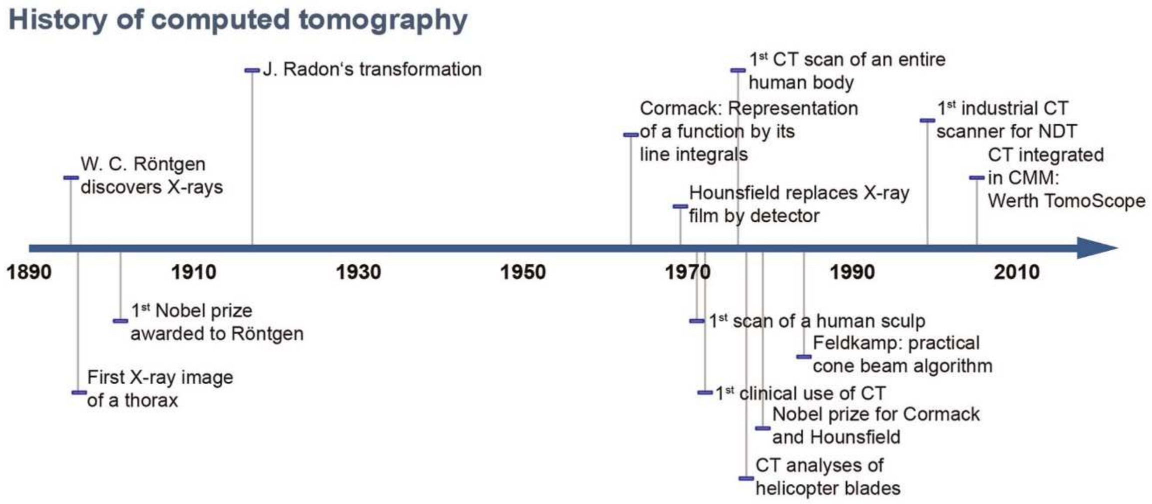

Figure 2.2 – Timeline/History of CT [8]

In the 80's, advanced micro-focus X-ray CT based on the same principles of medical CT was developed and thanks to the better attention given to the pixel resolution and to the accuracy, computed tomography started to be used also in industry. In particular, CT systems became popular for material analysis and *Non-Destructive Testing* (NDT): e.g. for qualitative observation of the inner structure of materials (e.g. fiber-reinforced plastics) and detection of material defects. The first industrial use of CT for NDT purposes goes back to 1978 with a medical CT system. In this occasion, helicopter rotors have been scanned [9].

More recently, CT has emerged as measuring instrument used in the field of coordinate metrology as alternative to tactile or optical 3D coordinate measuring systems (CMSs). The first attempts to perform dimensional measurements using existing CT scanners appeared around 1991 [10, 11], but the accuracy was not satisfactory (around 0.1 mm). Later, in 2005, the first CT system dedicated to dimensional measurements was produced [12].

2.2 Description of industrial CT systems

A typical industrial CT system is generally characterized by three main hardware components: X-ray source, X-ray detector and kinematic systems. Moreover, CT specific software is needed for 3D reconstruction and edge detection as well as for dimensional analysis.

The most common configurations of industrial CT are shown in Figure 2.3. The fan-beam configuration features a line detector (1D - detector), while the cone-beam configuration mounts a flat panel detector (2D - detector) and allows circular or helical trajectories.

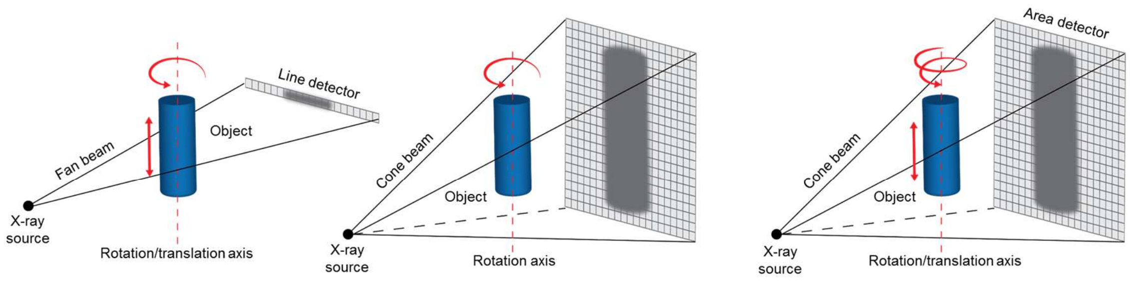

(a) Fan-beam configuration

(b) Cone-beam configuration
Circular trajectory

(c) Cone-beam configuration
Helical trajectory

Figure 2.3: CT scan configurations.

In the following, the main hardware components of industrial CT systems are described:

2.2.1 X-ray source

The X-ray source is one of the most important parts of a CT systems since it strongly influences the image quality of the acquired two-dimensional projections of the scanned object. As illustrated in Figure 2.4, the X-ray source (vacuum tube) consists of a negatively charged cathode and a positively charged anode, containing a metal target. Electrons are emitted from the cathodic filament (usually a tungsten wire) and, subsequently, accelerated toward the anode. To produce a small electron focus on the target, necessary to obtain high image quality (i.e. sharp instead of blurred images), the electron beam must be controlled in convergence and intensity by magnetic deflectors and lenses. When hitting the target, the fast electrons are suddenly decelerated and 99% of their energy results to be converted into heat while only 1% into X-rays. The X-ray beam, right before its emission, is usually collimated by passing through a circular aperture (for conical beams) or collimating plates (for fan beams). A window made by beryllium or aluminum seals this aperture for maintaining the vacuum inside the tube. The emitted X-rays consist of two components:

Brehmsstrahlung or continuous radiation and Characteristic radiation. *Brehmsstrahlung* comes from the German word ”Bremse” meaning slowing down. Brehmsstrahlung radiation is the dominant X-ray production process and generates a continuous spectrum when incoming electrons hit atomic nuclei in the target. X-rays are released as the electrons are decelerated. Characteristic radiation occurs when an incoming electron collides and excites an inner-shell electron in an atom of the target: the hit electron leaves a vacancy in one of the atom’s electron shells and another electron may fill the vacancy releasing the Characteristic radiation characterized by a discrete spectrum. Both radiation types are shown in figure 2.5.

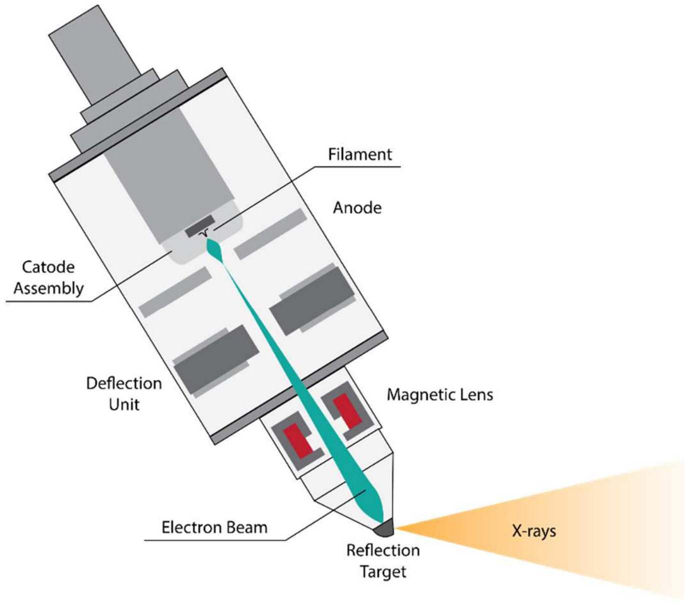

Figure 2.4: Typical X-ray source for cone-beam CT with reflection target.

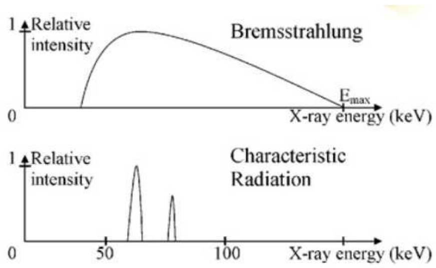

Figure 2.5: Bremsstrahlung and Characteristic radiations [12].

The energy spectrum defines the penetrative ability of the X-rays, as well as their expected relative attenuation as they pass through materials of different density [13]. The X-ray energy spectrum is affected by: voltage, current, filtration and target material. X-ray source current and voltage have to be chosen by the CT user taking into consideration that while the acceleration voltage determines the energy interval of the X-ray spectrum (higher-energy X-rays penetrate more effectively than lower-energy ones), the intensity of the generated X-ray spectrum (affecting the signal-to-noise ratio, SNR, and thus image brightness) is only controlled by the anode current. Beam filtration can be introduced for selectively removing low-energy X-rays (i.e. harden the spectrum) and consequently reducing an effect called beam hardening (see Section 3.3), typical of CT scans. Filters can be made by different materials such as copper, aluminum, brass, etc. Their effect is increasing the average energy of the X-ray beam with an improvement of quality (see Figure 2.6-a). The drawback is that the total amount of X-rays is decreased leading to a worst image SNR. The target can be made from different material as well, producing different X-ray radiation spectra (Figure 2.6-b). For example, high atomic number elements like tungsten (Z = 74) enable to reach higher penetration. Moreover, the target can be: (i) transmitting target, used only when low power CT sources are involved because of the low resistance to high temperatures, (ii) reflective target, usually combined with high power CT sources and equipped with water cooling systems, (iii) high-precision rotating target, used to spread the heat input over a larger area, (iv) multi-material target, to allow easy multi-spectra measurements.

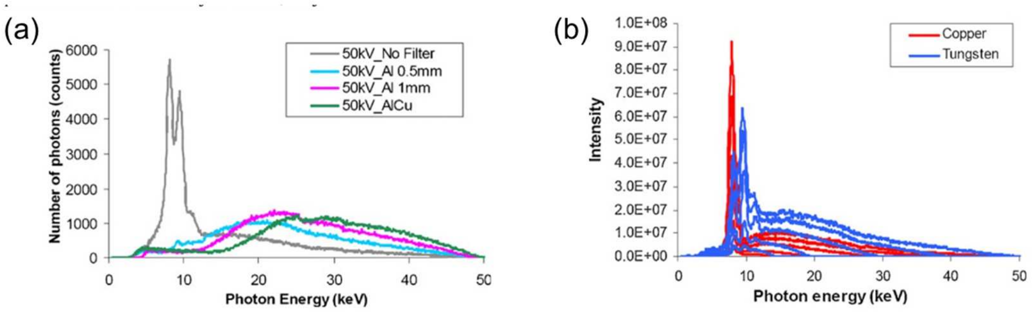

Figure 2.6: Spectra for 50 kV source before and after passing various filters (a) and spectra of Cu and W targets from 15 to 50 kV (b) [14, 15].

2.2.2 X-ray detector

As anticipated above, the X-ray detectors used nowadays in industrial CT systems are either flat panel detectors consisting of a 2D array of pixels, or straight or curved line detectors consisting of a 1D array of pixels. The acquisition step is more time consuming when using a 1D detector instead of a 2D detector. In fact, in the first case, only one slice is measured during one complete rotation of the object around the rotation axis and the object has to be translated in vertical direction for every new slice to be measured. On the contrary, in cone beam systems with flat panel detector, a complete rotation of the object is sufficient and no linear translation of the rotary table is needed. However, this solution is affected by artifacts arising from the cone beam source such as scattered radiation and Feldkamp artifact (see Section 3.3). For example, the scanning quality deteriorates from the center to the borders of the detector and the spatial resolution degrades in direction of the rotation axis. Fan beam configuration ensures higher accuracy (beam is more collimated and yield less scatter), more efficiency (detection of higher percentage of incident radiation with better SNR), higher resistance to higher X-ray energies allowing thicker objects to be measured and reduced deformations of the image when moving away from the central pixel when using curved rather than straight detectors.

Basically, there are three detector principles: (i) counting-type detectors, where the output of the detector is proportional to the total number of photon impacts, (ii) scintillation-type detectors or indirect detectors, where the output is proportional to the total photon energy and (iii) ionization detectors, when the output responds to energy deposition per unit mass [16]. The most widespread detectors are the indirect ones, often based on amorphous silicon TFT/photodiode arrays positioned behind X-ray scintillators that convert the X-rays into visible light. Detectors influence image quality through the size and quantity of pixels, and through their efficiency in detecting the energy spectrum generated by the source.

2.2.3 Kinematic systems

In medical CT scanners, X-ray source and X-ray detector continuously rotate around the object (patient), while the patient is translated horizontally. Industrial CT systems differs from this configuration, since they feature fixed X-ray source and detector. Between them, the object is placed on a rotary table allowing its rotation and, in addition, vertical translation only in fan beam systems or in cone beam systems with helical trajectory.

The magnification can be modified by changing the relative position of the object with respect to the X-ray source and the X-ray detector. The voxel size v_s (voxel means 'volumetric pixel') of the reconstructed three-dimensional model of the scanned object results from the geometrical magnification m:

$$m = \frac{SDD}{SOD} \qquad \text{(Eq. 2.2)}$$

$$v_s = \frac{p_s}{m} \qquad \text{(Eq. 2.3)}$$

where SDD is the source-to-detector distance, SOD the source-to-object distance and p_s detector pixel size (see Figure 2.7).

The closer to the source the object is positioned, the higher magnification and thus smaller voxel size is obtained. The voxel size is cubic in cone-beam systems, while, in fan-beam systems, it can present a different vertical dimension depending on the vertical step chosen for the translation of the object. The basic kinematic system, illustrated in Figure 2.7, usually consists of:

a. Rotary table for stepwise or continuous rotation of the workpiece
b. Horizontal translation axis (Z-direction), also named ‘Magnification axis’. Higher geometrical magnification (i.e. object positioned closer to the source) increase the image resolution but causes more blurred images due to the finite X-ray focal spot size.
c. Horizontal translation axis (X-direction) to move the turntable parallel to the detector.
d. Vertical translation axis (Y-direction) moving turntable and workpiece. In cone-beam systems with circular trajectory this axis is used only for positioning the workpiece in the detector field of view; in fan-beam systems and cone-beam systems with helical trajectory, it is necessary for the translation.

It is important to emphasize the fact that each machine component should have high geometrical accuracy and mechanical and thermal stability as they have a direct influence on measurement results.

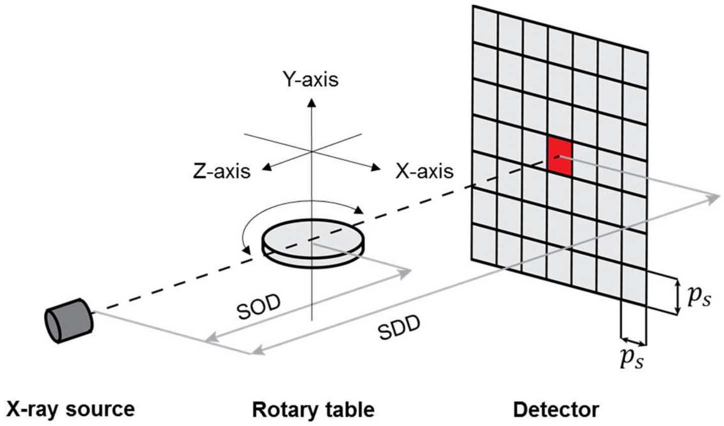

Figure 2.7: Scheme of a CT system. X-axis and Z-axis (magnification axis) are horizontal translation axes; Y-axis is both vertical translation axis and rotation axis. SOD is the source-to-object distance, SDD the source-to-detector distance and p_s the pixel size.

2.3 CT measurement procedure

Dimensional measurements by computed tomography can be performed by following the procedure schematized in Figure 2.8.

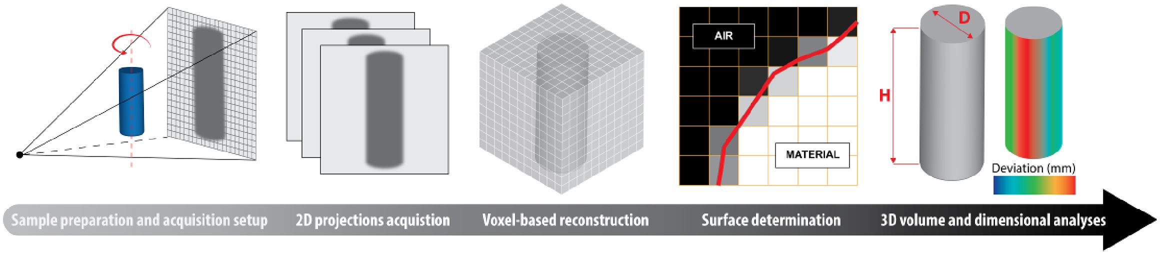

Figure 2.8: Typical CT measurement procedure.

Before the CT scan begins, the workpiece has to be properly prepared. For example, the workpiece has to be firmly placed on the rotary table to ensure its stable position during the scan, but any deformations of the workpiece has to be avoided. Materials that present a low absorption of the radiation, as carbon fiber or polystyrene, should be preferred for fixation stands, so measurement results won't be disturbed. Moreover, the object orientation should be studied in order to minimize the maximum thickness to be penetrated by the X-rays and to avoid typical CT artifacts, such as the so-called Feldkamp effect (see Section 3.3). A good practice is to let the sample stabilize in temperature (around 20 °C) inside the CT cabinet, in case of metrological CT systems with thermally controlled cabinet.

After sample preparation and stabilization, the object has to be precisely positioned relatively to source and detector. The turntable is used to position the sample at the desired magnification and vertical position. Then, when the acquisition phase starts, the rotary table is used to rotate the object while the X-ray beam (emitted by the X-ray source) propagates through its material. As the radiation interacts with the object, some X-rays are absorbed, some are scattered and some other transmitted. Only the transmitted photons reach the detector to create a 2D projection of the object. The process of X-ray intensity reduction is called *attenuation* and comprises both absorption and scattering, which are due to two effects: Photoelectric effect and Compton (scatter) effect (Figure 2.9).

The intensity loss is described by the Lambert-Beer's law (represented in Figure 2.10), stating that each layer of equal thickness absorbs an equal fraction of the radiation traversing it [17]:

$$I = I_0 e^{-\mu x} \quad \text{(Eq. 2.4)}$$

with I_0 initial intensity of the incident radiation (not attenuated), I final intensity (transmitted through the material thickness x) and μ linear attenuation coefficient.

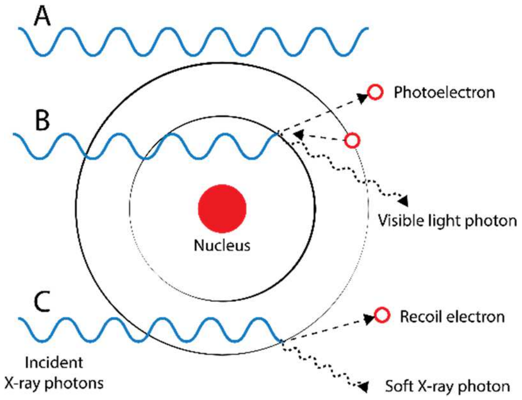

Figure 2.9: Transmitted radiation with no interaction between electrons (A); photoelectric absorption (B) and Compton scattering (C).

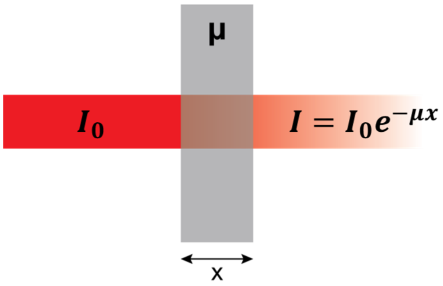

Figure 2.10: Illustration of material attenuation (uniform object) for a monochromatic x-ray beam following the Lambert-Beer's law.

The attenuation coefficient μ can be obtained by the linear attenuation coefficient due to the Photoelectric absorption (μ_p) and the coefficient due to the Compton effect (μ_c):

$$\mu(E) = \mu_p(E) + \mu_c(E) \quad \text{(Eq. 2.5)}$$

where E is the X-rays energy. Usually, materials with low atomic number have a lower attenuation coefficient with respect to materials with high atomic number. In other words, the attenuation is determined by the length traveled in the absorbing material, by the material compositions and density (i.e. attenuation coefficient μ) and by the X-rays energy. The attenuation allows detecting the presence of material and is measured by capturing the remaining X-rays that traverse the workpiece by means of an X-ray detector, resulting in a 2D grey image in case of a flat panel detector or a 1D grey profile in case of a 1D line detector.

Images are taken from different angular positions of the workpiece during its rotation. The angular step can be defined by the user from the desired number of radiographic projections, which can be derived for example by the following formula [18]:

$$Number\ of\ projections = \frac{N\pi}{2} \qquad \text{(Eq. 2.6)}$$

where N stands for the width of the projections (in pixels). For example, in the case of projections with a width of 1024 pixels, approximately 1500 projections should be acquired during the 360° rotation of the sample. The higher the number of projections, the better the resulting accuracy. However, a high number of projections increases the scanning time. By averaging the projection images at each specified angular position, the noise of a single projection can be reduced, enhancing the quality of the reconstruction with further increase of the scanning time.

Besides the number of projections being averaged and collected, several other scanning parameters as X-ray current and voltage, detector integration time (i.e. length of time that the detector is allowed to collect photons), geometrical magnification and beam filtration must be set by the operator to optimize the CT scanning resolution and accuracy. These parameters have to be chosen taking into consideration also part size, material and geometry complexity.

When the acquisition of 2D projection images is completed, the 3D volume of the scanned workpiece is obtained by a reconstruction software based on specific algorithms. The most common algorithm for reconstruction of cone beam projections is the *filtered back-projection* algorithm, also known as Feldkamp-Devis-Kress algorithm or Feldkamp (FDK) method [19]: the projections are filtered before the reconstruction in order to achieve higher reconstruction quality. Figure 2.11 shows an example of backprojection, resulting in a blurry version of the correct image, while Figure 2.12 an example of filtered backprojection resulting in a mathematically exact reconstruction of the image with reduced blurring content. The reconstructed 3D volume is a matrix composed of voxels, where each voxel is associated to a specific grey value connected to the local attenuation.

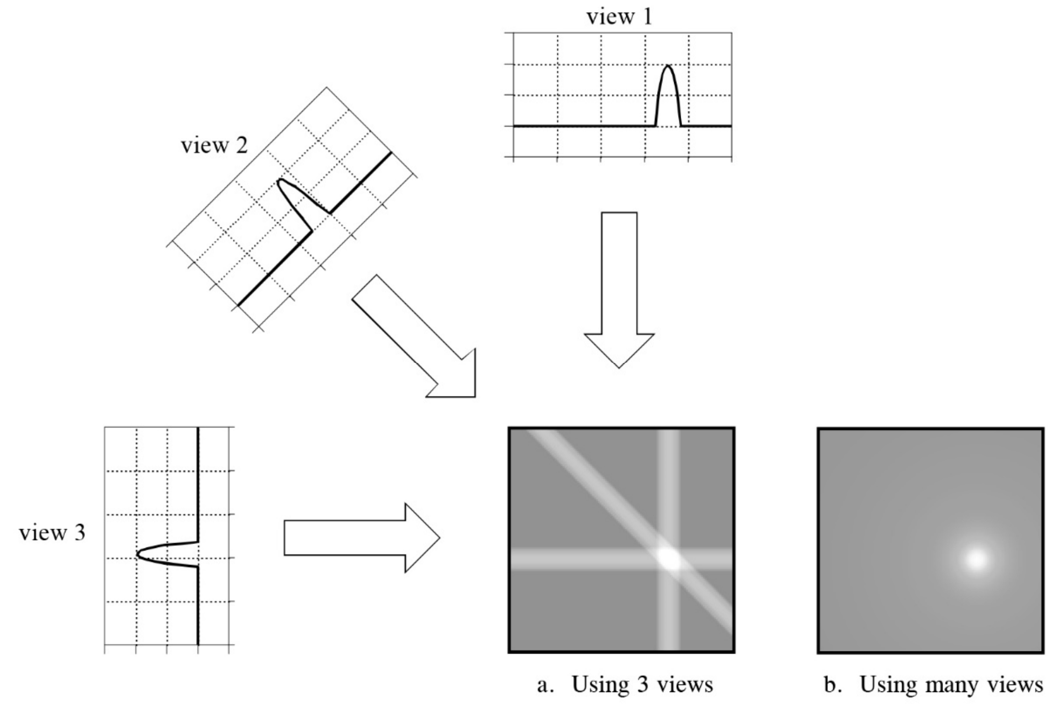

Figure 2.11: Backprojection reconstructs an image by taking each view and smearing it along the path it was originally acquired. Here views are represented as gray value profiles. [20]

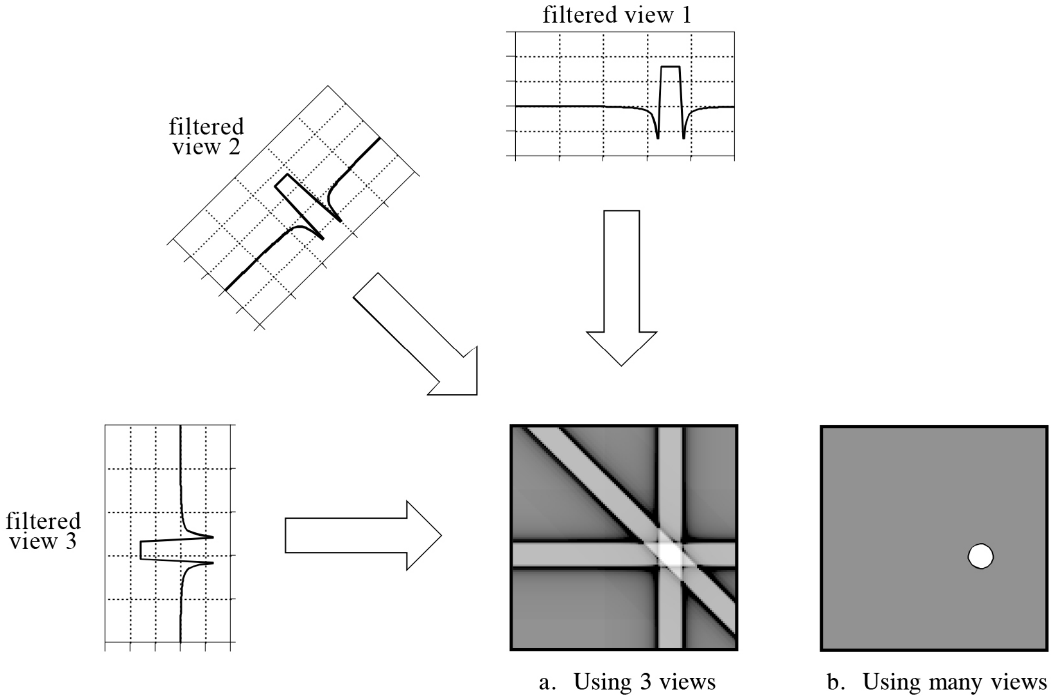

Figure 2.12: Filtered backprojection reconstructs an image by filtering each view before backprojection. [20]

Reconstruction software usually allows applying correction techniques in order to minimize some typical unwanted effects, such as scattering, beam hardening and noise (see Section 3.3).

Since the full scan field for CT is a cylinder, object dimensions must ideally contained in a cylinder with maximum diameter not exceeding detector borders. The higher the magnification, the smaller the maximum diameter (see Figure 2.13). The sample height could instead exceed detector borders in case the region of interest is in any case contained in the field of view, or if a multiple scan is performed followed by merging of the obtained volumes, or in case of helical scanning or fan-beam CT configuration.

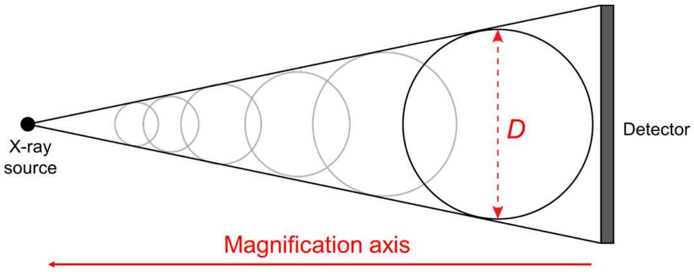

Figure 2.13: Top view of a typical CT system. The sample should be contained in a cylinder of diameter D to be fit in the detector field of view. This diameter decreases when geometrical magnification increases.

In dimensional metrology, determination of scale errors is an important aspect to be taken into account. In CT, the correction of scale errors consists in correction of the measured voxel size v_s by the use of calibrated reference objects (e.g. ball bars or other object featuring spherical or cylindrical shapes) with measurable dimensions not affected by the determined surface (see next page). These reference objects can be CT scanned before, together or/and after the measurement of the actual workpiece. The measured dimensions must be compared with the calibrated reference values. The corrected voxel size can be obtained as:

$$v_{s\_corrected} = \frac{L_{cal}}{L_{meas}} \cdot v_s \qquad \text{(Eq. 2.7)}$$

with L_{cal} reference length calibrated, for example, by tactile CMM and L_{meas} length measured by CT.

The resolution is also affected by the finite size of the focal spot leading to obtain blurred instead of sharp images (see Chapter 5). The focal spot size increases with the power (Watts) resulting from the chosen X-ray current and voltage. Finally, resolution and accuracy can be influenced by the quality of each hardware component of the CT system.

Once the reconstruction is done, the 3D reconstructed model of the scanned object can be visualized and virtually sectioned for visual inspections of inner and outer features and geometries as well as internal voids and inclusions. However, to be able to perform dimensional measurements, the object surface has to be determined. The edge detection (also called segmentation or surface determination) converts 3D voxel data into 3D surface data. With this aim, a threshold value has to be determined to distinguish between material and background or between two materials characterized by different densities. A common approach is to use an iso-50% threshold value [21], defined as the average value between air (background) and material (object), as seen in Figure 2.14. Due to the “partial volume effect” (i.e. CT attributes an average gray value to each voxel), (Figure 2.14-a) an intra-voxel interpolation is needed to locate the edge with sufficiently accuracy within edge transition voxels (Figure 2.14-b). This interpolation increases the resolution to sub-voxel resolution. The iso-50% threshold value can be used for a global surface determination. In this case, this value is applied to the whole volume, assuming a homogeneous material and absence of image artifacts (image artifacts are described in [17] as: ”discrepancies between the actual value of some physical property of an object and the map of that property generated by a CT imaging process”). However, in CT scans the presence of image artifacts due to beam hardening, scatter radiation, insufficient material penetration, etc. is common. For this reason, the global method is not well-suited for CT scanning. In particular, for accurate dimensional measurements, a local adaptive method is preferable. This method determines the surface in each voxel locally. The iso-50% value is used as a first estimate border. The surface location is then defined for each voxel locally by searching in grey level perpendicularity to the pre-determined surface within a user-defined search distance. Inaccuracies in determining the surface could lead to significant measurement errors [22, 23].

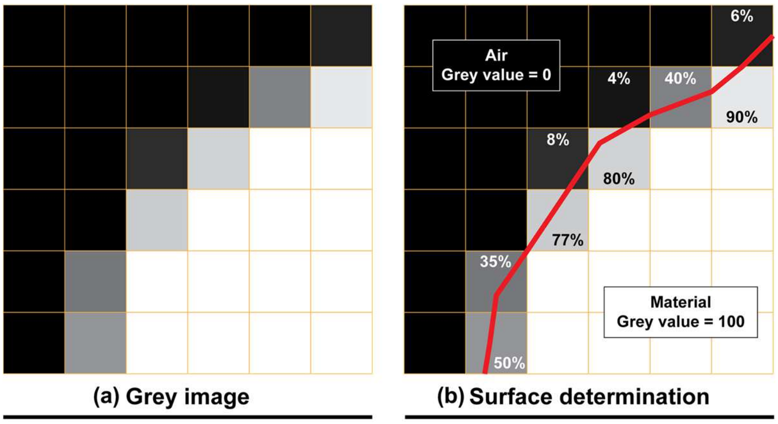

(a) Grey image

(b) Surface determination

Figure 2.14: (a) Grey image showing the "partial volume effect and (b) determined surface.

Dimensional measurements and evaluations can be performed directly on the voxel-based model with software specifically dedicated to CT data elaboration. Another possibility is to create a surface model (e.g. in STL format) using the information provided by the determined surface and creating a polygonal mesh composed by triangles. STL model extraction allows handling less memory consuming data with software which are not specific for CT. However, additional errors are introduced due to the extraction procedure.

Typical CT dimensional evaluations are (i) actual/nominal comparison, where actual CT measurements are compared with reference data coming for example from a CAD nominal model or from a CMM calibration, (ii) fitting (e.g. least-squares fitting) of geometrical elements on voxel data or surface data for dimensional measurement and geometrical tolerance verification (iii) wall-thickness analysis.

2.4 Overview of CT industrial applications

X-ray computed tomography has recently emerged as metrological tool for performing accurate dimensional measurements and as an attractive possibility for dimensional quality control in industry. The main reason of this interest is that CT introduces a series of important advantages with respect to other coordinate measuring systems (CMSs) such as tactile and optical systems. Using CT, a complete three-dimensional volumetric model of the scanned object can be obtained in a relatively short time with high-density surface digitalization. Non-destructive and non-contact analyses together with the possibility of measuring non-accessible and complex features (e.g. internal geometries, internal voids or inclusions, freeform surfaces, etc) make this technology unique. Furthermore, CT is capable of measuring also parts which are soft and/or flexible and so easy to be deformed, as well as objects of any color and material. Moreover, CT allows performing material analysis simultaneously to dimensional quality control [24]. Despite these advantages, CT is characterized also by significant drawbacks. In particular, the accuracy of CT measurements is affected by a large number of influence quantities. For this reason, the uncertainty determination and the measurement traceability are in most cases difficult. Moreover, CT scanning are characterized by image artifacts. Differently from other well-established CMSs, an international standardization of testing procedures for CT systems is not available yet, although a dedicated ISO working group is currently working on the definition of a dedicated CT part of the ISO 10306 series.

Figure 2.15 summarizes the main CT advantages and disadvantages.

Advantages

Non-destructive technique
Non-contact measurements
Measurement of inner and outer geometries
High density surface digitalization
Simultaneous material analysis and dimensional quality control
Possibility to scan any surface, shape, color or material up to a certain density and thickness penetrable by X-rays

Disadvantages

Multiple complex influence quantities
Standardization still under discussion
Several image and reconstruction artifacts
Measurement uncertainty difficult to be determined
Traceability is challenging
Problems with scanning multi-material objects
Maximum penetrable material thickness limits the object size

Figure 2.15: Advantages and disadvantages of CT, [adapted from 24]

Nowadays, the manufacturing industry is experimenting improvements in production technologies with production of more complex parts with freeform surfaces and a huge amount of different features [25]. The need for inspection and quality control of such parts requires new accurate and time efficient measurement technologies that could contribute to reduce waste and costs during the manufacturing. In this context, industrial X-Ray Computed Tomography (CT) offers a large variety of applications in the entire development and production chain [24]. In particular, CT should not be considered only a tool for quality check of products, but it can be better employed also for the so-called *First Article Inspection* (FAI), consisting in testing a pre-series product in order to discover possible issues connected to the production processes with important advantages in terms of effectiveness and time compression in process engineering. Furthermore, more recently, fast and in-line computed tomography systems are starting to be adopted in industry [26] for process control purposes. Figure 2.16 presents an overview of different fields of application for the CT technology in the industrial domain. Voxel based evaluations can be classified in visualization and non-destructive testing (NDT), while surface based evaluations comprise digitization and dimensional metrology. The need for traceability increases with the complexity of the task.

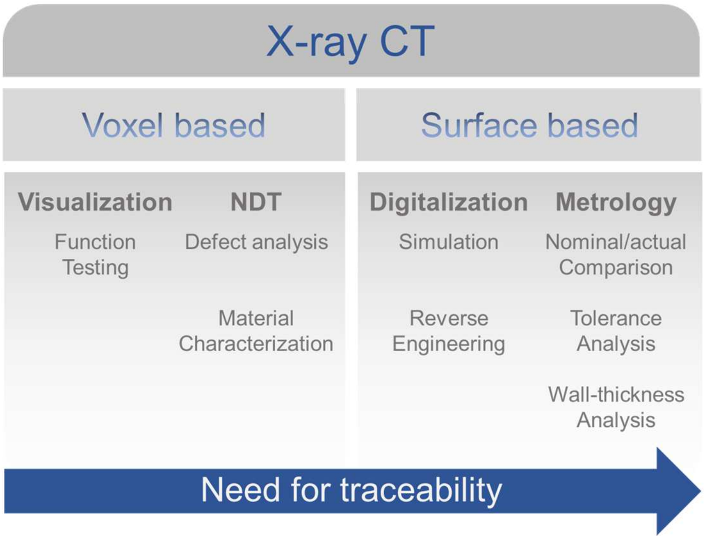

Figure 2.16: Fields of application for CT [adapted from 24]

Visualization analyses allows performing a visual qualitative inspection of industrial parts, e.g. functional testing of assembled workpieces under real working condition: individual components can be assessed from CT data in the assembled state, which is of high relevance to guarantee the proper functioning of the assembly. This can be done by segmentation procedures on components with appreciable difference between their material densities, or by comparison between pre- and post-assembly status (see the example in Figure 2.17). Moreover, contact surfaces between assembled components can be identified, as seen in Figure 2.18, showing a couple of examples.

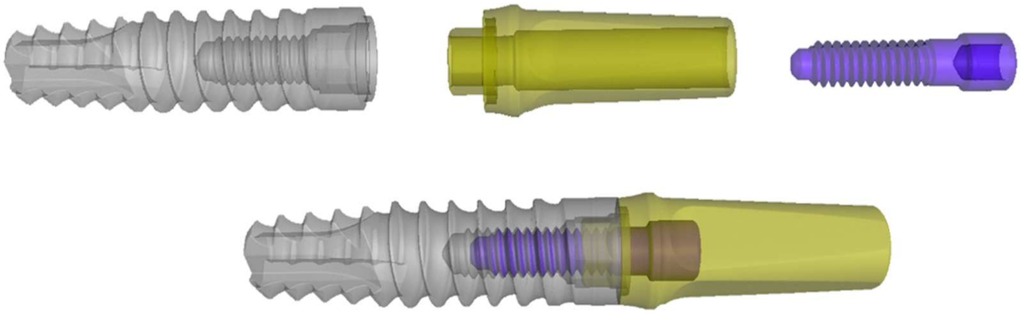

Figure 2.17: CT scan of components of a dental implant shown before and after the assembly (from measurements performed by the author).

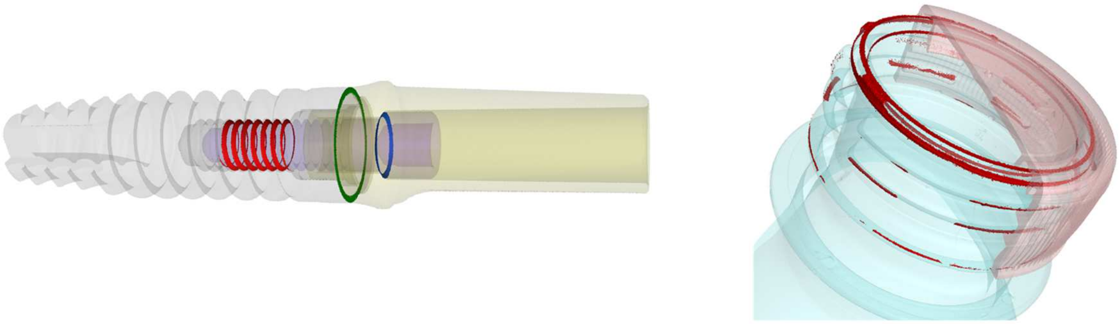

(a)

(b)

Figure 2.18: (a) Contact surfaces between individual components of a dental implant assembly and (b) between a bottle body and cup (from measurements performed by the author).

First CT systems introduced in industry were meant to perform basically non-destructive qualitative analyses. However, the more recent use of CT systems as measuring instrument for coordinate metrology applications opened up new possibilities in the product development, based on dimensional analyses. Nominal/actual comparison can be done to assess dimensional deviations between the actual part and the nominal/desired model, as well as verification of geometrical product specifications to determine if a part fits to the specifications.

Figure 2.19-a provides an example of nominal/actual comparison and Figure 2.19-b an example of dimensional measurements and geometrical tolerance verification.

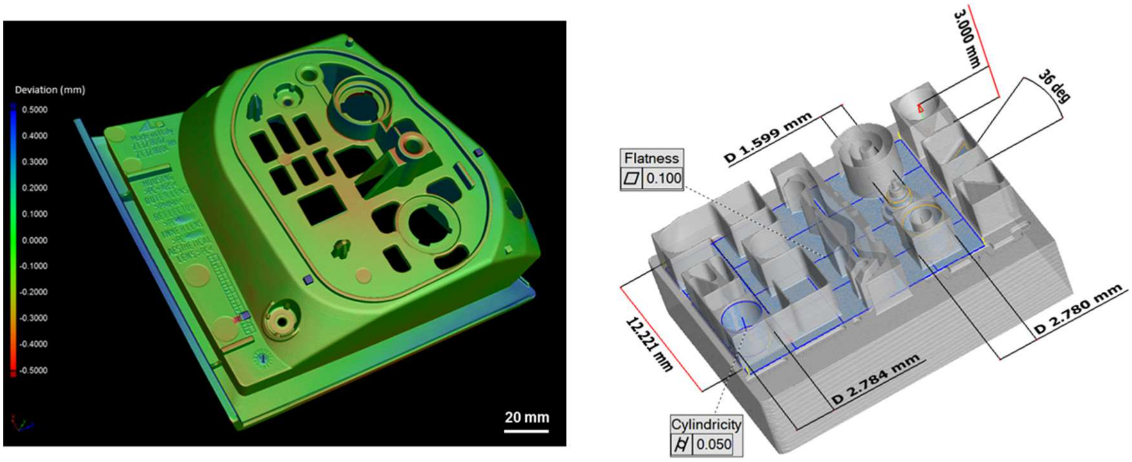

(a) (b)

Figure 2.19: Nominal/actual comparison of an injection-moulded polymeric component (a) and dimensional measurement and geometrical tolerance verification on a aluminium test part produced by micro-milling (b) (from measurements performed by the author).

Besides the comparison between actual part and nominal model (e.g. CAD model), similar comparisons can be also done between a CT reconstructed volume and data obtained using other measuring devices or between two CT scans of the same part but in different conditions. For example, wear analysis is possible by CT scanning and comparing the unworn and the worn part, as shown in Figure 2.20: wear of a micro-milling tool and wear of a knee prosthetic insert.

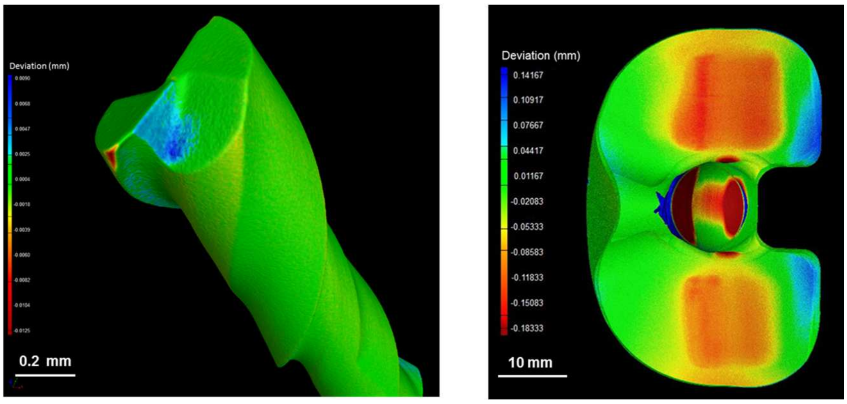

Figure 2.20: Wear maps of a micro-milling tool (left) and of a knee prosthetic insert (right) obtained by nominal/actual comparison between the CT scanned unworn and worn parts. The red zones correspond to the worn surfaces (from measurements performed by the author).

Wall-thickness analysis over the entire workpiece can be conducted as well, as shown by the example in Figure 2.21.

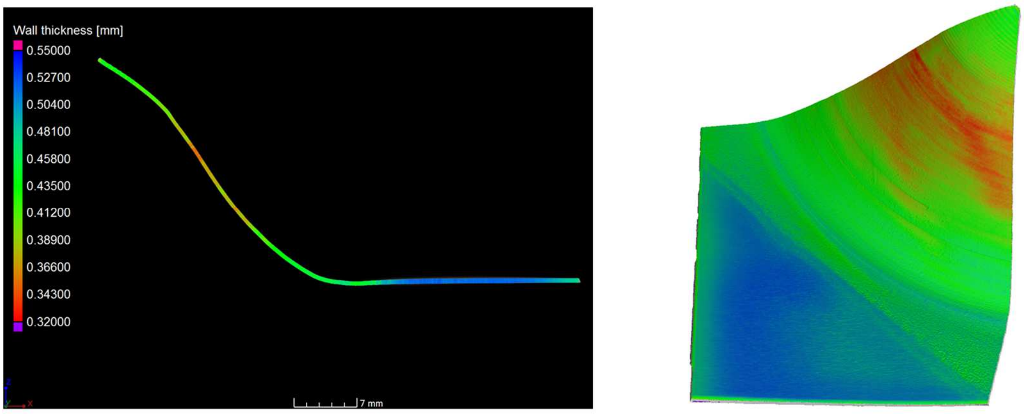

Figure 2.21: Wall-thickness analysis performed on a Ti6Al4V sheet in order to assess the impact of thermal treatments on deformations, shown in a 2D section (left) and in the 3D reconstructed volume (right) (from measurements performed by the author).

Fiber orientation, alignment and density in composite materials can be evaluated as well as defects (pores, voids, inclusions and cracks) distribution inside the part volume.

Metrological CT systems, in addition, can perform non-destructive analyses leading to quantitative information as in the case of defect analysis, where accurate evaluations of pores dimensions (size and volume) can be conducted. This is of great relevance for several manufacturing processes, first of all additive manufacturing (AM). AM processes, in fact, offer the unique possibility of producing complex internal features/cavities impossible to be manufactured with conventional manufacturing techniques and measured by conventional measuring instruments. Moreover, AM parts are characterized by the presence of inherent porosity. In Figure 2.22 an example of CT analysis conducted on an AM micro-valve is reported: the internal channel dimensions can be evaluated with no need to cut the sample and internal porosity can be analyzed in both distribution and volume.

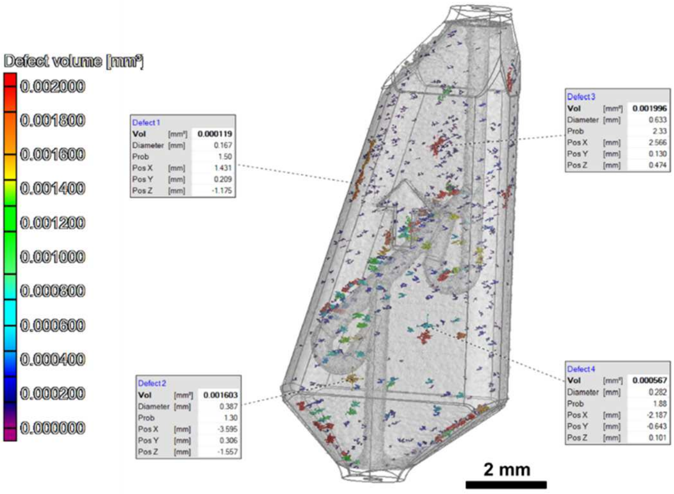

Figure 2.22: CT porosity analysis of a Ti6Al4V micro-valve produced by additive manufacturing. The internal channel can be evaluated in a non-destructive way. The colour scale to the left is linked to the defects volume (from measurements performed by the author).

The CT capability of generating virtual models of actual production parts can be used in several simulation techniques: the object of interest can be simulated starting from a detailed model of real workpieces instead of nominal models (CAD). In other cases, simulations results can be compared with data coming from computed tomography in order to get a more complete evaluation of some specific geometrical aspects. For example in [27], CT measurement of a test-part produced by micro-milling process was compared with simulations of the process, (see Figure 2.23). In this way, a comprehensive analysis of machining errors was possible.

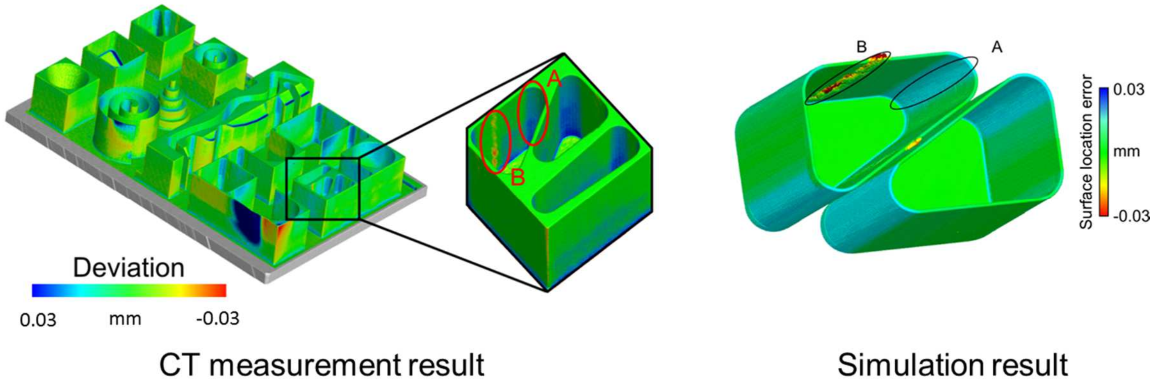

Figure 2.23: Deviations of the measured workpiece from the CAD model (left) and comparison of the simulated surface with the CAD model (right) (from measurements performed by the author, published in [27]).

Finally, CT enables the reverse engineering of products, consisting in a digitalization process oriented to obtain a model (e.g. CAD model) of a real part [28]. This process can be subdivided into two phases: (i) digitalization of the geometry of interest and (ii) modelling phase for creation of the CAD model. CT can be used for the first phase.

Chapter 3

Metrological traceability of CT measurements

This chapter discusses metrological traceability of CT. In particular, current tests used for CT performance verification and methods applied for uncertainty determination are presented. Moreover, descriptions of the main factors influencing CT performances and of reference objects suited for CT are provided.

3.1 Metrological traceability of CT measurements

Metrological traceability is a requirement of ISO 9000 [29] and ISO 17025 [30] and is defined by the international vocabulary of metrology (VIM) [31] as "the property of the result of a measurement or the value of a standard whereby it can be related to stated references, through an unbroken chain of comparisons all having stated uncertainties."

Dimensional measurements performed by CT have to be traceable to the units of the International System of Units (SI). This can be achieved by an unbroken chain of calibrations, aimed at connecting measurements carried out on a coordinate measuring system (CMS; in this case CT) to the length unit (meter). Two important steps are needed in order to evaluate the measurement accuracy as well as to ensure traceability: (i) metrological performance verification and (ii) assessment of task-specific measurement uncertainty. The first step is required in acceptance and reverification tests, aimed at verifying the ability of CT systems to measure calibrated sizes and forms. The second step, necessary for traceability establishment, consists in further analysis and tests oriented at determining the task-specific uncertainty of measurements [30].

However, CT measurements are affected by multiple influence quantities occurring in the CT measurement procedure, which are often difficult to be identified and accurately assessed. Furthermore, CT metrology suffers the lack of internationally accepted standards and guidelines which complicates both performance verification and uncertainty determination.

The most common approach to achieve traceability of CT measurements is the development of reference objects dedicated to CT, with concepts similar to those used in traditional coordinate metrology, for identification of error sources, correction of systematic errors, performance verification, determination of task-specific measurement uncertainty, etc.

3.1.1 Metrological performance verification

Performance verification of a measuring instrument consists of two types of tests: (i) acceptance test, to be performed when accepting a system to assess its conformance to the manufacturer's specifications and (ii) reverification test, to monitor performances over time, against user's requirements (may differ from manufacturer specifications).

In order to ensure comparability of results, either between different CT systems or with other coordinate measuring systems (such as tactile and optical CMMs), procedures for testing of CT systems should resemble the principles of ISO 10360-2 [32], which is internationally used for testing the length measuring performance of CMMs. Since the international standard dedicated to CT systems (which will be part of the ISO 10360 series) is currently under development, the most commonly adopted reference document is the German guideline VDI/VDE 2617-13:2012 [33], that is closely related to ISO 10360-2 except from the addition of specific aspects occurring when using CT systems. In particular, VDI/VDE 2617-13 provides guidance to verify: (i) length measurement errors (E) and (ii) probing error of size (PS) and probing error of form (PF). In fact, an important principle of acceptance testing is to assess both global and local performance – i.e. error – characteristics of CMSs (Figure 3.1) [34].

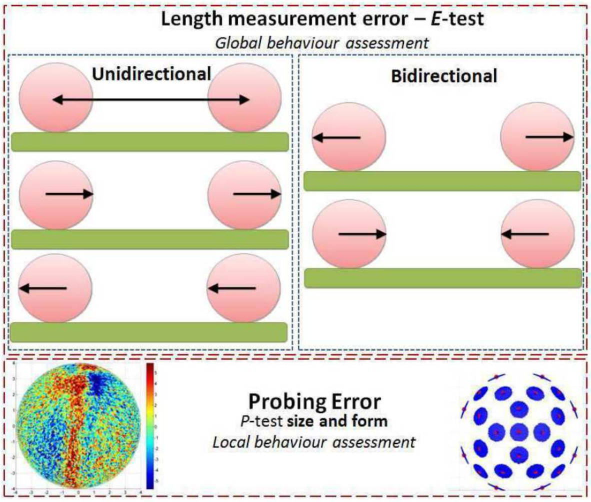

Figure 3.1: Global behaviour assessment – E-test performed as uni- and bidirectional length measurements (here for the case of cylindrical geometry); Local behaviour assessment – P-test tested as probing dispersion using 95% of the points and probing size error using all point, 25 representative points based on 25 patches and all probed points (here for the case of spherical geometry) [34].

The local error behavior is tested as a probing error test (P-test) assessing the diameter and form deviation of a calibrated sphere, calotte or special combinations of spheres and calottes with negligible form errors and surface roughness.

The probing error of form PF can be obtained from the following equation:

$$PF = R_{max} - R_{min} \quad \text{(Eq. 3.1)}$$

where PF is the span of the radial deviations of the measurement points from the calculated regression sphere (determined using the least-squares method with a free radius), R_{max} and R_{min} respectively the maximum and the minimum distance from the probing points to the center of the regression sphere.

The probing error of size PS is calculated as the difference between the measured diameter D_a and the calibrated diameter D_r of the sphere:

$$PS = D_a - D_r \quad \text{(Eq. 3.2)}$$

The current ISO 10360 draft for CT based CMS (2016) contains a 25-point probing procedure for the probing error test for form and size (PS and PF) in order to achieve comparability to the probing error of a tactile CMM, determined according to ISO 10360-5:2010 [35]. The object is measured at one hemisphere at two different magnifications using 25 representative points (for example, based on 25 patches; Figure 3.1) distributed over the sphere/calotte surface. Additionally, considering the large amount of measurement points determined by CT, another type of test takes into account 95% of the measured points for analysing PS and PF.

The global system behavior is tested as a length measurement error (E-test) using reference standards for lengths (e.g. hole plates, step gauges, ball plates, etc.). The acceptance test commands to measure 5 different calibrated lengths in 7 different spatial directions inside the measurement volume and 2 different magnifications.

For bi-directional measurements (e.g. using gauge blocks) the length measurement error is stated as:

$$E = L_a - L_r \qquad \text{(Eq. 3.3)}$$

where L_a is the measured length and L_r the calibrated length.

Measuring uni-directional lengths (e.g. sphere center-to-center distances) usually leads to lower errors. The main reason is that these measurements are not affected by the surface determination process as the bi-directional lengths. For ensuring the comparability between results of these types of length measurements, the VDI/VDE 2617-13 [33] provides a couple of methods to compute *E*.

The calculated errors should be contained inside the Maximum Permissible Error (MPE) limits, which is usually specified by the manufacturer of the system tested for acceptance. The expanded test uncertainty U (ISO/TS 23165 [36]) of the test method used shall be taken into account when comparing the length measurement error with its limit E_{MPE} in order to make a conformity decision (see ISO 14253-1 [37]):

$|E| \leq |E_{MPE}| - U$, for the manufacturer

$|E| \leq |E_{MPE}| + U$, for the purchaser.

3.1.2 Measurement uncertainty determination

According to the ISO GUM [38], the uncertainty of measurement is a parameter to be associated with the result of a measurement, that characterizes the dispersion of values that could reasonably be attributed to the measurand. Uncertainty of measurement comprises, in general, many components. Some of these components may be evaluated from the dispersion of results of a series of repeated measurements and can be characterized by experimental standard deviations. The other components, which can also be characterized by standard deviations, are evaluated using a certain type of probability distributions, which choice is based on experience or other information.

Every measurement result (y) should be accompanied by a statement about the measurement uncertainty (U), as specified by ISO 14253-1 [37]:

$$Y = y \pm U \tag{Eq. 3.4}$$

A task-specific uncertainty statement [39] is necessary in order to: (i) determine the quality of a measurement process, (ii) take decisions on conformance or non-conformance of products with specifications and (iii) achieve traceability to SI units (in this case the unit of length: meter). However, since CT are multi-purpose measurement instruments affected by a large amount of influencing factors and by their interactions (Section 3.3), the statement about the measurement uncertainty is often a difficult task and no widely accepted standards and guideline exist up to now [40]. Different procedures for uncertainty determination of industrial CT measurements are applicable, such as expression for analytical calculated uncertainty budget (standard GUM method using error propagation theory [38]), variability simulation (e.g. Monte-Carlo method), experimental determination of systematic and stochastic variability (ISO 15530-3 [41]), etc. The general methodology is to calculate the measurement uncertainty through an uncertainty budget according to GUM [38]. This requires a mathematical model including all the quantities influencing the value of the measurand and that specifies the effects of changes of each input quantity on the measurand. Due to numerous influencing factors and the lack of knowledge for modeling their influence, the most challenging part in the GUM procedure is to define analytic equations considering all relevant input quantities. Consequently, even though the GUM is the reference document for consistent evaluation of measurement uncertainty, this method alone is not feasible to be applied to determine the uncertainty of CT measurements.

A simpler and practical way for uncertainty determination is the *substitution method*, adapted for CT using the procedure described in ISO 15530-3:2011 [41] for tactile coordinate measuring machines. This approach is based on a sequence of repeated measurements of a calibrated workpiece performed using the same strategy and the same conditions as measurements on actual production parts. Moreover, the calibrated workpiece used in the procedure must be of similar material, size and geometry as the actual part to be measured. The calibration of the reference workpiece should be performed by a more accurate measuring system (e.g. tactile CMM) to ensure traceability.

The final measurement result can be expressed as:

$$Y = y - b \pm U \quad \text{(Eq. 3.7)}$$

with systematic error $b = \bar{y} - x_{cal}$ ($\bar{y}$ actual value obtained by CT; x_{cal} calibrated value obtained by CMM).

A different approach for uncertainty determination for CT dimensional measurements was proposed by Dewulf et al [42]: since a CT model is a voxel model, the result of a CT dimensional measurement can basically be interpreted as the product of the number of voxels and the voxel size and the relative uncertainty can be considered as caused by the uncertainty on the voxel size and the uncertainty on the edge detection.

The difficulty of accurately determining CT task-specific uncertainty is proved by results achieved by three international intercomparisons. The first intercomparison, *CT Audit* (2009-2012) [43], was carried out and organized by the University of Padova (UNIPD), Italy. Four different calibrated samples representing a variety of dimensions, geometries and materials were measured by several participants coming from America, Asia and Europe. Several uncertainty evaluation methods were applied by different participants: GUM method, substitution method, experience-based, MPE-based. Normalized errors En were calculated according to ISO/IEC 17043:2010 [44] (Eq. 3.8) in order to assess the validity of the estimated expanded uncertainties.

$$En = \frac{x - X}{\sqrt{U_{lab}^2 + U_{ref}^2}} \quad (3.8)$$

where x is the participant's result, X is the reference value from calibration, U_{lab} is the expanded measurement uncertainty of the participant's result and U_{ref} is the expanded calibration uncertainty of the reference value. If $|\, En \,| < 1$ a good agreement between participant's results and reference value (both with their expanded uncertainty) can be concluded. Results proved that less than half of the participants' measurement results were accompanied by a valid measurement uncertainty statement.

The second intercomparison is the CIA-CT intercomparison on industrial CT for measurement applications (2012-2013) [45], which was organized by the Centre for Geometrical Metrology (CGM), Department of Mechanical Engineering, DTU, Denmark. The main goals of this comparison were to test the applicability of CT for dimensional measurements of small objects, commonly measured in industry, which are more representative than artificial reference standards. Results showed that 45% of the measurements yield $|En|$ values larger than 1.

Finally, the InteraqCT comparison on assemblies (2015-2016) [46] was organized by the CGM, Department of Mechanical Engineering, DTU, Denmark, to test the applicability of CT for measurements of assemblies with dimensions and materials commonly adopted in industry. In this case, the majority of participants stated measurement uncertainties based on MPEs, whereas just a few participants used more complex uncertainty models. Out of a total of 110 measurement values obtained by the participants, 29% of those measurements yielded $|En|$ values larger than 1.

Results of these three intercomparisons demonstrate that uncertainty determination is still a major challenge for CT dimensional measurements. However, an improvement over time can be observed from the En values.

3.3 Influence factors

CT metrology is affected by a large number of influence quantities occurring over the entire measurement chain, which in most cases are difficult or impossible to be quantified. As already explained in the previous sections, uncertainty determination and traceability establishment are complicated by these influences. The German guideline VDI/VDE 2630-1.2 [47] offers a complete overview on these influencing variables, which are summarized in Figure 3.2. Some parameters and factors influencing CT measurements can be chosen by the operator to obtain proper CT images (target, beam current and voltage, workpiece material and geometry, temperature control, scanning and measurement strategy, user influence, etc) other are imperfections typical of CT images (beam hardening, scatter, ring artifacts, metal artifacts, noise, Feldkamp errors, geometrical errors artifacts, etc.).

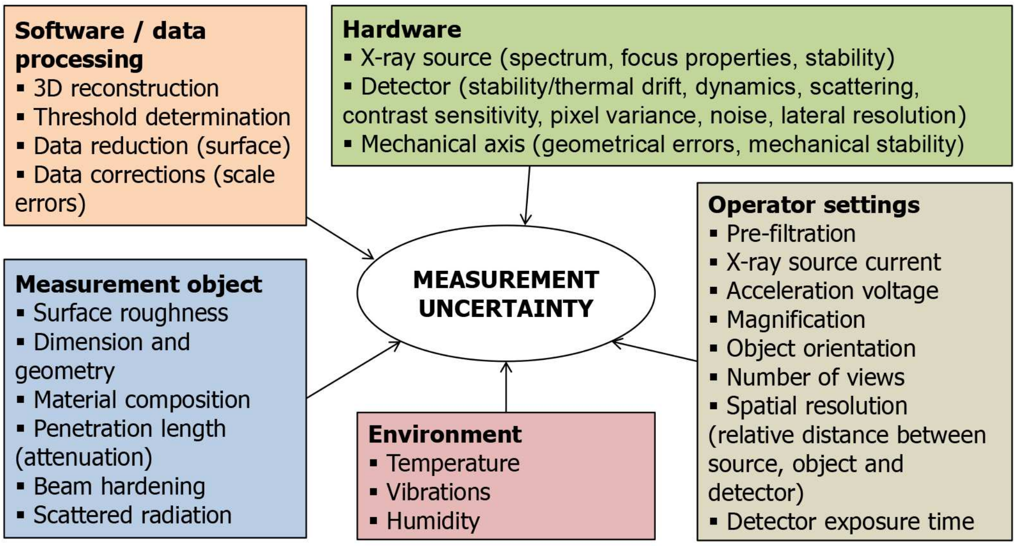

Figure 3.2: Overview of influence quantities for CT dimensional measurements [48]

In the following, some of the most relevant influence quantities are briefly described.

Beam hardening

Beam hardening concerns the non-linear attenuation of an X-ray beam along its propagation path through a workpiece due to the polychromatic character of the spectrum and the energy dependent X-ray attenuation [49]. As the beam pass through absorbing material, low energy (soft) X-rays are more rapidly attenuated than high energy (hard) X-rays. While the hard X-rays are able to fully penetrate the part reaching the detector, the soft X-rays extinguish after a certain traveling distance. Consequently, the number of photons hitting an X-ray detector and the grey value of the corresponding pixel is not strictly linearly related to the penetrated material thickness.

However, most reconstruction algorithms are based on a linear attenuation assumption, the high absorption of soft X-rays at the edge of the part gives the false impression that the skin of the part is made of more absorbing material, causing this edge to color lighter than the core of the part in reconstructed CT models. In addition, streaks or dark bands between dense object degrade the image quality. Beam hardening often results in the so-called *cupping effect* (Figure 3.3).

Beam hardening can be reduced or completely eliminated following two main approaches:

- physical filters with a certain thickness, usually made by Al or Cu, can be interposed between the X-ray source and the object to filter out the soft component of the radiation;
- correction through linearization technique based on an estimation of the relation between a propagated path length within the object and a corresponding measured intensity.

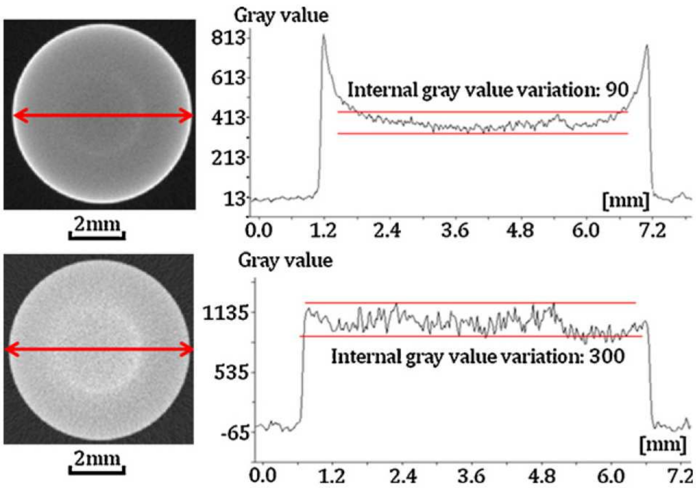

Figure 3.3: Reconstructed slices of a steel cylinder and corresponding grey value profile along the red line without beam hardening correction (top) and after beam hardening correction (bottom). The so-called *cupping effect* can be observed when the beam hardening is not corrected. [49]

Feldkamp effect

The so-called Feldkamp effect is related to the algorithm typically used for 3D reconstruction in CT (Feldkamp-Davis-Kress algorithm [19]). The resulting artifact (sometimes called "cone beam artifact") appears only in reconstruction obtained from 3D cone beam CT systems. As illustrated in Figure 3.4, in fan beam reconstruction, each individual point (e.g. point A) can be obtained by summing the filtered projection values along a trajectory TA, which is always a straight line on the projection plane. On the contrary, in cone-beam reconstruction, points far from the central detector horizontal plane (e.g. point B) follow an elliptic trajectory TB: in most cases this points values contain errors, which increase with the increase in cone angle θ producing strong artifacts on the surfaces parallel to the beam [49].

Ring artifact

Improper corrections of non-ideal or defective detector pixels may cause the formation of ring artifacts in the CT volume. A pixel with non-linear response causes a wrong signal at the same location in each CT projection. During the back-projection step in the reconstruction process this 'bad pixels' will form concentric rings in axial planes in the CT volume due to the circular trajectory. Figure 3.5 shows typical ring artifacts encountered in an axial CT slice from a CT where detector calibration is insufficient [51]. Besides issues with imperfect detector behavior, also stationary objects in the projections, other than the test component under study which is rotated, may lead to the formation of ring artifacts.

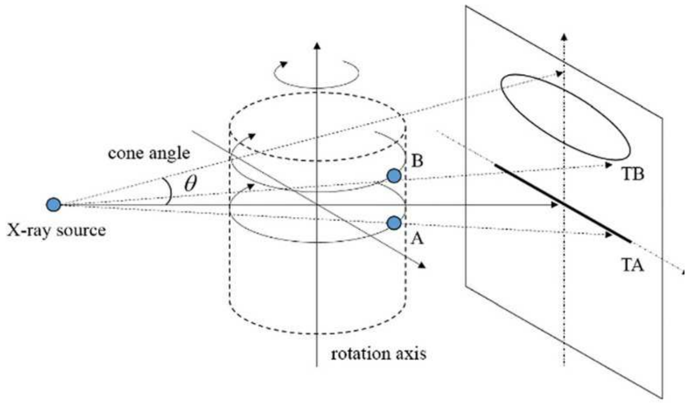

Figure 3.4: Projection trajectory of fan beam scanning and cone beam scanning [50]

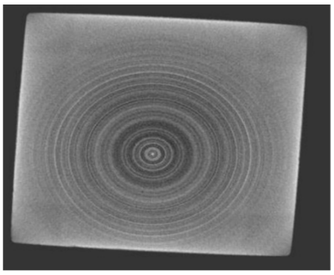

Figure 3.5: Example of ring artifact [51]

Noise

In principle, random image noise must be classified into the categories of quantum noise and detector noise. The quantum noise is produced by fluctuations caused by scattering and absorption while the radiation passes through the object. Its amplitude remains constant as the signal level changes (Figure 3.6-a). In other words, the quantum noise level is linearly increased with the intensity, so dark and light regions in the image are equally noisy. In contrast, detector noise (Figure 3.6-b) is a thermal noise produced by the electrons in the detector, it does not depend on the X-ray exposure, and above all it can also be measured without radiation. This type of noise that increases with the square-root of the signal level, resulting in the bright areas being more noisy than the dark ones. Both sources of noise are present in most images, but one or the other is usually dominant. For example, it is common for the noise to decrease as the signal level is decreased, until a plateau of constant amplitude noise is reached [20].

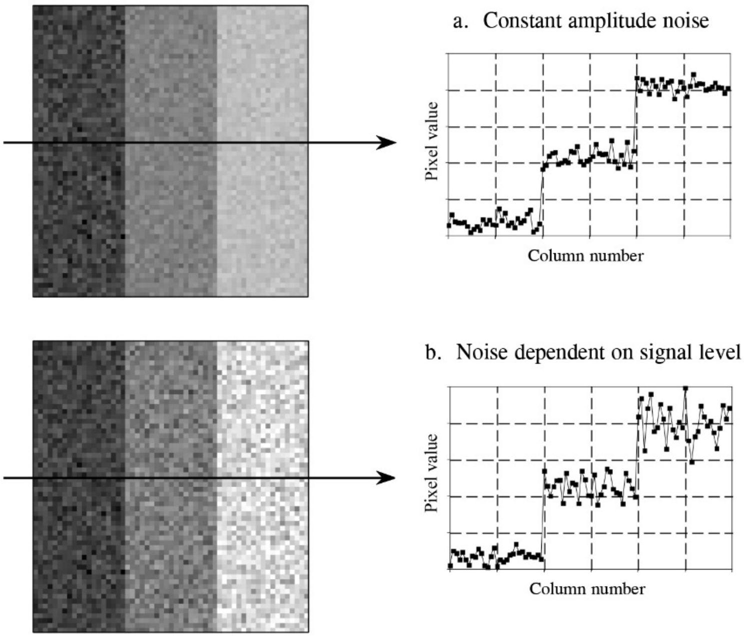

Figure 3.6: Random noise in images takes two general forms: quantum noise (a) and detector noise (b) [20].

2.4 Reference objects

As already anticipated, the most common approach for traceability of CT measurement is the development of reference objects dedicated to CT, with concepts similar to those used in traditional coordinate metrology. Several reference objects are proposed by guidelines and research works and they can be distinguished based on their material, configuration and function. Reference objects featuring high-precision spheres are well suited for investigations on the influences on dimensional measurements, as well as for scale error correction (Section 2.3). In fact, they are not influenced by edge detection, threshold value determination, beam hardening or surface offset because the sphere center is measured unidirectionally. A selection of these kind of objects is shown in Figure 3.7.

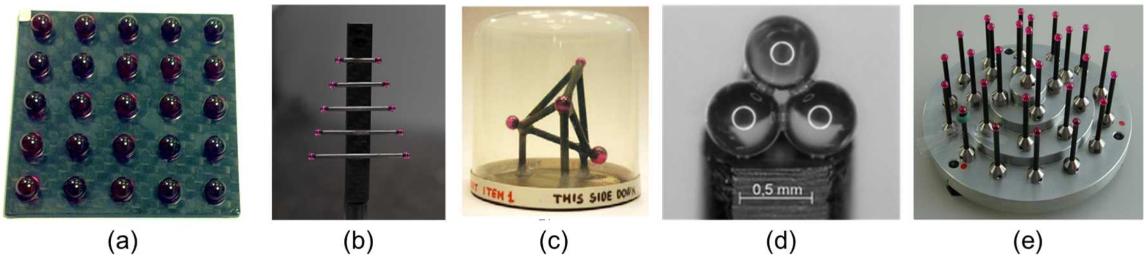

Figure 3.7: Selection of reference objects featuring high-precision spheres to investigate specific influences on dimensional measurements and to perform scale error correction. (a) Ball plate, DTU; (b) CT-tree, DTU; (c) CT-tetrahedron, UNIPD; (d) Sphere tetrahedron, PTB; (e) 27 ruby spheres.

In [23] a tetrahedron made by 4 touching spheres was also used to find the optimal threshold value by sphere distance calculation. However, these items usually do not allow the setting of the correct threshold value, because the material of the spheres (ruby, zirconia, alumina, steel) often differ from common workpiece materials (plastic, Aluminum, Titanium, steel). Other possibilities to map 2D/3D deviations and to define CT rescaling factors are the 2D calotte plate [52] and the 3D calotte cube [53] (Figure 3.8-a,b), proposed by PTB and made of more dense materials.

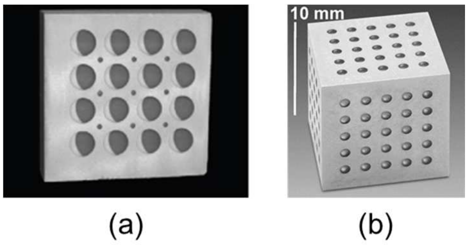

Figure 3.8: Calotte plate (a) and calotte cube (b) manufactured by PTB, Germany [52, 53].

Other reference objects were proposed in order to study the threshold effect, like the fiber gauge (Figure 3.9-a) proposed by Carmignato et al [22]. The optimal threshold value can be evaluated by the simultaneous measurement of internal and external features. The measured diameters were found to be strongly dependent on the chosen threshold value, as shown in Figure 3.9-b.

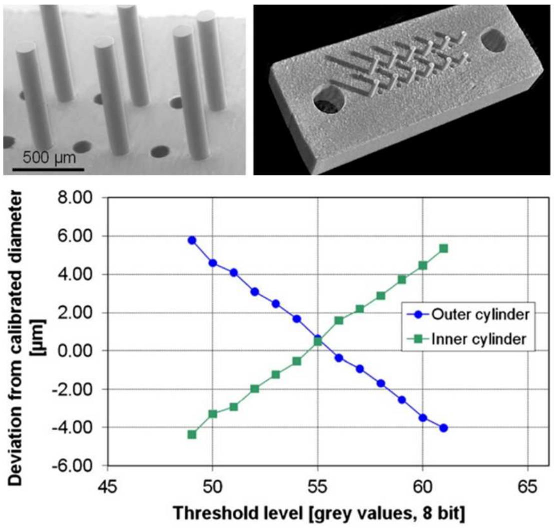

Figure 3.9: Reference standard developed for testing micro-CT systems: the 'fibre gauge', featuring fibres and holes. The diagram above shows the influence of the threshold value on the measured diameters of cylindrical features. As the threshold value increases, diameters of inner cylinders increase, while diameters of outer cylinders decrease. [22].

Errors of bi-directional length measurements can be determined from calibrated face-to-face distances measured on samples with plane and parallel surfaces such as step gauges and Cactus step gauge [54] (Figure 3.10) or from calibrated tubes length of the Pan flute gauge (Figure 3.11) [43]. Because the majority of reference standards have the drawback that their features are not similar to actual industrial workpieces, Bartscher et al [55] presented a dismountable freeform reference standard made from a cast miniaturized aluminum cylinder head. It can be dismounted in four segments, with fixed reference geometries (spheres and cylinders) (Figure 3.12).

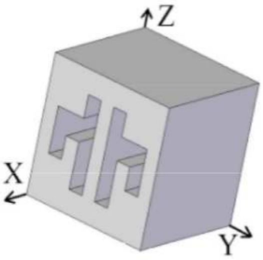

Figure 3.10: 3D model of the 'cactus' step gauge [54].

Figure 3.11: 'Pan flute' gauge consisting in 5 tube made by borosilicate glass with different calibrated lengths [43].

Figure 3.12: Aluminum segment dismountable freeform reference standard developed by PTB [56]

Several reference objects have been developed to analyze specific influence quantities. A step-cylinder with a central bore inside [53] is well suited to adjust the measuring parameters versus material-specific absorption and penetration thickness (Figure 3.13). Moreover, it allows detecting the maximum possible material thickness. A step-cylinder without inner hole as well as a step wedge (Figure 3.14) can be used for beam hardening correction [48]. Reference items as the multi-wave standard, the PTB sample incorporating grooves and flanges, and the 'Hourglass' standard were proposed to evaluate the metrological structural resolution of CT systems (references and descriptions will be provided in Section 5.3).

Figure 3.13: Example of step cylinder with maximum diameter 250 mm [53].

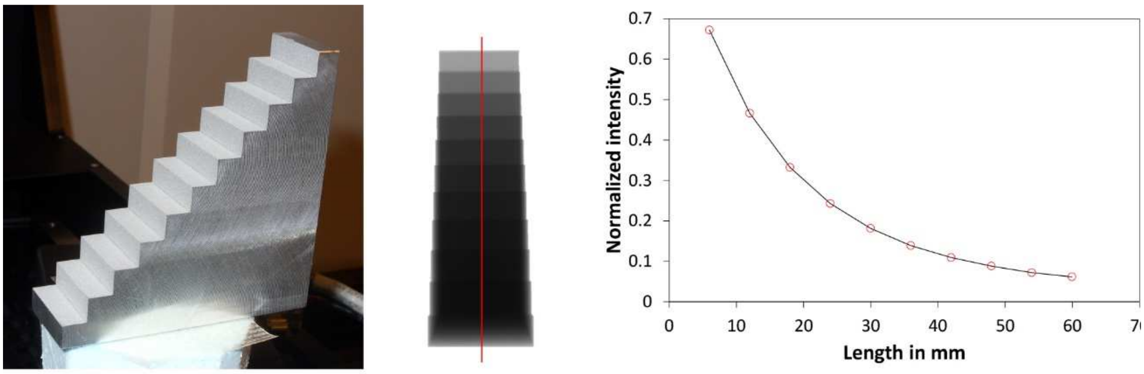

(a) Step wedge.

(b) Projection image.

(c) Correction curve.

Figure 3.14: Principle of beam hardening correction method using a reference object - step wedge [48].

Multiple dedicated objects were designed in order to estimate the CT geometry and perform a geometrical calibration (references). For example, Cho et al [56] proposed a reference object with spheres mounted on two static circular trajectories allowing the geometry of the system to be resolved in just one pose with no need to rotate the object (Figure 3.15). Finally, Hermanek at al. [57] developed a cylindrical reference standard with internal artificial calibrated defects for achieving traceability of CT measurements of internal porosity (Figure 3.16).

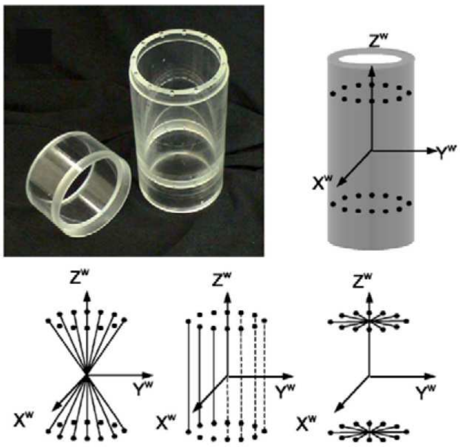

Figure 3.15: Reference object with circular static trajectories used for geometrical calibration of a CT system [56].

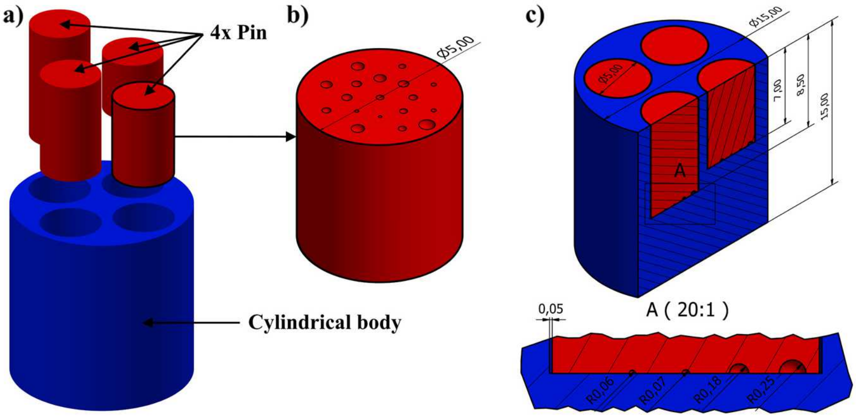

Figure 3.16: Reference object for accuracy evaluation of CT porosity measurements; a) 3D image of the object, b) magnified image of a pin, c) general dimensions of the object.

Chapter 4

Experimental study on material influence in dimensional CT

This chapter presents tests conducted within the ISO TC 213 WG 10 experimental study on material influence in dimensional computed tomography (CT). The main intent of this study is to demonstrate if there are major additional length measurement errors resulting from material effect that are not covered by the current testing procedure using hole plate measurements

4.1 Study motivations

The study described in this Chapter is part of a test survey organized by the working group ISO TC 213 WG 10 which is developing the future ISO 10360-11 for CT metrological performance verification. The main intent of this study was to demonstrate if there are major additional errors resulting from material effect that are not covered by the testing procedure using hole plate measurements which is currently proposed by the draft.

4.2 Description of used reference objects

For this experimental study, PTB (Physikalisch-Technische Bundesanstalt, German National Metrology Institute) provided an uncalibrated hole plate made of aluminum (AL1; size 48 mm x 48 mm x 8 mm, see Figure 4.1).

In addition, a reference standard with dimensions similar to the aluminum hole plate but negligible material effect was used: “CT Ball Plate” (Figure 4.2), manufactured and calibrated by DTU. It is a calibrated object which features a regular 5 x 5 array of ruby spheres with nominal diameter equal to 5 mm, glued on a 2 mm thick carbon fiber plate (size 50 mm x 50 mm x 2 mm).

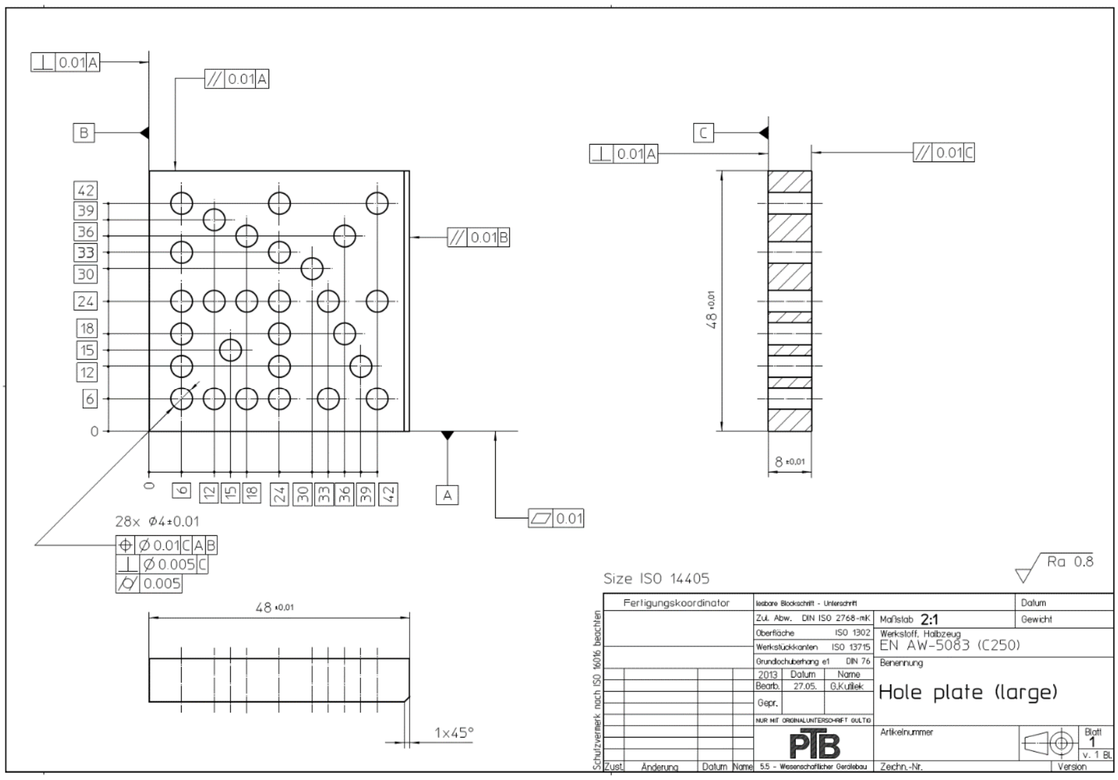

Figure 4.1: Technical sketch of the larger hole plate made from aluminium

Figure 4.2: CT ball plate (spheres have a nominal diameter of 5 mm and are placed on a 5 x 5 grid with inter-sphere distance of 10 mm). [58]

4.3 Description of the measurement procedure

CT measurements in this study were performed using the CT system described in Section 1.4.1.

The acquisition parameters are listed in Table 4.1.

Table 4.1: Scanning parameters

Reference	Voltage, kV	Current, µA	Filter	Exposure time, ms	Voxel size, mm
Aluminum Hole Plate	199	64	0.5 mm, Cu	2000	0.0360
CT Ball Plate	140	104	NO	1000	0.0360

The aluminum hole plate was scanned in three different configurations:

1) Tilted position (45 degrees, see Figure 4.3),
2) Vertical position (see Figure 4.4),
3) Tilted position (45 degrees, as in Figure 4.1) together with an Aluminum block (50 x 25 x 10 mm, see figure 4.5) covering half of the hole plate volume.

The procedures reported in [59] and [60] were used as reference for CT measurements of the hole plate.

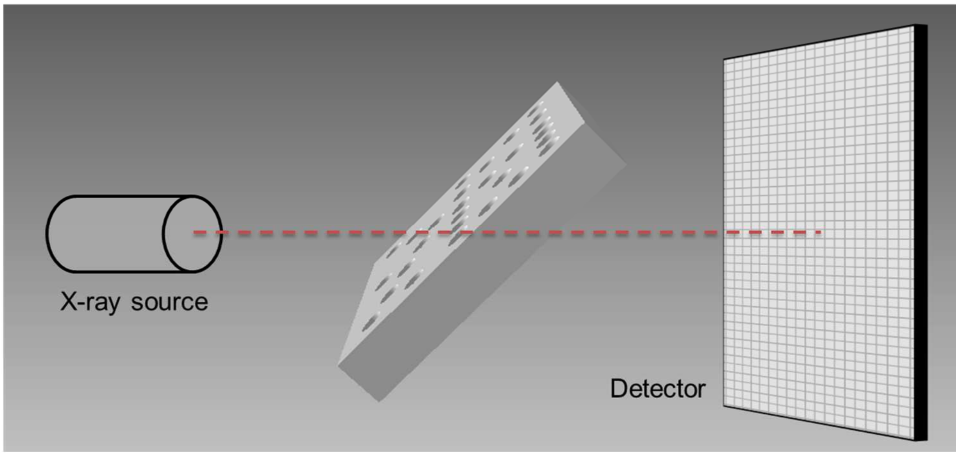

Figure 4.3: Hole plate in tilted position.

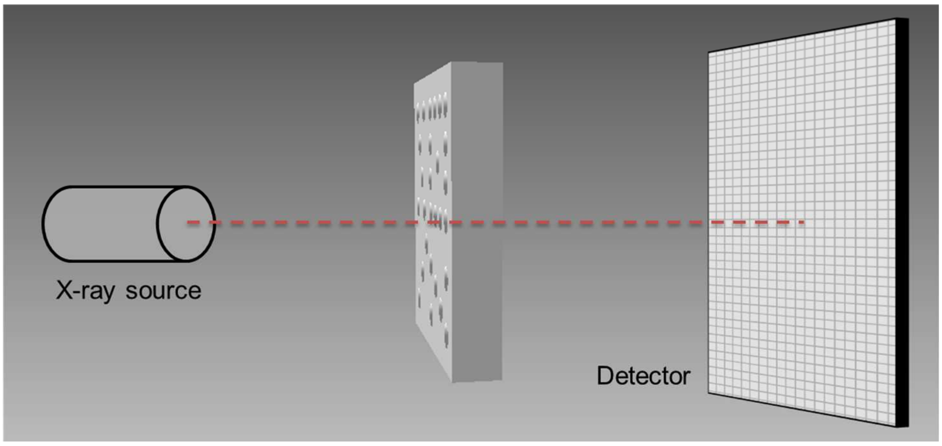

Figure 4.4: Hole plate in vertical position.

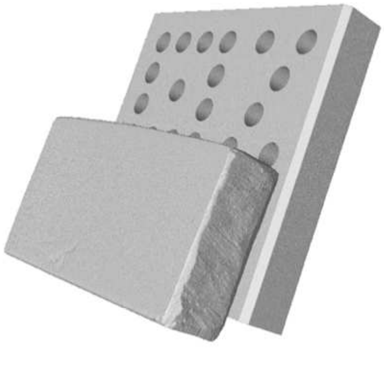

Figure 4.5: Hole plate in tilted position with the additional Aluminum block.

The "CT Ball Plate" (Figure 1.3) was scanned at the same magnification and the same two orientations (tilted position (45 degrees), and vertical position) of the hole plate, for comparing respective measurement results.

Length measurements performed on the CT Ball Plate are uni-directional (center-to-center distances), while length measurements on the hole plate can be both uni-directional and bi-directional as shown later in Table 4.2. Therefore, only uni-directional length measurements of the hole plate are comparable with corresponding length measurements of the ball plate.

Finally, two different beam hardening corrections were applied for each of the three configurations of the hole plate (for comparing their influence on measurement results):

- preset 1: $y = x$ (no correction)
- preset 2: $y = 0.75x + 0.25\, x^2$.

Nikon CT PRO 3D software was used for tridimensional reconstruction of the CT data and for corrections implementation.

4.4 Measurement results

4.4.1 CT Ball Plate

Since the CT Ball Plate is a calibrated object, length measurement errors could be evaluated as the differences between measured and calibrated values. These errors were compared to the maximum permissible length measurement error (E_{MPE}) stated by the manufacturer of the CT system. A total number of 100 sphere-to-sphere distances were determined (50 along x-axis and 50 along y-axis). Figure 4.6 and Figure 4.7 show how center-to-center distance errors lie within the MPE limits, for both positions of the ball plate. In particular, Figure 4.6 refers to the tilted position (45 degrees) and Figure 4.7 to the vertical position. Vertical position of the sample produced smaller errors. Due to the relatively small errors (for both vertical position and tilted position), scale factor is very close to the unit. For this reason, voxel size corrections were not applied; then no voxel size correction was applied also for CT measurements of the hole plate (which was scanned at the same magnification). Differences between uni-directional lengths obtained in the two different positions were evaluated (see Figure 4.8): average difference is 0.08 μm with a standard deviation of 2.44 μm and a maximum difference of -9.3 μm (which could be assumed to be an outlier). The range of all differences is [-8, 5.4] μm; 95% of the differences are in the range [-4.9, 4.8] μm.

Figures 4.6 and 4.7 distinguish between distances along x-axis (black squares) and distances along y-axis (red circles). It can be noticed that the position change of the ball plate resulted in an inversion of sign of errors: for instance, distances taken along x-axis have a positive trend in tilted position and becomes negative in vertical position.

Finally, distributions in Figures 4.9 and 4.10 show that distance differences along y-axis have a larger variability range (from -8 to 5.4 μm) than those along x-axis (from -1.4 to 4.7 μm). This behavior will be compared with hole plate's results.

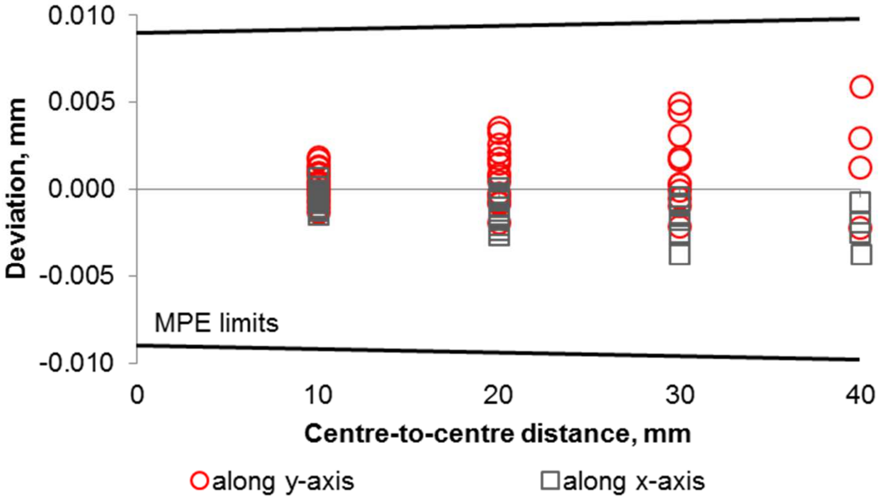

Figure 4.6: Length measurement errors determined from the ball plate measured in <u>tilted position</u>; MPE limits are visible.

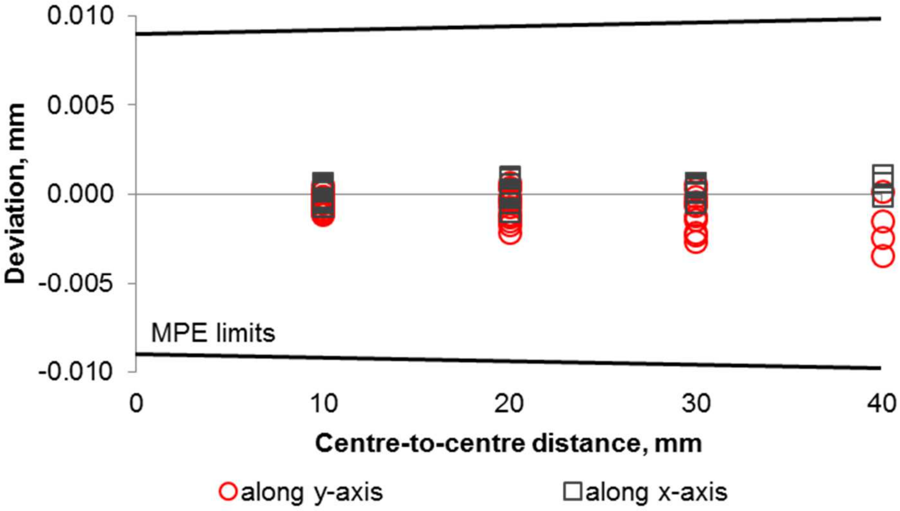

Figure 4.7: Length measurement errors determined from the ball plate measured in <u>vertical position</u>; MPE limits are visible.

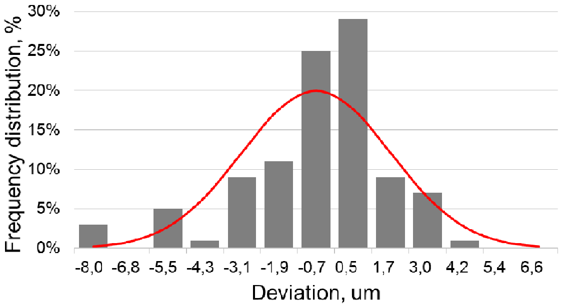

Figure 4.8: frequency distribution of differences of measurement results obtained in two positions (tilted, vertical) of the ball plate

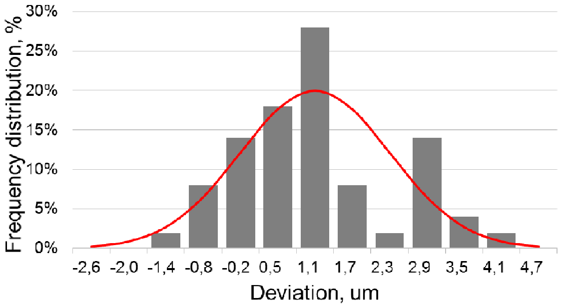

Figure 4.9: frequency distribution of differences of measurement results obtained in two positions (tilted, vertical) of the ball plate; results are limited to lengths measured along the x-axis.

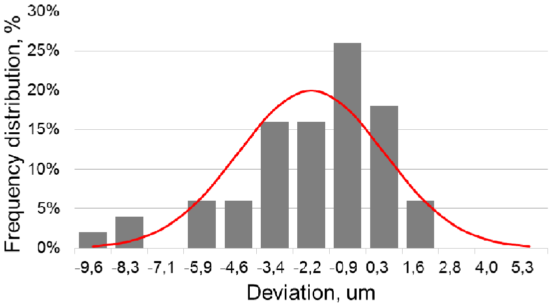

Figure 4.10: frequency distribution of differences of measurement results obtained in two positions (tilted, vertical) of the ball plate; results are limited to lengths measured along the y-axis.

4.4.2 Aluminum Hole Plate (AL1)

The aluminum hole plate AL1 was provided uncalibrated. Therefore, it was not possible to assess length measurement errors, but only to compute differences between lengths measured in the three different configurations listed in Section 4.3. Figures 4.11 and 4.12 show the 7 directions along which 5 length measurements are set. The arrows show the measurement directions on the hole plate. The length between the base hole and respective holes located in the indicated direction are measured. The base holes are illustrated as the filled circles. In each direction, both uni-directional and bi-directional lengths are assessed. For the evaluation of both kinds of lengths, 11 points illustrated in Figure 4.13 are defined on each hole.

Table 4.2 and 4.3 give more information about dimensions to be evaluated on the hole plate.

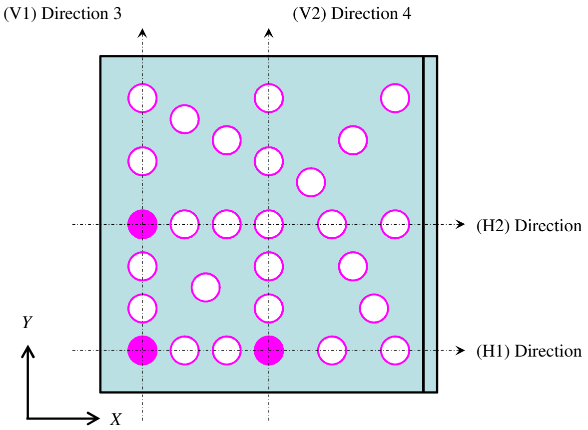

Figure 4.11: lengths measurement directions on the hole plate: 1 (H1), 2 (H2), 3 (V1) and 4 (V2). [59]

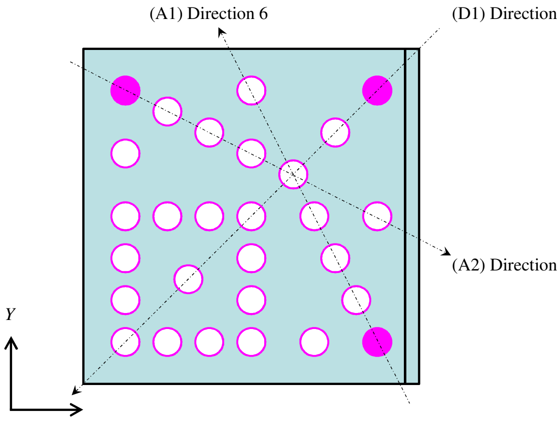

Figure 4.12: lengths measurement directions on the hole plate: 5 (D1), 6 (A1) and 7 (A2). [59]

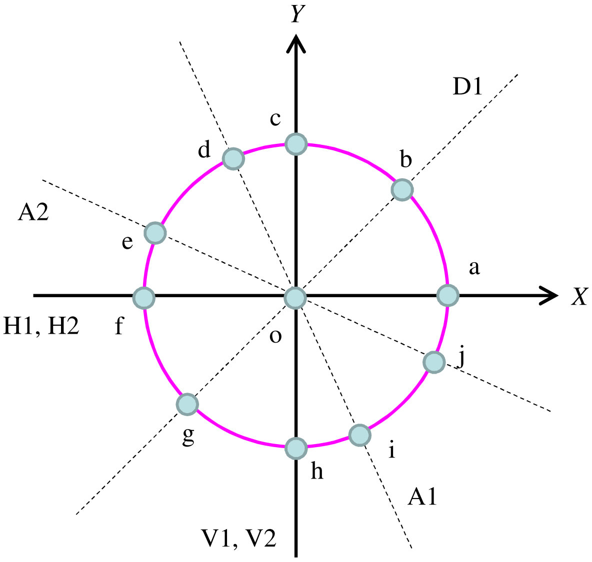

Figure 4.13: Circle of intersection between the mid-plane of the hole plate and a hole. Set of 11 identified points for each hole. [60]

Table 4.2: points of the holes related to respective lengths [60].

Direction 1 (H1)	Uni-directional length		Bi-directional length	
No.	From	To	From	To
1	*o*-1	*o*-2	*f*-1	*a*-2
2	*o*-1	*o*-3	*f*-1	*a*-3
3	*o*-1	*o*-4	*f*-1	*a*-4
4	*o*-1	*o*-5	*f*-1	*a*-5

5	*o*-1	*o*-6	*f*-1	*a*-6
Direction 2 (H2)	Uni-directional length		Bi-directional length	
No.	From	To	From	To
1	*o*-14	*o*-15	*f*-14	*a*-15
2	*o*-14	*o*-16	*f*-14	*a*-16
3	*o*-14	*o*-17	*f*-14	*a*-17
4	*o*-14	*o*-18	*f*-14	*a*-18
5	*o*-14	*o*-19	*f*-14	*a*-19
Direction 3 (V1)	Uni-directional length		Bi-directional length	
No.	From	To	From	To
1	*o*-1	*o*-7	*h*-1	*c*-7
2	*o*-1	*o*-11	*h*-1	*c*-11
3	*o*-1	*o*-14	*h*-1	*c*-14
4	*o*-1	*o*-21	*h*-1	*c*-21
5	*o*-1	*o*-26	*h*-1	*c*-26
Direction 4 (V2)	Uni-directional length		Bi-directional length	
No.	From	To	From	To
1	*o*-4	*o*-8	*h*-4	*c*-8
2	*o*-4	*o*-12	*h*-4	*c*-12
3	*o*-4	*o*-17	*h*-4	*c*-17
4	*o*-4	*o*-22	*h*-4	*c*-22

5	*o*-4	*o*-27	*h*-4	*c*-27
Direction 5 (D1)	Uni-directional length		Bi-directional length	
No.	From	To	From	To
1	*o*-28	*o*-24	*b*-28	*g*-24
2	*o*-28	*o*-20	*b*-28	*g*-20
3	*o*-28	*o*-17	*b*-28	*g*-17
4	*o*-28	*o*-10	*b*-28	*g*-10
5	*o*-28	*o*-1	*b*-28	*g*-1
Direction 6 (A1)	Uni-directional length		Bi-directional length	
No.	From	To	From	To
1	*o*-6	*o*-9	*i*-6	*d*-9
2	*o*-6	*o*-13	*i*-6	*d*-13
3	*o*-6	*o*-18	*i*-6	*d*-18
4	*o*-6	*o*-20	*i*-6	*d*-20
5	*o*-6	*o*-27	*i*-6	*d*-27
Direction 7 (A2)	Uni-directional length		Bi-directional length	
No.	From	To	From	To
1	*o*-26	*o*-25	*e*-26	*j*-25
2	*o*-26	*o*-23	*e*-26	*j*-23
3	*o*-26	*o*-22	*e*-26	*j*-22
4	*o*-26	*o*-20	*e*-26	*j*-20

5	*o*-26	*o*-19	*e*-26	*j*-19

Table 4.3: Dimensions to be evaluated on the hole plate [60].

Uni-directional lengths (centre-to-centre distance)			
<Uni_H1> 1	<Uni_H2> 1	<Uni_V1> 1	<Uni_V2> 1
<Uni_H1> 2	<Uni_H2> 2	<Uni_V1> 2	<Uni_V2> 2
<Uni_H1> 3	<Uni_H2> 3	<Uni_V1> 3	<Uni_V2> 3
<Uni_H1> 4	<Uni_H2> 4	<Uni_V1> 4	<Uni_V2> 4
<Uni_H1> 5	<Uni_H2> 5	<Uni_V1> 5	<Uni_V2> 5
<Uni_D1> 1	<Uni_A1> 1	<Uni_A2> 1	
<Uni_D1> 2	<Uni_A1> 2	<Uni_A2> 2	
<Uni_D1> 3	<Uni_A1> 3	<Uni_A2> 3	
<Uni_D1> 4	<Uni_A1> 4	<Uni_A2> 4	
<Uni_D1> 5	<Uni_A1> 5	<Uni_A2> 5	
Bi-directional lengths (point-to-point distance)			
<Bi_Ext_H1> 1	<Bi_Ext_H2> 1	<Bi_Ext_V1> 1	<Bi_Ext_V2> 1
<Bi_Ext_H1> 2	<Bi_Ext_H2> 2	<Bi_Ext_V1> 2	<Bi_Ext_V2> 2
<Bi_Ext_H1> 3	<Bi_Ext_H2> 3	<Bi_Ext_V1> 3	<Bi_Ext_V2> 3
<Bi_Ext_H1> 4	<Bi_Ext_H2> 4	<Bi_Ext_V1> 4	<Bi_Ext_V2> 4
<Bi_Ext_H1> 5	<Bi_Ext_H2> 5	<Bi_Ext_V1> 5	<Bi_Ext_V2> 5
<Bi_Ext_D1> 1	<Bi_Ext_A1> 1	<Bi_Ext_A2> 1	

<Bi_Ext_D1> 2	<Bi_Ext_A1> 2	<Bi_Ext_A2> 2	
<Bi_Ext_D1> 3	<Bi_Ext_A1> 3	<Bi_Ext_A2> 3	
<Bi_Ext_D1> 4	<Bi_Ext_A1> 4	<Bi_Ext_A2> 4	
<Bi_Ext_D1> 5	<Bi_Ext_A1> 5	<Bi_Ext_A2> 5	

Uni-directional length measurements

Figure 4.14 compares the results obtained measuring the hole plate in tilted position and in vertical position. Figure 4.15 compares the results obtained measuring the hole plate with and without an aluminum block added (both measurements are in tilted position).

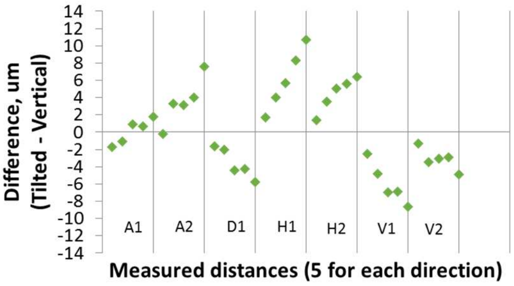

Figure 4.14: Differences of (uni-directional) length measurements obtained measuring the hole plate in two different positions (tilted, vertical).

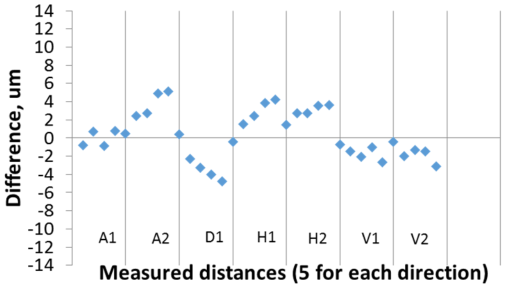

Figure 4.15: Differences of (uni-directional) length measurements obtained measuring the hole plate with and without an aluminium block added (both measurements are in tilted position).

For each direction (A1, A2, D1, H1, H2, V1, V2) there is an ascending trend (of the absolute values) of the length differences: as expected, this shows that differences are larger for larger lengths.

It must be noticed that these differences are higher when we compare two different positions of the hole plate (tilted and vertical; Figure 4.16), than when we consider a change in the material thickness of the object in the same position (tilted; see Figure 4.17).

In both cases we have small mean values (0.24 µm and 0.3 µm), with standard deviations equal to 4.77 µm and to 2.63 µm respectively. Maximum difference is larger in the first case (10.8 µm), with 95% of the differences included in the range [-9.3, 9.8] µm. In the second case the maximum difference is 5.2 µm and 95% of the differences are included in the range [-5, 5.6] µm. Based on differences between measurement results obtained in different configurations, one conclusion is that hole plate measurements seem influenced more by a change of sample position inside the measurement volume than by an increment of the total thickness to be penetrate by the x-ray beam: variability is approximately doubled in the first case.

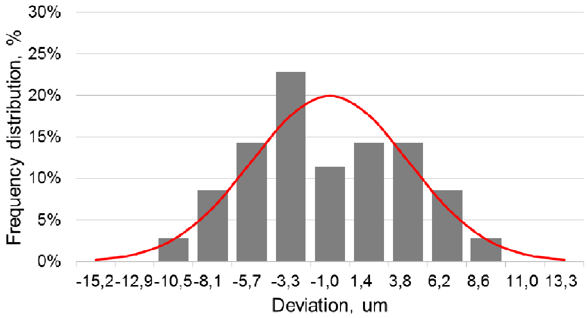

Figure 4.16: frequency distribution of differences of (uni-directional) length measurements obtained measuring the hole plate in two different positions (tilted, vertical)

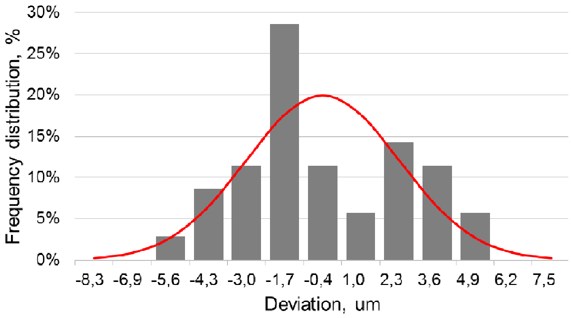

Figure 4.17: frequency distribution of differences of (uni-directional) length measurements obtained measuring the hole plate with and without an aluminium block added (both measurements are in tilted position)

Since ball plate and hole plate uni-directional measured lengths are similar (between 6 and 40 mm), they can be compared.

Comparing Figure 4.8 and Figure 4.16, shows that differences are larger in the case of the hole plate than in the case of the ball plate (range is [-8, 5.4] µm in Figure 4.8, while it is [-10.5, 11] µm in Figure 4.16). One possible explanation is the material influence: the ball plate has negligible material effect, while the aluminum hole plate has a higher material influence.

As explained before (section 4.3.1), for the ball plate the differences of distances measured along y-axis have a larger variability range (from -8 to 5.4 µm) than those along x-axis (from -1.4 to 4.7 µm). For the hole plate the situation is different: as shown in Figures 4,18 and 4.19, the differences of center-to-center distances measured along x-axis are positive (from 0.5 to 11.4 µm), while those along y-axis are negative (from -9.5 to -0.7 µm), but with similar range.

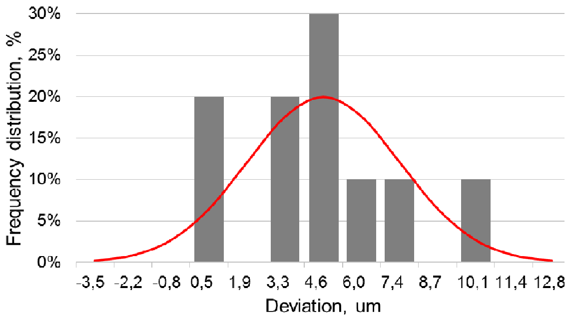

Figure 4.18: frequency distribution of differences of (uni-directional) length measurements obtained measuring the hole plate in two different positions (tilted, vertical); results shown here are limited to lengths measured along the x-axis.

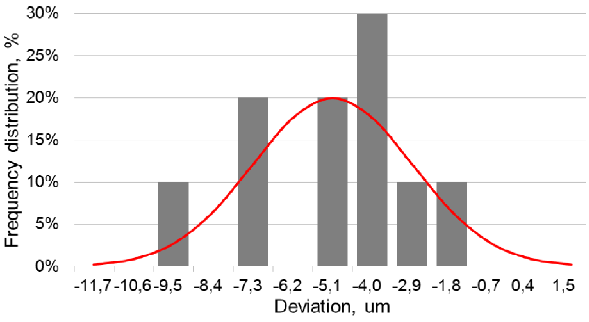

Figure 4.19: frequency distribution of differences of (uni-directional) length measurements obtained measuring the hole plate in two different positions (tilted, vertical); results shown here are limited to lengths measured along the y-axis.

Figures 4.20, 4.21 and 4.22 show the same results already shown in Figure 4.15, but subdivided in the three following categories:

- distances between holes not covered by the block (Figure 4.20);
- distances between holes covered by the block (Figure 4.21);
- distances between holes partially covered by the block (Figure 4.22).

The ranges of differences of all three Figures are similar; therefore, no clear effect of adding the block is visible.

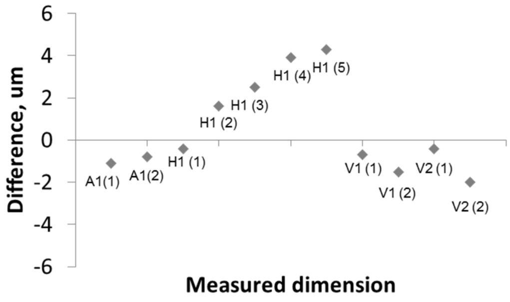

Figure 4.20: Differences of (uni-directional) length measurements obtained measuring the hole plate with and without an aluminium block added (both measurements are in tilted position); this figure shows only the distances between the holes that are not covered by the block when the block is added.

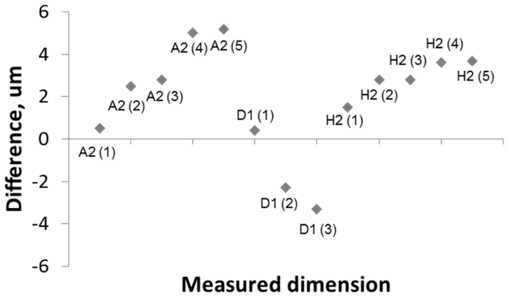

Figure 4.21: Differences of (uni-directional) length measurements obtained measuring the hole plate with and without an aluminium block added (both measurements are in tilted position); this figure shows only the distances between the holes that are covered by the block when the block is added.

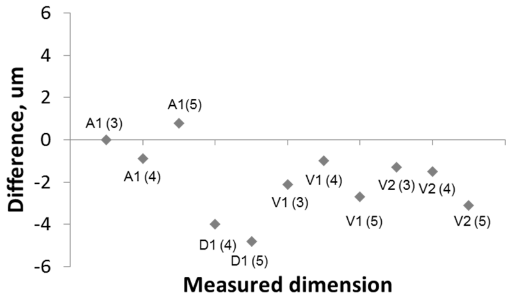

Figure 4.22: Differences of (uni-directional) length measurements obtained measuring the hole plate with and without an aluminium block added (both measurements are in tilted position); this figure shows only the distances that are partially covered by the block when the block is added.

Bi-directional length measurements

Figure 4.23 compares the bi-directional results obtained measuring the hole plate in tilted position and in vertical position. Figure 4.24 compares the bi-directional results obtained measuring the hole plate with and without an aluminum block added (both measurements are in tilted position).

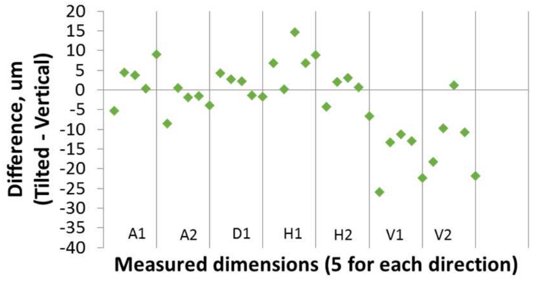

Figure 4.23: Differences of (bi-directional) length measurements obtained measuring the hole plate in two different positions (tilted, vertical).

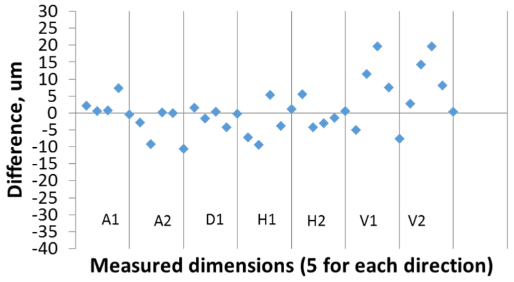

Figure 4.24: Differences of (bi-directional) length measurements obtained measuring the hole plate with and without an aluminium block added (both measurements are in tilted position).

Comparing Figures 4.23 and 4.24 with Figures 4.14 and 4.15, it can be noticed that bi-directional measurements show a higher variability than uni-directional ones, as expected.

As for uni-directional length measurements, also for bi-directional length measurements of the hole plate, differences are higher when we compare two different positions of the hole plate (tilted and vertical; Figure 4.23) than when we consider a change in the material thickness of the object in the same position (tilted; see Figure 4.24).

In the first case (tilted position compared with vertical position), the average difference is equal to -3.14 μm, the standard deviation is 9.36 μm, and 95% of the differences are included in the range [-21.9, 15.6] µm. Frequency distribution of differences is reported in Figure 4.25.

In the second case (with and without aluminum block), the average difference is 1.09 µm, the standard deviation is 7.21 µm, and 95% of the differences are included in the range [-13.3, 15.5] µm. Frequency distribution of differences is reported in Figure 4.26.

The differences of uni-directional distances measured along x-axis are in a positive range (Figure 4.18), while those along y-axis are in a negative range (Figure and 4.19). This trend is similar, but less evident, for bi-directional distances: distances along the x-axis have differences in the range [-7.2, 16.7] µm (Figure 4.27); while distances along the y-axis have differences in the range [-27.6, 2.3] µm (Figure 4.28).

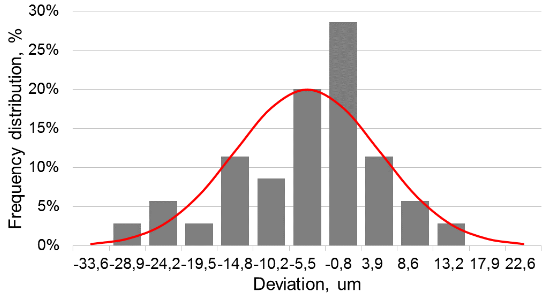

Figure 4.25: frequency distribution of differences of (bi-directional) length measurements obtained measuring the hole plate in two different positions (tilted, vertical).

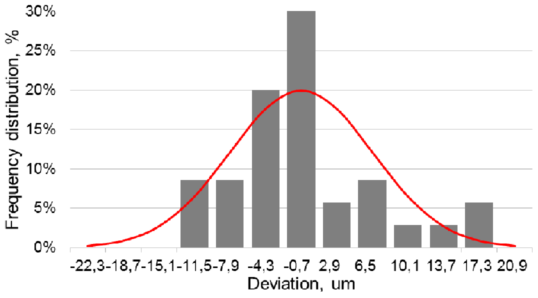

Figure 4.26: frequency distribution of differences of (bi-directional) length measurements obtained measuring the hole plate with and without an aluminium block added (both measurements are in tilted position)

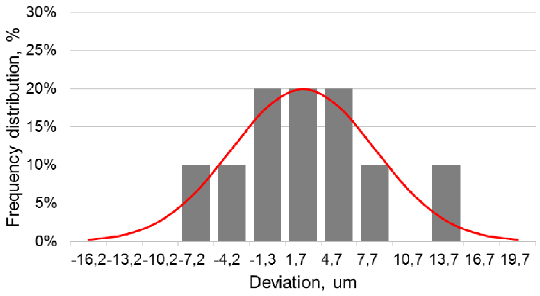

Figure 4.27: frequency distribution of differences of (bi-directional) length measurements obtained measuring the hole plate in two different positions (tilted, vertical); results shown here are limited to lengths measured along the x-axis.

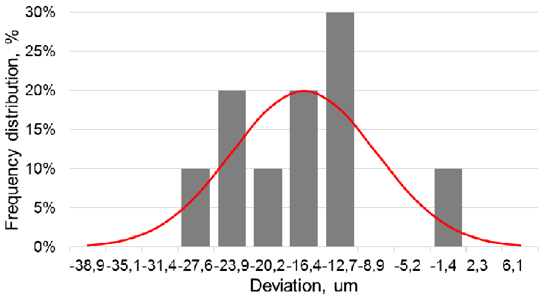

Figure 4.28: frequency distribution of differences of (bi-directional) length measurements obtained measuring the hole plate in two different positions (tilted, vertical); results shown here are limited to lengths measured along the y-axis

Furthermore, it can be noticed that in both comparisons (Figure 4.23 and Figure 4.24) the largest differences were registered along vertical directions (V1 and V2). This is particularly evident in Figure 4.23, where the maximum absolute values of differences exceed 20 µm for distances V1 and V2. The main cause of this influence on vertical distances can be explained with the Feldkamp effect. Figures 4.29 and 4.30 show deviations colored maps of each cylinder associated to the fitted elementary geometry: red areas highlight errors associated with this Feldkamp effect. For the vertical position of the hole plate (Figures 4.29) these errors are concentrated on the top and on the bottom of the cylinders. For the tilted position (Figures 4.30) the errors are more distributed on the cylinder surface.

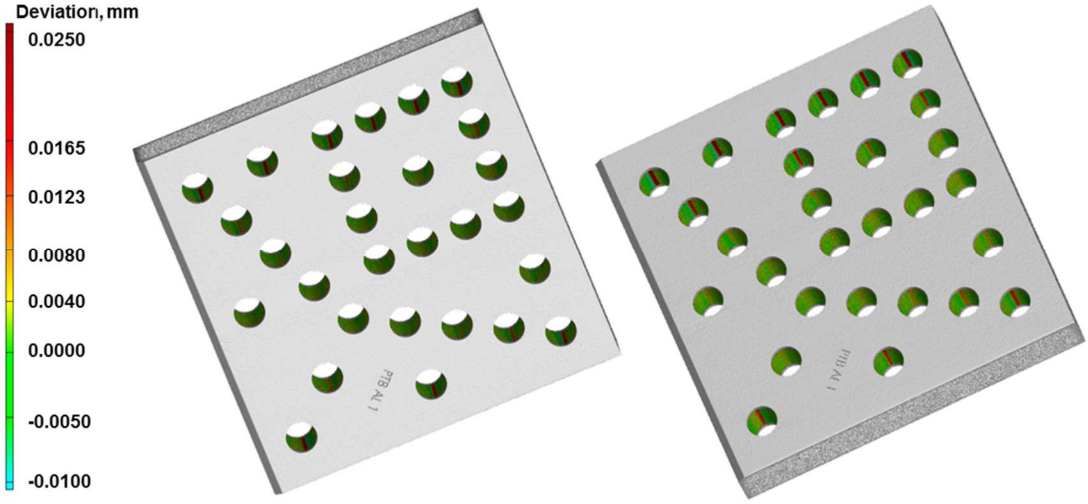

Figure 4.29: Feldkamp effect; vertical position (2 views)

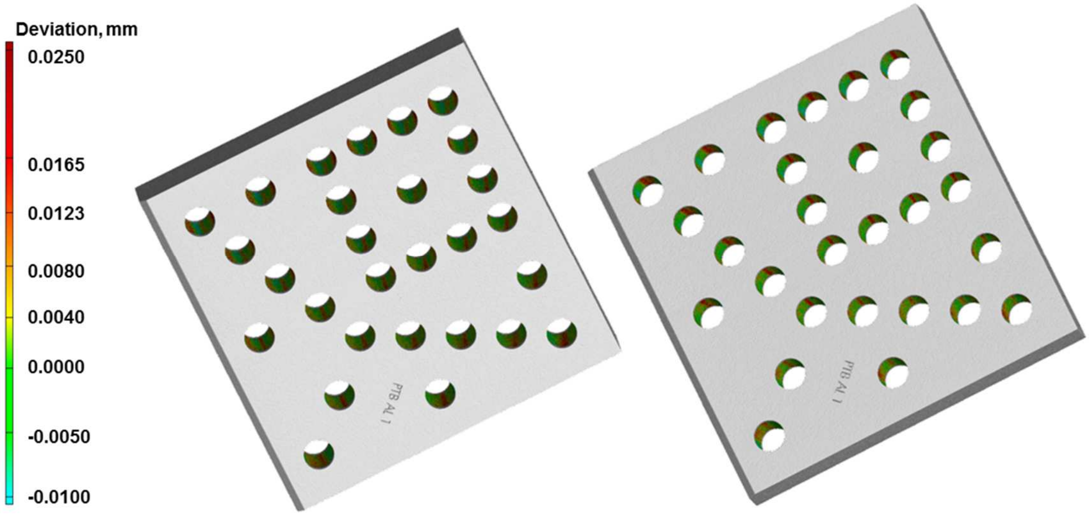

Figure 4.30: Feldkamp effect; tilted position (2 views)

Figures 4.31, 4.32 and 4.33 show the same results already shown in Figure 4.24, but subdivided in the three following categories:

- distances between holes not covered by the block (Figure 4.31);
- distances between holes covered by the block (Figure 4.32);
- distances between holes partially covered by the block (Figure 4.33).

The ranges of differences of all three Figures are similar; therefore, no clear effect of adding the block is visible.

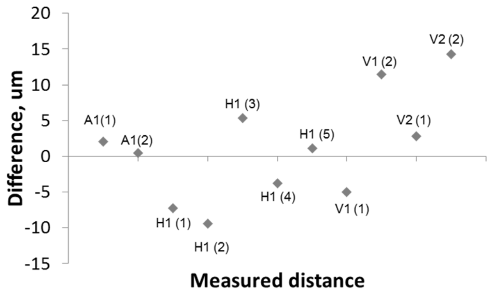

Figure 4.31: Differences of (bi-directional) length measurements obtained measuring the hole plate with and without an aluminium block added (both measurements are in tilted position); this figure shows only the distances between the holes that are not covered by the block when the block is added.

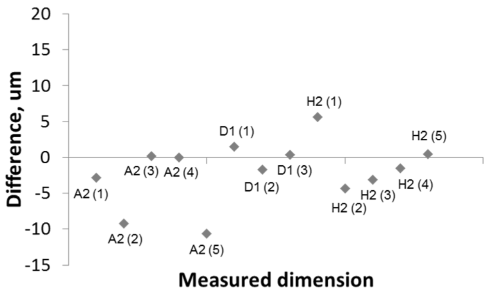

Figure 4.32: Differences of (bi-directional) length measurements obtained measuring the hole plate with and without an aluminium block added (both measurements are in tilted position); this figure shows only the distances between the holes that are covered by the block when the block is added.

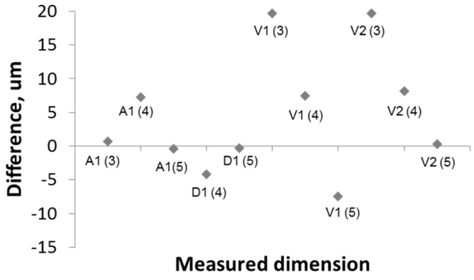

Figure 4.33: Differences of (bi-directional) length measurements obtained measuring the hole plate with and without an aluminium block added (both measurements are in tilted position); this figure shows only the distances that are partially covered by the block when the block is added

4.4.2.1 Beam hardening correction effect

Two different beam hardening corrections were applied for each of the three configurations of the hole plate, for comparing their influence on measurement results. The following two correction (BHC) presets were applied, as implemented in CT PRO 3D reconstruction software:

- preset 1: $y = x$ (no correction)
- preset 2: $y = 0.75x + 0.25 x^2$

The results shown in previous sections of this chapter refer to BHC preset 1, which was the optimal choice (no cupping effect was observed in gray value profiles) for all the scans considered in this work.

Uni-directional length measurements

Figures 4.34, 4.35 and 4.36 show the differences between BHC preset 1 and BHC preset 2, respectively for the three configurations considered in this work, in the case of uni-directional length measurements. From these figures it is clear that for uni-directional length measurements the differences between BHC preset 1 and BHC preset 2 are small: always less than 1.2 µm.

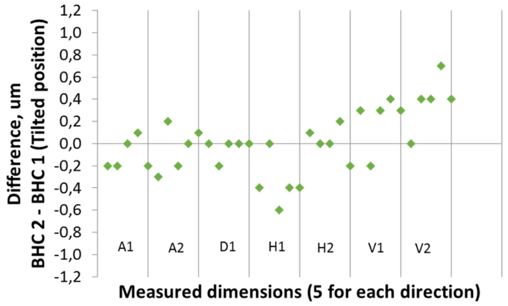

Figure 4.34: Differences between BHC preset 2 and BHC preset 1 for the hole plate measured in tilted position, for the case of uni-directional length measurements.

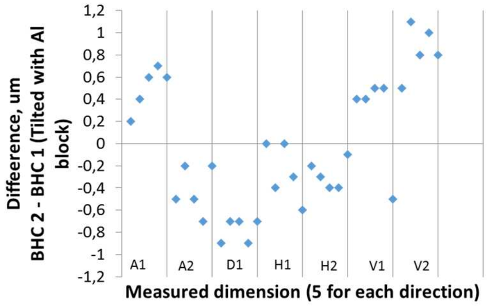

Figure 4.35: Differences between BHC preset 2 and BHC preset 1 for the hole plate measured with the added aluminium block, for the case of uni-directional length measurements.

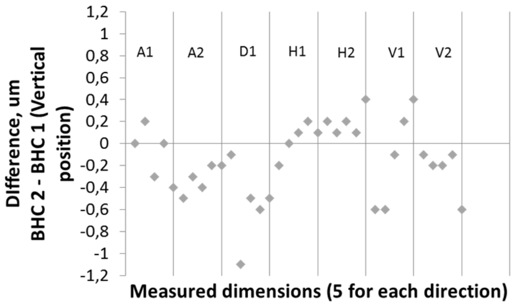

Figure 4.36: Differences between BHC preset 2 and BHC preset 1 for the hole plate measured in vertical position, for the case of uni-directional length measurements.

Bi-directional length measurements

Figures 4.37, 4.38 and 4.39 show the differences between BHC preset 1 and BHC preset 2, respectively for the three configurations considered in this work, in the case of bi-directional length measurements. The largest differences occurred for the hole plate in the tilted position (Figure 4.37).

Generally, bi-directional measurements show a larger variability than uni-directional measurements. In particular, distances along vertical directions (V1 and V2) show the largest variability (except for the vertical position of the hole plate).

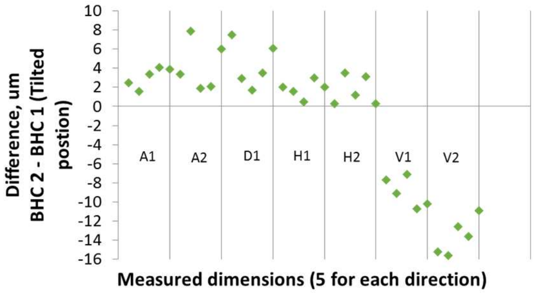

Figure 4.37: Differences between BHC preset 2 and preset 1 for the hole plate measured in tilted position, for the case of bi-directional length measurements.

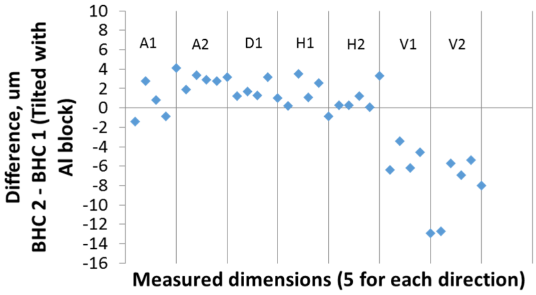

Figure 4.38: Differences between BHC preset 2 and BHC preset 1 for the hole plate measured with the added aluminium block, for the case of bi-directional length measurements.

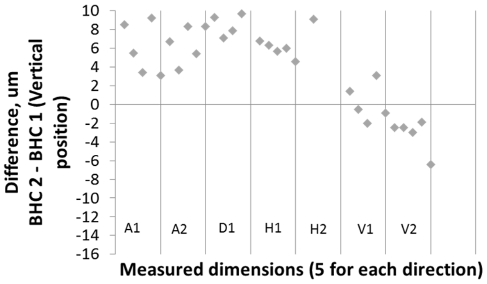

Figure 4.39: Differences between BHC preset 2 and BHC preset 1 for the hole plate measured in vertical position, for the case of bi-directional length measurements.

4.5 Conclusions

The main intent of this study, performed within the ISO TC 213 WG 10 experimental study on material influence in dimensional computed tomography (CT), was to demonstrate if there are major additional length measurement errors resulting from material effect that are not covered by the current testing procedure using hole plate measurements.

Two reference objects were used in this study:

1. uncalibrated hole plate made from aluminum (AL1; size 48 mm x 48 mm x 8 mm) borrowed from PTB;
2. calibrated ball plate with a regular 5 x 5 array of ruby spheres glued on a 2 mm thick carbon fiber plate (size 50 mm x 50 mm x 2 mm), manufactured and calibrated by DTU.

The second object (ball plate) was chosen because of its dimensions and measurable lengths similar to those of the hole plate, in order to compare the results of an object with negligible material effect (ball plate) with another one sensitive to material influence (hole plate).

Using the calibrated CT ball plate, it was possible to determine length measurement errors for the CT system under test. Such errors were then compared to the maximum permissible length measurement error (MPE) stated by the CT manufacturer. Tests showed that sphere-to-sphere distance errors are well within MPE limits for the CT systems used in this work.

Since the hole plate was provided uncalibrated, it was not possible to assess length measurement errors, but in this case it was possible to compute differences between lengths measured in different configurations of the object. The three different configurations reported in this report were:

- tilted position (45 degrees);
- tilted position (45 degrees) with an added aluminum block;
- vertical position.

CT scans of the three configurations were at the same magnification and with the same acquisition parameters.

CT measurement results obtained from the hole plate produced the following main results:

- A position change of the sample (vertical to tilted) produced significant variability of length measurement results, while the variability of results was not visibly influenced by adding a 10 mm thick aluminum block to the hole plate. This holds both for uni-directional and bi-directional length measurements.
- Bi-directional length measurements were subject to a higher variability than uni-directional ones.
- Uni-directional length measurements obtained from the hole plate were subject to a higher variability than corresponding measurements obtained from the hole plate; this was due to the negligible material effect of the ball plate compared to the hole plate.
- The Feldkamp effect had a significant influence especially on bi-directional length measurements in vertical direction (V1 and V2) of the hole plate.
- Different beam hardening corrections produced visible effects on bi-directional length measurements, while their effects were negligible for uni-directional length measurements.

These results, together with results obtained by other research institutions which took part to the test survey, contributed to define the final procedure for the evaluation of CT length measurement errors. In particular, it was possible to conclude that hole plate measurement can find applicability as reference standard for length measurement tests, where the material effect —which can severely degrade the quality of CT measurements of workpieces— can be clearly identified in a CT acceptance and reverification testing procedure [61]. This effect does not change observed unidirectional length measurement errors significantly, but can be clearly recognized when bidirectional length measurement errors are analyzed.

Chapter 5

Image quality and metrological structural resolution of CT systems

This chapter deals with the image quality of 2D projection images acquired by CT and with the metrological structural resolution (MSR). In particular, focal spot drift and size were evaluated and the 'Hourglass' method for MSR evaluation was improved and compared with other proposed methods. Finally, influence factors affecting the 'Hourglass' method were identified and quantified.

5.1 Resolution concepts and definitions

Resolution is the capability of a measuring device to separately measure physical quantities of the same dimensions [31]. In imaging systems, the resolution is strictly connected to the image quality concept, which deals with the reproduction accuracy of an imaged object. This accuracy depends on how “sharp” are the acquired images or, in other terms, on the blurring content, described by the point spread function (PSF) of the system [62] (see Figure 5.1). An image I results from the convolution of the object function $O(x, y, z)$ with PSF; noise and possible artifacts, which can worsen the image quality too, will be superimposed on this image:

$$I(x,y,z) = K \cdot O(x,y,z) * (PSF(x,y,z) + noise + artifacts) \qquad \text{(Eq. 5.1)}$$

where K is an energy-dependent contrast factor.

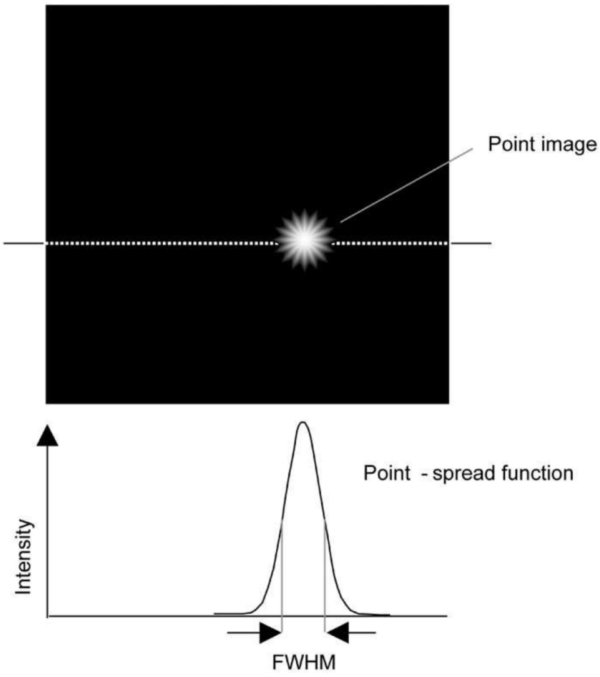

Figure 5.1: The image of a point source and its resulting one-dimensional point spread function. The full width at half maximum (FWHM) is indicated [63]

Since many years, resolution of optical and imaging systems has been discussed and many definitions have been proposed. One of the oldest and best known resolution criteria was given by Lord Rayleigh in 1896: it states that the presence of two sources will be discerned if the diffraction maximum of one source lies at the diffraction minimum of the second [22]. If the two sources are closer, they cannot be distinguished from a single light source and the detail will be lost (Figure 5.2). According to Rayleigh Criterion the angular resolution of a lens of diameter D is given by:

$$\theta_{Rayleigh} = 1.2197 \cdot \frac{\lambda}{D} \qquad \text{(Eq. 5.2)}$$

where λ is the radiation wavelength.

This criterion was then improved by C. Sparrow [22]:

$$\theta_{Sparrow} = 0.947 \cdot \frac{\lambda}{D} \qquad \text{(Eq. 5.3)}$$

For this latter definition, as the distance between two sources is decreased, the central minimum that exists between two peaks at the Rayleigh criterion disappears.

The resolution is thus dependent on the distance between the two sources and the aperture of the imaging system. In other words, the resolution will be limited by the width of the point spread function of the imaging system.

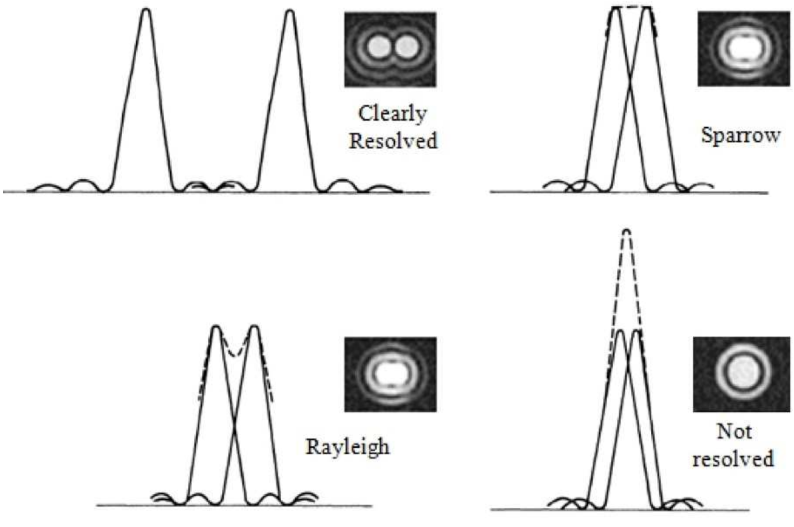

Figure 5.2: The Raleigh and Sparrow criteria for overlapping point images [64]

The classical criterion of Rayleigh measures the spatial resolution, which is the capability of an imaging system to display fine details separately.

The concept of spatial resolution can be applied also to CT systems, and sometime is referred to the total geometrical unsharpness U_{TOT}, which depend mainly on the focus size, focus movement/drift during scanning, the detector element spacing and aperture and reconstruction algorithm [62].

Other research works ([65, 66, 67]) adopted a simplified evaluation of the geometrical unsharpness, taking into account the most dominant factors, such as focus size, detector system and scanner geometry:

$$U_{TOT} = \sqrt{U_F^2 + U_D^2} \qquad \text{(Eq. 5.4)}$$

$$U_F = \frac{m-1}{m} \cdot W_F \qquad U_D = \frac{W_D}{m}$$

with U_F geometrical unsharpness associated with focus size, U_D geometrical unsharpness associated with the contrast transmission of the detector and m geometrical magnification. W_F is the focal spot size which is connected to the X-ray tube power and W_D is detector image unsharpness experimentally evaluated to be twice the pixel size [68]. The focal spot size is usually approximate to increase of 1 µm when the power increases of 1W. This approximation is necessary especially for micro-focus tubes, for which a recognized procedure to estimate the focal spot size and shape has not been defined yet.

Spatial resolution is also determined sometimes by direct measurements, e.g. hole and bar test patterns, some other times by indirect methods, such as the calculation of modulation transfer function (MTF) [62] (Figure 5.3).

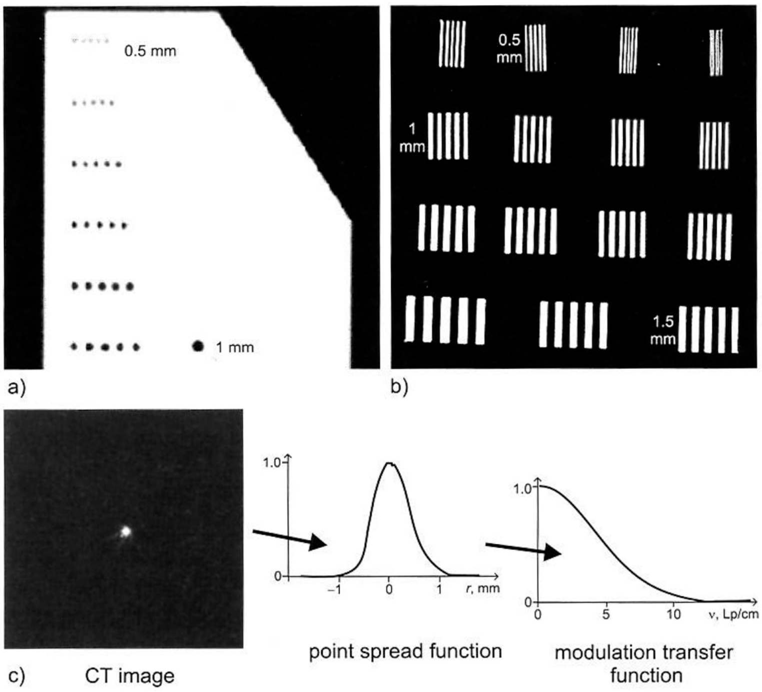

Figure 5.3: Various resolution tests and resulting images. a) Drilled hole pattern. b) Bar pattern. c) Wire Phantom for measurement of the point spread function (PSF) and calculation of the modulation transfer function MTF) [62].

Direct measurements are easy to be performed and interpreted, but the evaluation is based on mere qualitative criteria. To check whether a system conforms to the manufacturer's specifications, the MTF method is better suited. The MTF is the magnitude of the Fourier transformed point spread function (PSF) of the imaging device and describes how much contrast at a specific spatial frequency is maintained by the imaging process. In this case, the spatial resolution is specified in terms of spatial frequency for a given percent value of the MTF, which is often 10% as reported in [62]. Concerning CT measurements, the MTF defines a limit for the ability to detect a structure in the volume data. In analogy to the structural resolution of coordinate measuring systems, the ISO 15708:1 [69] describes the structural resolution in the grey scale range of voxels by the modulation transfer function (MTF). Several methods to assess this type of resolution were proposed by standards and guidelines [70, 71, 72].

The metrological structural resolution (MSR) for dimensional measurements in another characteristic, which describes the size of the smallest separately measurable structure. Since CT measurement data in dimensional measurements always undergo a threshold value process to obtain the relevant geometrical information, the structural resolution for dimensional measurements must in principle be distinguished from the structural resolution in the grey scale range of the voxels, since the structural resolution in the grey scale range of the voxels does not encompass the complete dimensional measurement chain, i.e. from 2D projections acquisition till surface determination and filtering operations [33].

Besides the abovementioned concepts of resolution, in literature and standards, the terminology about resolution of CT systems is not unambiguous. For this reason, Table 5.1 provides an attempt to summarize the main concepts and definitions with distinction between 2D radiographic projections and 3D reconstructed volume.

Table 3.1: Summary of the main resolution concepts and definitions, distinguished between 2D radiographic projections and 3D reconstructed volume.

Resolution definitions	
1) 2D radiographic projections	
Image quality	**Total image unsharpness** *The penumbral shadow (blurring) in a radiological image.* Dependent upon (i) focal spot size, (ii) source to object distance and (iii) object to detector distance. **Synonyms** Blurring, Geometrical unsharpness
	Modulation transfer function (MTF) P*roperty of a CT unit of recognizably reproducing objects of low contrast relative to homogeneous surroundings*.
	Contrast sensitivity *A measure of the minimum percentage change in an object which produces a perceptible density/brightness change in the radiological image.* Dependent upon (i) signal-to-noise ratio and (ii) blurring.

2) 3D reconstructed volume	
Structural resolution in the grey range scale of voxels	**Spatial resolution** *Smallest separation at which two points can be distinguished as separate entities.*
	Total image unsharpness *The penumbral shadow (blurring) in a CT reconstructed volume.* Dependent upon (i) focal spot size, (ii) source to object distance, (iii) object to detector distance, (iv) detector element spacing and aperture, (v) focal spot drift during scanning and (vi) reconstruction algorithm. **Synonyms** Blurring, Geometrical unsharpness
	Modulation transfer function (MTF) *The specified characteristic of the Modulation Transfer Function (MTF) at 10% modulation, using the unit line-pairs per mm (lp/mm), defines a limit for the ability to detect a structure in the volume data of a CT measurement.*
Metrological structural resolution	*The size of the smallest structure that can still be measured dimensionally at a given measuring field size.* Dependent upon (i) focal spot size, (ii) source to object distance, (iii) object to detector distance, (iv) detector element spacing and aperture, (v) focal spot drift during scanning, (vi) reconstruction algorithm, (vii) surface determination procedure and (viii) filtering operations.
Positional resolution	*Smallest measurable displacement in space in the measured direction (x, y and z).* The positional resolution is contained in the specifications for length measurements and probing measurements.
Contrast resolution	*Capability to distinguish details at low contrast.* Dependent upon (i) signal-to-noise ratio and (ii) spatial resolution. **Synonyms** Density resolution, Contrast sensitivity, Low-contrast resolution

5.2 Experimental investigations on the focal spot

Among the many sources of instability of an X-ray system, the X-ray tube is a major error source. Focal spot size and focal spot drift are two factors which have a relevant influence on the spatial resolution of CT systems.

As explained in Chapter 2 of this thesis, an X-ray beam generated by an X-ray source reaches an X-ray detector after being attenuated by its interaction with the object material. In the ideal case of X-ray beam departing from a single point, the obtained projected image of the workpiece is completely sharp (Figure 5.4-a). However, in real cases, the X-ray focal spot has always a finite size, causing images to be blurred (Figure 5.4-b). Moreover, although a higher magnification increases the image resolution (in terms of voxel size), it also causes images to have a higher blurring content (Figure 5.4-c).

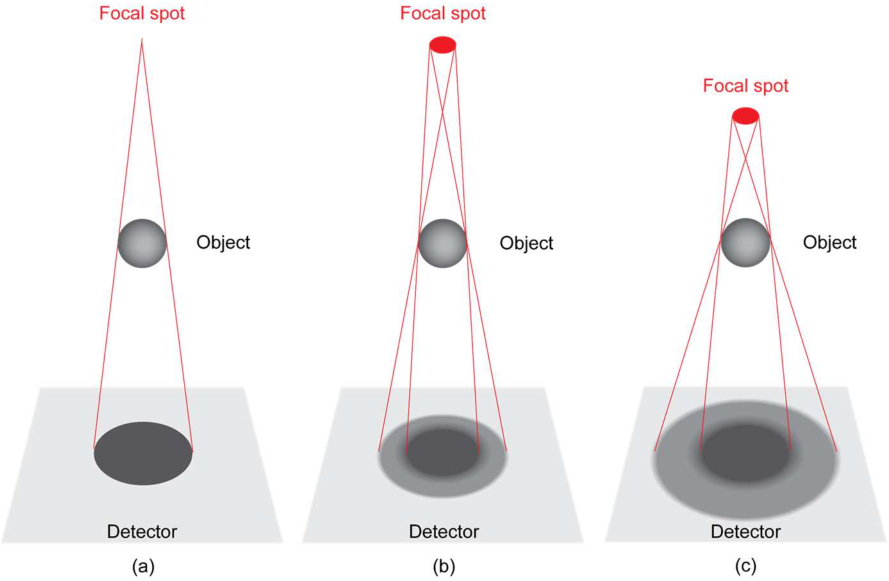

Figure 5.4: (a) Ideal focal emission point resulting in a totally-sharp projection image of the object; (b) a finite focal spot size causes the image to be blurred on the detector; (c) the blur increases with the geometric magnification.

Thus, a sufficiently small focal spot size is necessary in X-ray computed tomography (CT) in order to obtain high-resolution images and is required especially for analyzing micro-features and structures [12, 24]. During the production of X-rays, 99% of the electron beam energy is transformed to heat. Figure 5.5 shows a thermal image of an X-ray tube after a scan, which indicates that heat is generated at both the target and the X-ray tube which contains the coils to align and focus the beam [72]. The heat produced and the size of focal spot are directly related to the input voltage and current of the X-ray source [73]. Scans with higher power produce more heat than scans with lower power. For X-ray systems designed with a large focal spot, for example a focal spot of 1 millimeter diameter, the influence from heat generation may not be significant. However, when the diameter of a focal spot is a few micrometers or less, the incident power per unit area on the target surface can be extremely high [72]. Excessive heat generated over a small area can pit and even melt a target material. The heat generated can cause a change in the geometry of the X-ray tube, which can manifest itself as a 'drift' of the focal spot [74]. Such a drift leads to instability in the imaging geometry, introducing errors in the image reconstruction process and affecting the accuracy of dimensional measurements.

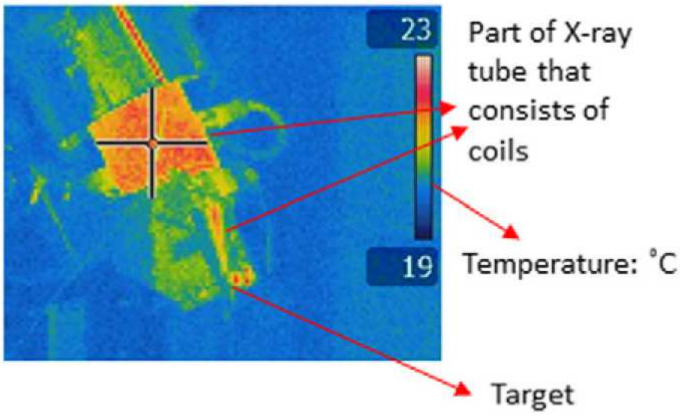

Figure 5.5: Thermal image of the X-ray tube of a Nikon Metrology MCT225 system [72].

In the following paragraphs, new methods to evaluate focal spot drift and size are presented and applied on the metrological CT system introduced in Section 1.4.1.

These tests were part of a collaborative work with the UK's National Measurement Institute (National Physical Laboratory, NPL).

5.2.1 Focal spot drift

The influence of focal spot drift on the positional stability of 2D projections is a relevant issue to be dealt with in CT dimensional metrology. As an example, Figure 5.6 shows how a positional change of the object projections caused by focal spot drift during the CT acquisition can affect the quality of the reconstructed volume.

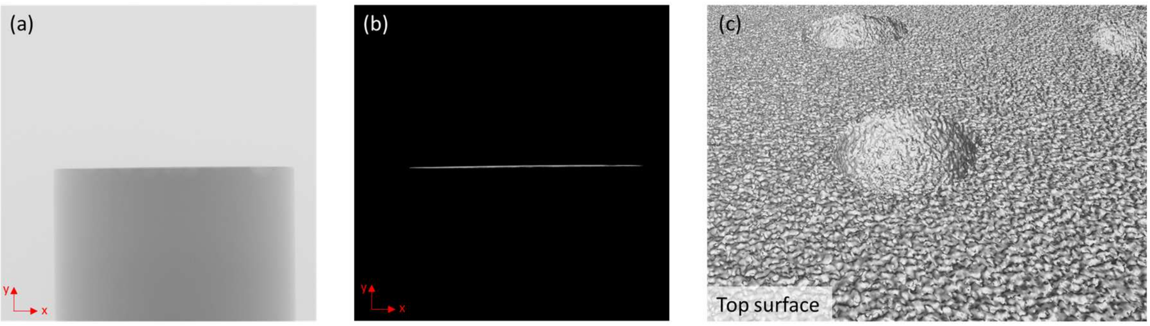

Figure 5.6: (a) First projection of an aluminum cylinder, part of 1500 projection images collected by CT acquisition. (b) Difference image between first and last projection, showing a focal spot drift along the y-axis. (c) Top surface of the reconstructed 3D volume characterized by high noise rate due to the focal spot drift.

The focal spot drift has been investigated experimentally, as well as using computer simulation techniques by several research works [75, 76, 77]. The most common approach is collecting a number of 2D projection of stationary reference objects over a period of time. Typical reference objects are spheres, hole plate and cross wire. In the ideal case, all the collected projected images should be exactly the same. Positional changes of the object are usually attributed to the drift of the focal spot, but there could be other causes, such as the mechanical rigidity of the X-ray tube-object-detector assembly, variations in the X-ray flux and electronic properties of the detector [74]. However, in [76] the focal spot drift was identified as the main contributor to the positional instability of 2D projections. Experimental studies were performed in collaboration with NPL in order to evaluate the focal spot drift and its correlation with thermal behavior.

5.2.1.1 Experimental set-up

<u>Temperature conditions</u>

Two identical CT system (Nikon MCT225) were used for the purpose. Both the two metrological CT systems used were characterized by liquid-cooled gun, temperature-controlled cabinet (20.0±1.0°C) and were located in air-conditioned rooms, where temperature was controlled to fit the specifications provided by the manufacturer (18-

25°C). For monitoring temperature fluctuations during drift tests, additional temperature sensors were added inside the systems:

- System #1: sensor 1 placed on the metal part of the X-ray tube right above the target, sensor 2 attached to the filter holder and sensor 3 attached to the water pipe below the target.
- System #2: sensor 1 attached to the metal part of the X-ray tube right above the target, sensor 2 as close as possible to the X-ray spot (filter holder) and sensor 3 in proximity of the detector.

Figure 5.7 shows the X-ray source of the Nikon MCT225 system.

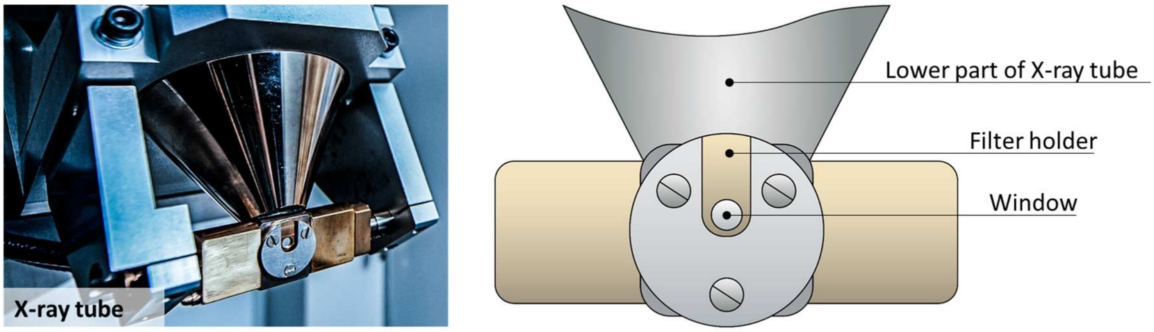

Figure 5.7: Particular of the X-ray tube of a Nikon MCT225 system (left) and sketch of the target assembly (right), showing the holder for physical filters and window for sealing the tube aperture.

Sample design

The sample design, sketched in Figure 5.8, consists of a steel sphere with 0.79 mm diameter embedded in a polyurethane cylinder of 10 mm diameter and 5,42 mm height.

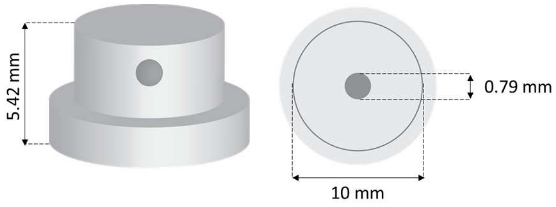

Figure 5.8: Steel sphere with diameter of 0.79 mm embedded in polyurethane cylinder. This design allows mounting the sample directly inside the filter holder of a Nikon MCT225 system.

This design allowed placing the sample directly inside the filter holder (Figure 5.7), which is in contact with the X-ray tube aperture (window). In this way, the magnification factor could be maximized and possible mechanical instabilities due to the manipulation system (e.g. rotary table) were minimized. The achieved magnification factor was 118, with voxel size of 1.7 µm. Moreover, the polyurethane was chosen as it absorbs less radiation than steel and, for this reason, does not disturb the edge detection operations on the projected spheres.

Image elaboration

After the acquisition of a number of 2D projection images over a certain period of time, they were analyzed in Matlab: a Canny edge detection algorithm [78] was applied and circles were fitted to the obtained edge coordinates by non-least squares circle fitting (Figure 5.9). The drift along x- and y-axis was evaluated through comparison of the circle center coordinates in all subsequent images, combined with the magnification factor.

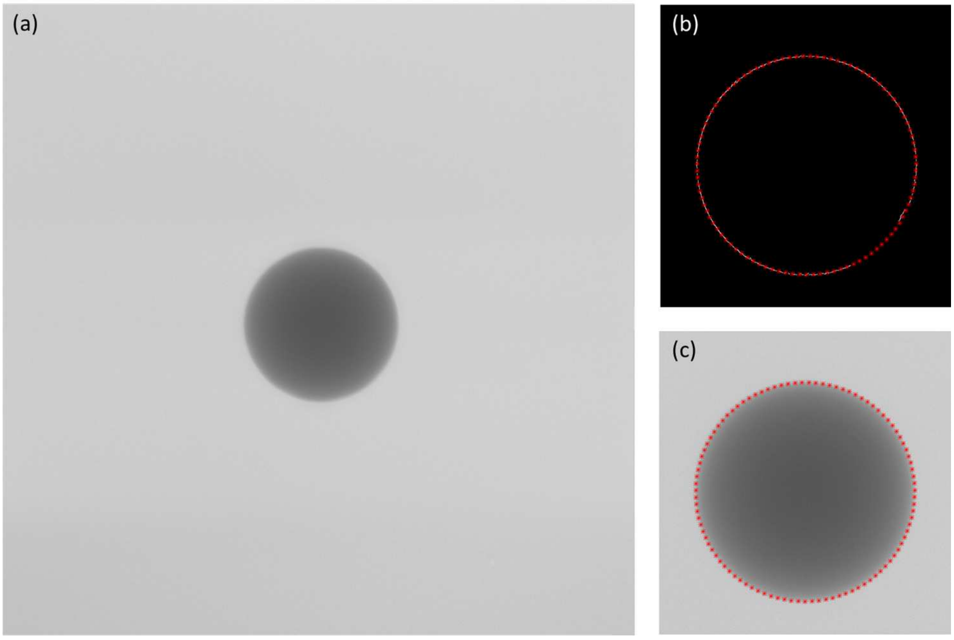

Figure 5.9: (a) 2D projection of 0.79 mm steel sphere; (b) application of Canny edge detection algorithm and circle fitted on edge coordinates; (c) determined fitted circle superimposed on the imaged sphere.

5.2.1.2 Results

The evaluation of focal spot drift was performed by taking into account different conditions of the employed CT systems. In particular, “cold” scans and “hot” scans were compared: a “cold” scan was conducted as first acquisition of the day without any previous warming-up of the system, while a “hot” scan was done with the system warmed-up. Moreover, besides considering the drift of a system with normal thermal behavior, it is also important to evaluate the drift of a system facing instability issues, as overheating of the X-ray tube leading to flux instability and increased noise. For this reason, the system #2 was tested right before the maintenance of the X-ray tube, which was required at that moment for extraordinary instable thermal conditions. In the following, results obtained by "cold" and "hot" scans on both good and bad behaving systems are summarized.

Normal thermal conditions (System #1)

Figure 5.10 and Figure 5.11 compare the focal spot (x, y) drift in a "cold" scan (3142 projections done as first acquisition of the day, without previous warming-up of the system) with the drift in a "hot" scan (9999 projections done with the system warmed-up). Each scan was performed with beam power equal to 6 Watts. The drift effect is very low in both scans (below 0.2 drift/pixels). As expected, a higher variation of (x, y) coordinates can be observed for the "cold" scan, while the "hot" scan has almost zero variability during the first 6000 projections (A typical high-quality CT scan is characterized by circa 3000 projections). An initial variation of temperature was recorded in the "cold" scan, while constant trends were registered in the "hot" scan for all the three sensors. The suggestion is to allow the X-tube to stabilize for an appropriate period of time (depending on the specific CT system) prior to image acquisition [74].

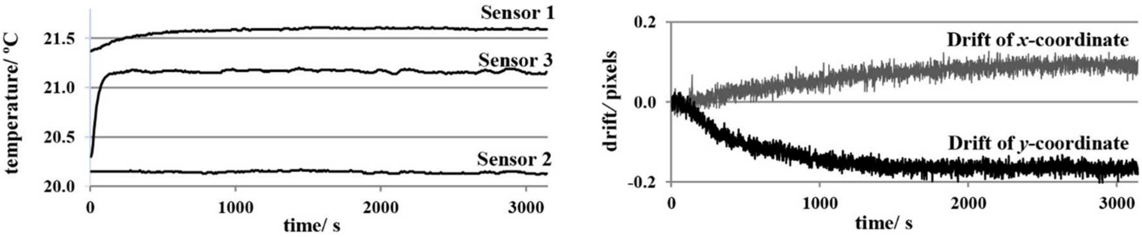

Figure 5.10: Temperature of the three sensors (left) and drift in the (x, y) center coordinates (right) in "cold" scan (3142 projections) obtained with system #1 [74].

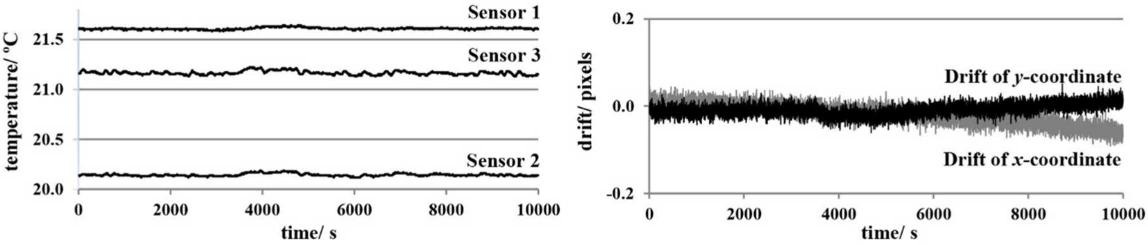

Figure 5.11: Temperature of the three sensors (left) and drift in the (x, y) center coordinates (right) in "hot" scan (9999 projections) obtained with system #1 [74].

Instable thermal conditions (System #2)

As anticipated above, system #2 was instable during the experiments due to thermal issues of the X-ray tube. As shown in Figure 5.12 and 5.13, a maximum drift of 0.7 pixels was measured for the "cold" scan (3142 projections done as first acquisition of the day, without previous warming-up of the system) and even higher than 1 pixel for the "hot" scan (3142 projections done after warming-up the system). In the first case, the X-ray tube has increased its temperature of about 1°C (Sensor 1). The temperature of the filter mount (holding up the sample) was relatively constant but too high with respect to the required temperature of 20°C. During the "hot" scan, all the monitored temperatures were more or less constant, but the drift effect nevertheless increased. The cause can be partially attributed to the temperature of the filter holder, which was higher with respect to the "cold" scan. However, besides the temperature, there were for sure other causes, as the abovementioned flux instability and high presence of noise. In fact, the drift trend is almost linear but with a very high-frequency variability.

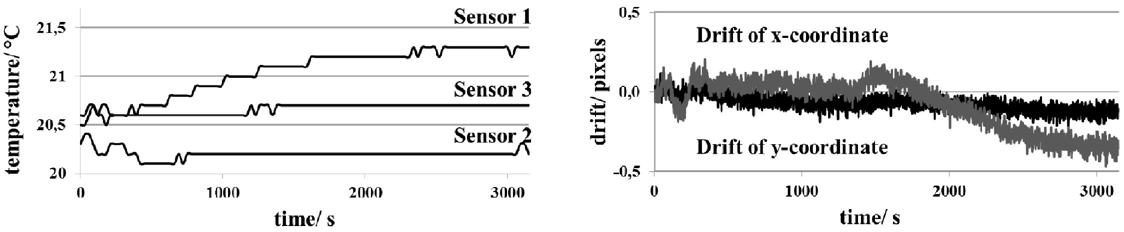

Figure 5.12: Temperature of the three sensors (left) and drift in the (x, y) center coordinates (right) in "cold" scan (3142 projections) obtained by system #2.

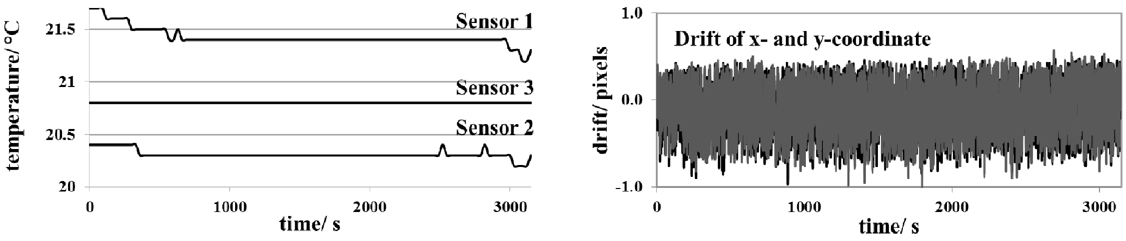

Figure 5.13: Temperature of the three sensors (left) and drift in the (x, y) center coordinates (right) in "hot" scan (3142 projections) obtained by system #2.

5.2.1.3 Conclusions

The focal spot drift in x- and y-axis was evaluated in two identical metrological CT systems (Nikon MCT225), here named system #1 and system #2. The first system was in normal operative conditions, while the second one was tested when facing instable thermal conditions. Experimental results showed that:

- in normal operative condition the maximum focal spot drift is below 0.2 pixels (circa 1/10 µm), and can be further improved with a previous warming-up of the X-ray source;
- in bad conditions (e.g. high temperature, thermal fluctuations, flux instabilities, noise) the average focal spot drift is equal to 1 pixel (circa 1.7 µm) considering both “cold” and “hot” scans.

5.2.2 Focal spot size

Several methods for assessing the effective focal spot size of X-ray sources are proposed in standards and guidelines [79, 80]. In particular, part 5 of EN 12543 [79] can be used to measure the size of focal spots of micro-focus X-ray tubes with size between 5 µm and 300 µm and energies up to 225 eV. In [81], it was demonstrated that there is no consistency among results obtained with different methods. Moreover, a standard test method is not yet available for X-ray tubes with focal spot size smaller than 5 micrometers, despite these tubes are increasingly used in industrial applications where the spatial resolution plays an important role for detecting and measuring very small features.

A promising approach is to compare the measurement result of a test object with a simulated measurement result [82]. For example, Taubenreuther [83] used a tungsten wire with diameter of 10 µm for evaluating spot sizes down to 3.3 µm. The parameters which determine the focal spot of a simulated measurement were varied until an optimal match between simulated and measured data was achieved. This method, as well as other methods [81, 83], applies the image convolution concept to describe the blurring of an acquired image and the deconvolution process to calculate the intensity distribution of the focal spot. Another proposed method, applying the same principle, chose a line pattern as test object [85].

This part of the thesis presents a new method for the determination of the effective focal spot size based on a similar approach, i.e. comparison of measurement and simulations results on test objects.

5.2.2.1 Description of the proposed method

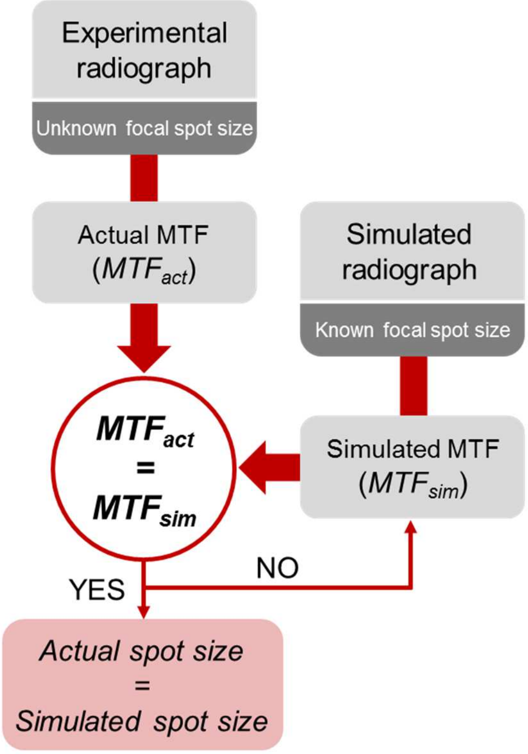

Figure 5.14: Schematic representation of the proposed method for evaluating the actual focal spot size of micro-focus X-ray sources.

The concept of the proposed method is illustrated in Figure 5.14. An experimental radiograph of a test object is obtained by CT acquisition of a single 2D projection. The actual focal spot size is unknown. In parallel, a number of simulated radiographs of the same test objects are generated with different dimensions of the focal spot. Each focal spot was simulated as a circle containing 81 equally-spaced points emitting X-rays. The MTF obtained from the actual radiograph has to be compared with those obtained from simulations. The final aim is to associate the focal spot size with the measured Modulation Transfer Function. When a match is found the actual focal spot size can be estimated to be equal to that specific simulated focal spot size.

5.2.2.2 Experimental set-up

A 0.25 mm-thick tungsten cutting edge (Figure 5.15) and a resolution chart with slit widths between 3 and 50 µm (JIMA RT RC-05 [86]; Figure 5.16-a,b) were used as test objects. Both samples were positioned on the rotary table as close as possible to the X-ray source in order to achieve a very high magnification and neglect the voxel size influence on spatial resolution. These objects were then imaged multiple times using different powers. Modulation Transfer Function (MTF) was evaluated at 10% of the contrast from the Edge Spread Function (ESF) obtained on the tungsten cutting edge projections, implementing in Matlab the method proposed by Samei et al. [87] (see Figure 5.15). Experimental data were then compared with simulated radiographs of a tungsten edge, obtained with different dimensions of the focal spot ranging from 3 µm to 24 µm. The optimal match between measured and simulated MTF was identified. The JIMA test chart was used for validation of the method, following the same steps. With the JIMA chart, the spatial resolution can be directly evaluated by a qualitative analysis or from extracted intensity profiles by applying the Rayleigh criterion as resolution limit (Figure 5.16-b,c). Since the focal spot size becomes larger as the X-ray power increases, several powers were tested: 2, 4, 6, 8, 10 and 12 Watts (W), with fixed voltage (80 kV).

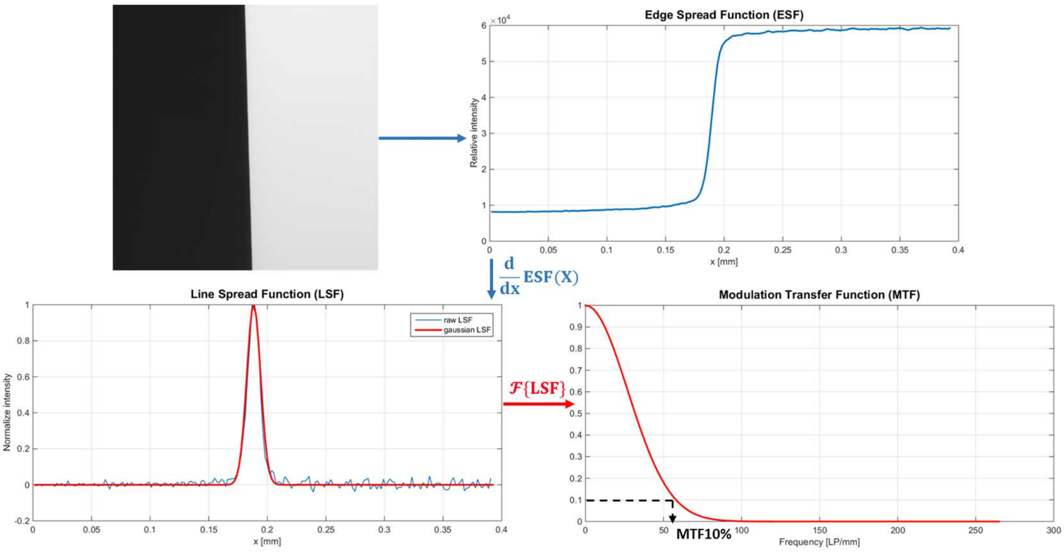

Figure 5.15: Example of radiograph of the 0.25 mm-thick tungsten cutting edge and mathematical procedure to obtain the MTF (at 10% of contrast) from the Edge Spread Function (ESF) of the acquired image.

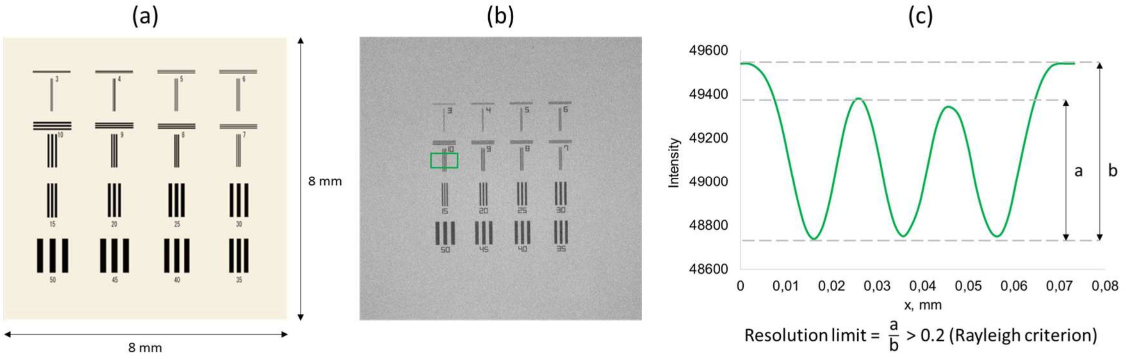

Figure 5.16: Schematic representation of JIMA chart with slit widths from 3 to 50 micrometers (a); X-ray image of the JIMA chart (b) and example of intensity profile extracted from the 10 µm-width pattern with formula for computation of the resolution limit (c).

5.2.2.3 Results

Experimental results are plotted in Figure 5.17-a, showing a good correlation between MTF10% and JIMA resolution for the different tested powers. It must be underlined that JIMA resolution values are limited to the available slit widths. As expected, the resolution degrades with the increase of radiation power. As an example, Figure 5.18 provides a visual comparison between tungsten edge and JIMA chart imaged at 2W and 20W. For both samples the worsening of resolution (higher blurring content) can be observed. Figure 5-17-b shows results of simulations: MTF10% and JIMA resolution are here plotted against the simulated focal spot size values.

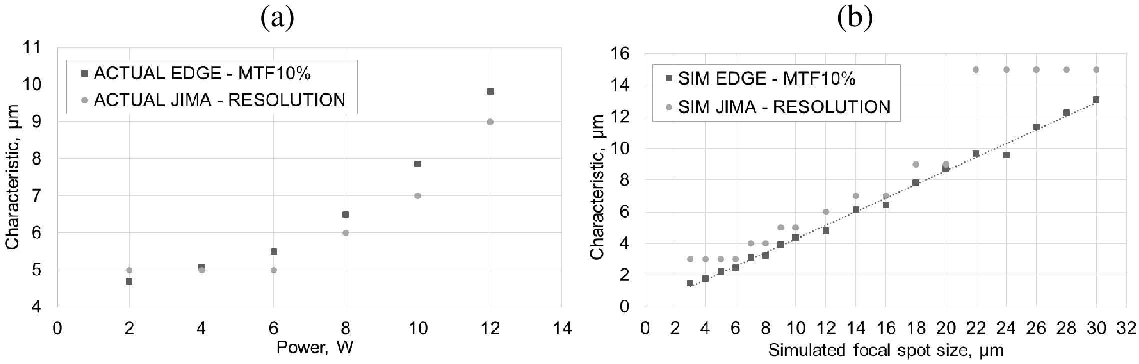

Figure 5.17: (a) MTF10% calculated from actual radiographs of a 0.25 mm-thick tungsten cutting edge and actual resolution obtained from JIMA test chart for several X-ray beam powers; (b) MTF10% and JIMA resolution obtained by simulations featuring different values of the focal spot size.

Again, the two measurements are in a good agreement. From this diagram the relation connecting the focal spot size with the MTF10% can be estimated by linear regression:

$$Focal\ spot\ size = 2.33 \cdot MTF10\% \qquad \text{(Eq. 5.5)}$$

This relation can be utilized to calculate the actual focal spot size. Results are reported in Table 5.2.

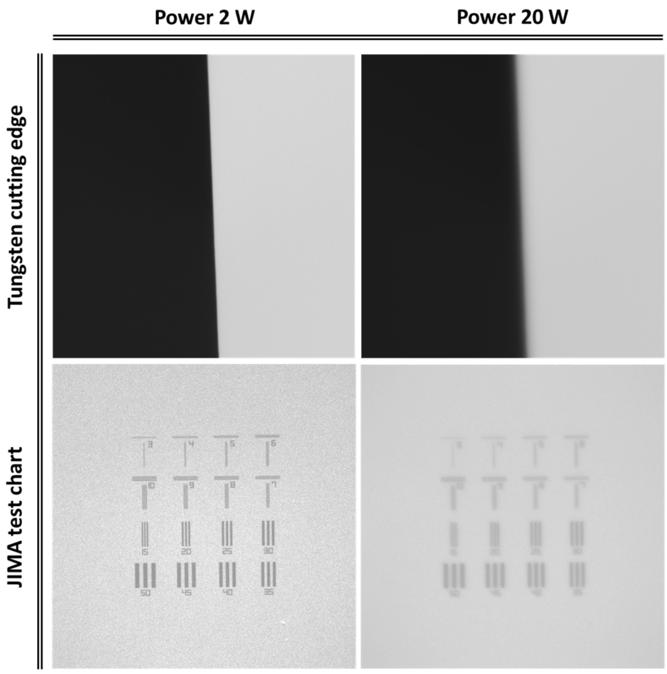

Figure 5.18: Comparison between tungsten cutting edge and JIMA chart imaged at 2W and 20W.

Table 5.2: Actual focal spot sizes calculated by means of the novel method.

Power, W	MTF10%, mm	JIMA resolution, mm	Actual focal spot, mm
2	0.0047	0.0050	0.0109
4	0.0051	0.0050	0.0118
6	0.0055	0.0050	0.0128
8	0.0065	0.0060	0.0151
10	0.0079	0.0070	0.0183
12	0.0098	0.0090	0.0228

5.2.2.3 Discussion and conclusion

A new method for evaluating the effective focal spot size of micro-focus X-ray tubes was presented. Experimental and simulation results showed that the MTF evaluated at 10% of the contrast on a 0.25mm-thick tungsten cutting edge has a good agreement with the resolution estimated by the JIMA test chart. Simulated and actual MTF values were compared and actual focal spot sizes were derived from this comparison. The focal spot size increases exponentially with the power (W). However, the computed spot sizes seem to be too large for the tested system, which has a minimum focal spot of 3 µm according to the manufacturer specifications. Further work is needed for optimizing the match between simulated and actual CT system behavior. In particular, new simulations should be conducted with addition of noise that could reasonably affect the results. More efforts should be dedicated also to optimize the alignment of test objects inside the scanning volume. In fact, even a slight misalignment with respect to the X-ray source could have a relevant influence on measurements.

5.3 Investigations on metrological structure resolution (MSR)

Metrological performance verification is fundamental for evaluating the measurement accuracy of CT systems and for ensuring the comparability with other measuring systems. For this purposes, several acceptance and reverification tests have to be performed periodically, as described in Section 3.1.1. An important characteristic to be assessed is the metrological structural resolution (MSR), defined by the German guideline VDI/VDE 2617-13 [33] as the size of the smallest structure that can still be measured within error limits to be specified. The MSR provides relevant additional information with respect to length measurement errors and probing errors of size and form. For example, increasing low-pass filters can result in improved probing error and – at the same time – worsened MSR. The statement of the MSR is of great importance, especially when measuring small geometries or microstructures [65]. Differently from other concepts of resolution, such as geometrical unsharpness [62] and modulation transfer function (MTF) (see e.g. ASTM E1695 [88] or EN 16016-3 [71]), the metrological structural resolution encompasses the whole CT measurement chain, ranging from acquisition of X-ray images till final metrological software elaborations. At present, a number of methods have been proposed for MSR evaluation. However, a standard procedure to be included in the CT part of the ISO 10360 has still to be defined [89].

This section is aimed at: (i) reviewing the state of the art in MSR evaluation, (ii) introducing the principle and the advantages of the 'Hourglass' method for evaluating the MSR of industrial CT systems, (iii) studying its relation with other proposed methods and (iv) quantifying the main influence factors that can affect the method. Finally, results from a MSR verification conducted on the MCT225 system are reported and discussed.

5.3.1 Overview of the state of the art in MSR evaluation

The main proposed methods for evaluating the MSR are briefly described in the following:

i. VDI/VDE 2617-13 [33] proposes to determine the MSR from the diameter of the smallest sphere that can still be measured within a certain error which should be specified by the manufacturer (Figure 5.19). Spheres should be scanned with the same parameters required for the actual measurement. Diameters are computed after least squares fitting of spheres.

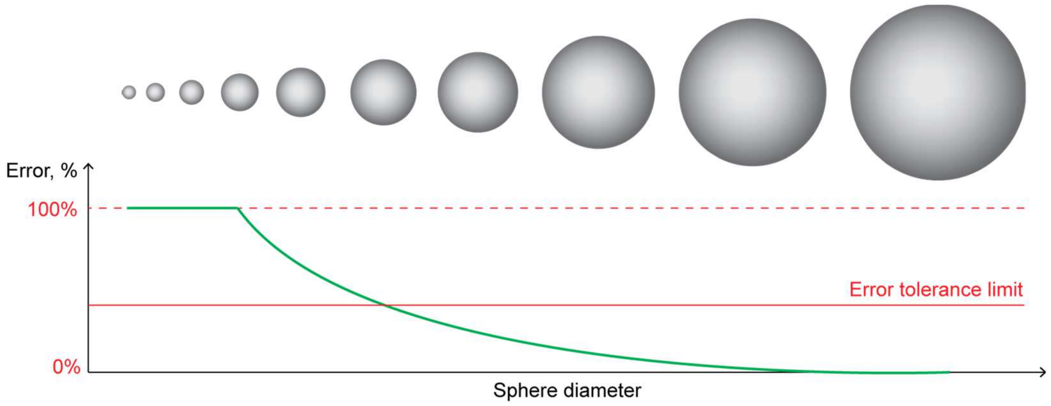

Figure 5.19: VDI/VDE 2630-1.3 proposed test procedure.

ii. Measurement of groups of equidistant line-patterns in vertical and horizontal direction and circular dots. For example, the MicroCT Bar Pattern Phantom manufactured by QRM GmbH [90] is conceived to assess in-plane and axial spatial resolution of CT systems in a direct visible manner, but it can be used to consider the whole dimensional measurement chain as well (Figure 5.20-a). In fact, distances between lines and dots diameters can be computed after the surface determination step. However, in this case, the measurement implementation is not easy, especially for lines and dots with size close to the resolution limit (Figure 5.20-b).

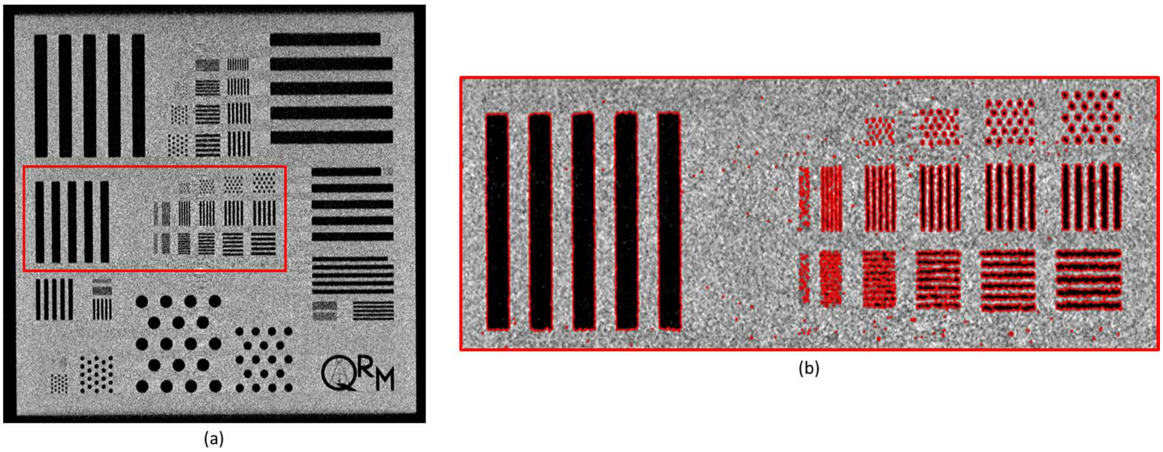

(a)

(b)

Figure 5.20: Reconstructed slice of the QRM MicroCT Bar Pattern Phantom (a) and determined surface (b) (from measurements performed by the author).

iii. Determination of the MSR of a CT system by measuring the edge radius of specimens featuring sharp edges [65] (Figure 5.21). The edge area has to be segmented in equally-spaced sections and then a Gaussian circle has to be fitted to each section. Reference measurements of the edge are required and were obtained by Bartscher et al. [65] using an optical measuring system with focus variation principle.

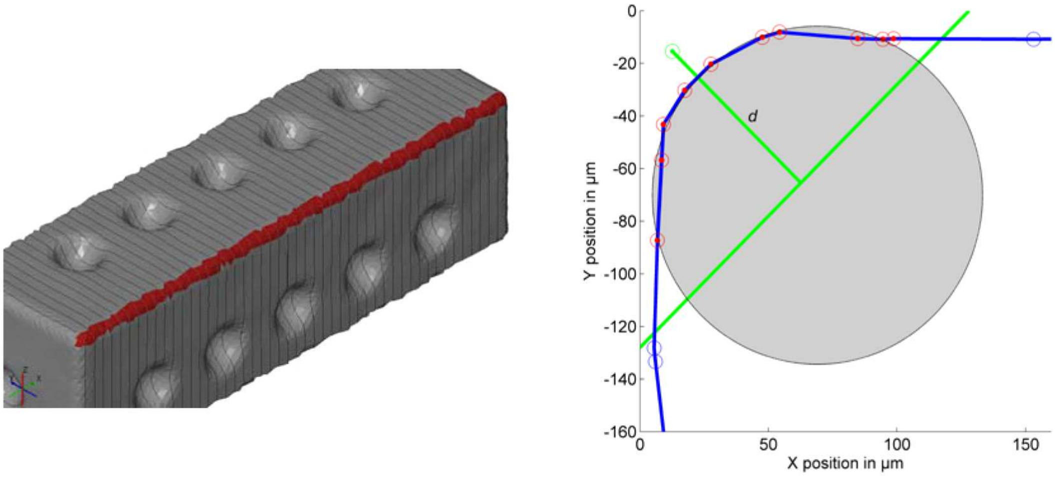

Figure 5.21: Calotte cube edge analyzed using parallel intersection cuts (left). The area chosen for circle fitting is shown in red. Detail of a sample section of one edge end respective fit of a circle (right). [65]

iv. Measurement of the radius of curvature on a calibrated round edge structure [91]. From the deviation between the measured and the calibrated radius, an analogue Gaussian broadening of the measurement system is determined. For this purpose, a reference standard was manufactured by PTB characterized by a cylindrical body incorporating three grooves and three flanges (Figure 5.22). AFM measurements were conducted to get reference values for the radius of curvature.

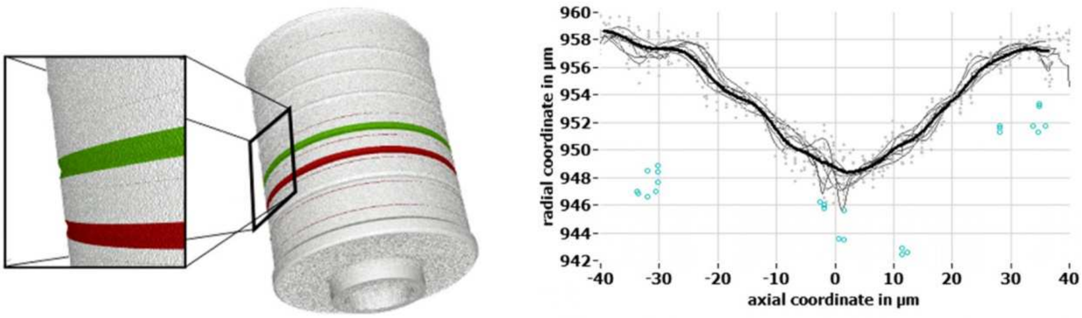

Figure 5.22: Reference sample incorporating grooves and flanges enabling the measurement of MSR (left). Extracted surface points in cylinder coordinates (right). [91]

v. Analysis of the frequency response of a CT system when measuring the surface of an Aperiodic Spatial Frequency Standard [92]. Acquired data points are extracted along circumferential lines (similar to what is usually done in roundness measurements) and a Fourier analysis carried out. The obtained amplitudes of different spatial frequencies have to be compared with a reference measurement so the frequency response of the CT system can be determined. The resulting characteristic curves of transmission resemble the MTF used to determine the spatial resolution of CT systems.

vi. Frequency response analysis applied on the sinusoidal surface of a multi-wave standard [93, 94]. Similarly to the method v. [92], circumferential lines are extracted from a CT reconstruction of the multi-wave standard and a frequency response analysis is conducted to obtain the relative transmission values that have to be fitted with a frequency domain generalized Gaussian function. The MSR is defined as the cut-off wavelength value at an amplitude transmission value of 50%.

5.3.2 Selected approach for MSR evaluation: the ‘Hourglass’ standard

The ‘Hourglass’ standard – developed at the University of Padova and already introduced in [95] – allows testing the CT metrological structural resolution by using a simple geometry consisting of two touching spheres with the same nominal diameter (D). A schematic representation of the object is shown in Figure 5.23-a. The CT reconstructed volume appears to be distorted in proximity of the contact point (Figure 5.23-b). The dimensions (d and h) of the distorted contact zone decrease as the metrological structural resolution improves (Figure 5.23-c).

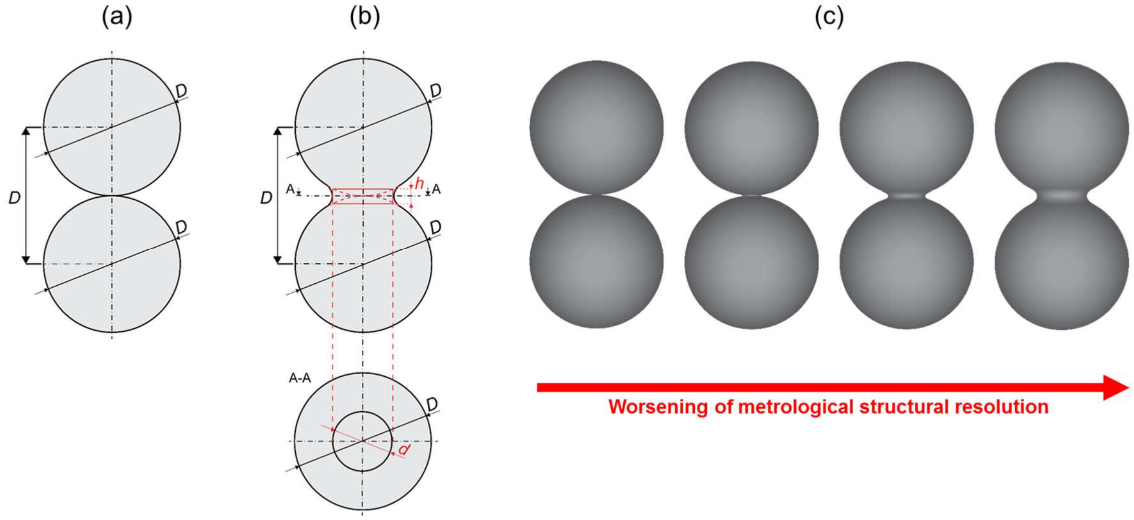

Figure 5.23: Concept of the 'Hourglass' standard. (a) Nominal geometry of the 'Hourglass' standard, which consists of two solid spheres of equal diameter D. (b) Distorted geometry of the surface reconstruction resulting from CT measurement of the 'Hourglass' standard, where the actual diameter d and height h of the contact zone depend on the metrological structure resolution. (c) As the metrological structure resolution decreases (left to right), the dimensions of the contact zone increase.

The diameter d can be calculated by fitting a Gaussian circle in the plane containing the touching point, while the height h can be derived from the following equation:

$$h = D - \sqrt{D^2 - d^2} \qquad \text{(Eq. 5.6)}$$

Since CT allows measuring inner surfaces and interfaces, measuring h can be useful to assess the minimal detectable distance of which two converging surfaces can be distinguished. Thus, h can be considered as the last measurable dimension and corresponds to a sort of limit of measurability. In this research work, the 'Hourglass' method was improved by definition of a more complete measurement procedure, made possible by the high number of available measurable dimensions (heights and diameters) ideally going down till infinitesimal values, as visible in Figure 5.24-a. Several vertical distances can be computed and measurement errors quantified for each of them (Figure 5.24-b). In this way, the metrological structural resolution can be defined, similarly to the VDI/VDE 2617-13 [33] definition, as the smallest dimension that can still be measured within a specified error. In this case, distances are computed instead of sphere diameters. The reconstructed 'Hourglass' standard has to be firstly aligned to the coordinate system where the vertical axis corresponds to the line traversing the spheres centers and the origin is set in correspondence of the contact point. A number of circles are then fitted (orthogonally to the line connecting the spheres centers) above and under the central plane with constant step-size and their radii are measured. The height which should correspond to the measured radii (i.e. reference height) can be derived using equation (1) and differ from the actual height when the structural resolution degrades.

This 'Hourglass' method provides several important advantages with respect to the other proposed methods:

- Simple design allowing simple and cheap construction and calibration.
- Fast measurement procedure.
- Presence of very small measurable dimensions (heights and diameters) ideally going down till infinitesimal values, as visible in Figure 5.24-a.
- The MSR can be measured directly in the unit of length (meter).
- Simple and direct verification that increasing low-pass filters can improve probing errors (assessed on the two touching spheres), while the MSR is worsened (see example in Figure 5.25).

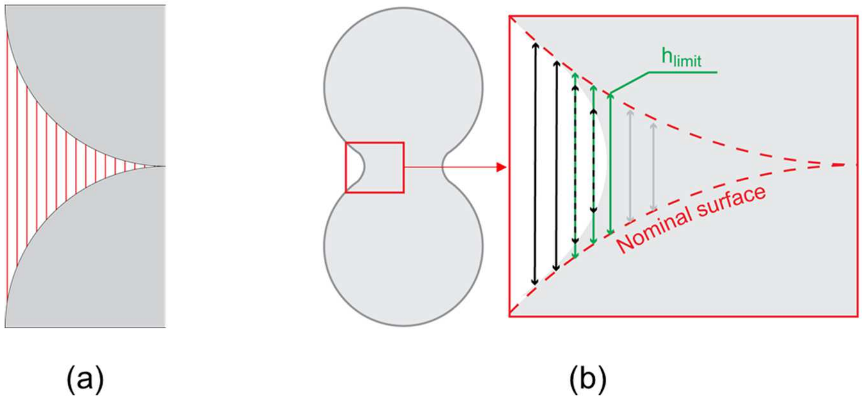

Figure 5.24: (a) Measurable dimensions (heights) ideally available till infinitesimal values. (b) Example of multiple measured heights. Measurement errors can be obtained by comparison of measured heights (black arrows) with nominal heights (green arrows). Grey arrows are heights that can't be measured.

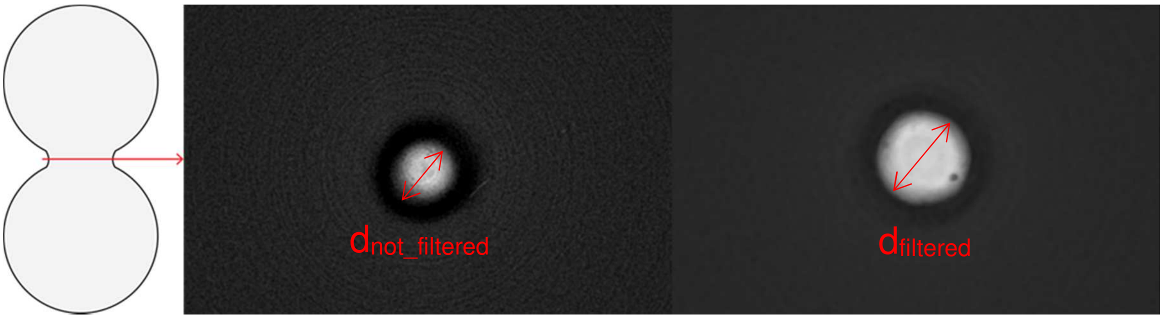

Figure 5.25: Effect of the application of a median filter on the middle 2D section of the distorted contact region: the diameter d increases proving the worsening of MSR, while probing errors measured on the two spheres improve.

In this work, six precision spheres with nominal diameter equal to 8 mm were used to produce three 'Hourglass' standards to be used for the experimental tests. Each 'Hourglass' standard was made by a different material: alumina, ruby and borosilicate glass. Spheres diameters have been calibrated and form errors evaluated by tactile coordinate measuring machine (Zeiss Prismo 7 Vast) with calibration uncertainty equal to 0.0015 mm (see Figure 5.26).

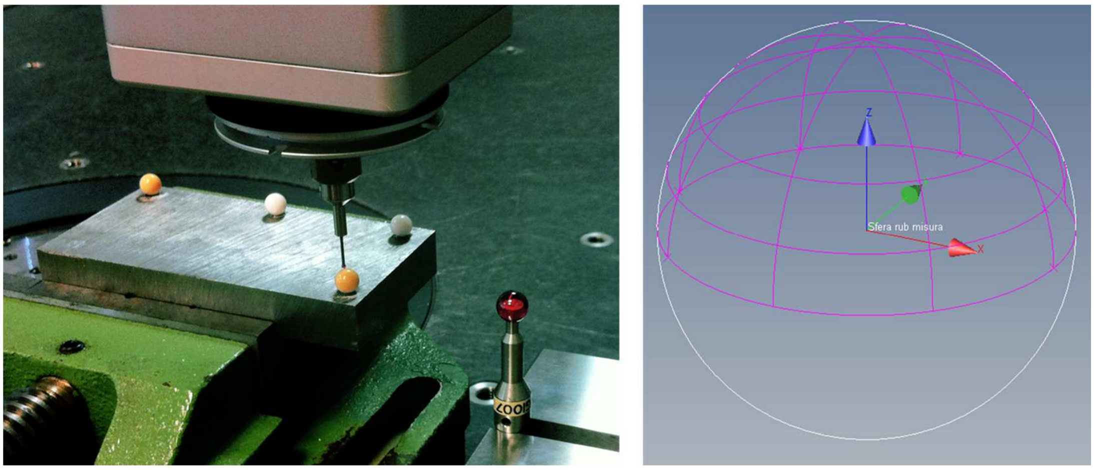

Figure 5.26: Calibration of an alumina sphere by tactile CMM (left). The calibrated ruby sphere was used as reference object to correct systematic errors and to determine the calibration uncertainty. The CMM measurement strategy (right) consisted in points probed in continuous mode on 7 half-circle paths.

5.3.3 Comparison of methods

Hourglass *vs.* VDI/VDE 2617-13

The guideline VDI/VDE 2617-13 [33] defines the MSR as the diameter of the smallest sphere that can still be measured within a certain specified error (method i. Section 5.1). The practical implementation of this method is not as simple as its concept. In fact, for CT systems with micrometric resolutions, spheres with diameter of few micrometers are required but they are difficult to be manufactured with acceptable form errors and are also problematic for calibration.

Simulations of CT bi-dimensional section of spheres were conducted using Matlab in order to evaluate the limit of measurability connected only to the voxel size. Three different coordinates of circles' centers inside the pixel grid were considered, as visible in Figure 5.27. The influence of the center position as well as the measurement errors become particularly relevant for very small pores (diameter ≤ 2 voxels). Moreover, simulated CT scans (3D) of spheres were performed using Scorpius XLab, showing that spheres with diameter equal or lower than 2 voxels are not measurable.

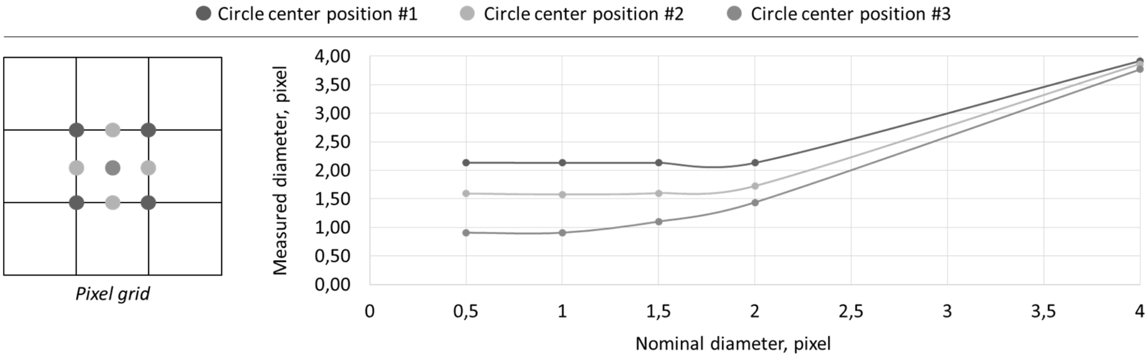

Figure 5.27: Results of 2D simulations of circles with different coordinated of the center inside the pixel grid.

To compare the spheres method with the 'Hourglass' method, 5 μ-spheres made by ruby with diameters equal to 0.2, 0.4, 0.6, 0.8 and 1 mm were CT scanned together with the ruby 'Hourglass' standard. Three magnifications were selected in order to consider different *sphere diameter/voxel size* ratios, as shown in Table 5.3.

Table 5.3 – Relation between diameter of spheres and voxel sizes considered in the experimental tests.

	Sphere diameter/voxel size		
Sphere diameter, mm	Voxel size = 0.05 mm	Voxel size = 0.10 mm	Voxel size = 0.20 mm
0.2	4	2	1
0.4	8	4	2
0.6	12	6	3
0.8	16	8	4
1	20	10	5

Actual scans confirmed that spheres with diameter below 2 voxels are not measurable. Furthermore, percentage measurement errors are higher than 35% for spheres diameter equal to 2 voxels and around 10% for diameters ranged between 3 and 6 voxels (see Figure 5.28). Since ruby is not a material with a high X-rays absorption, the contrast to noise ratio could be not sufficient to discriminate between noise and spheres when the diameter is, for example, equal to 1 voxel. For this reason, a 0.1 mm steel sphere was manufactured by means of micro-EDM technology and CT scanned with voxel size 0.1 mm (*sphere diameter/voxel size* = 1). The sphere was actually detectable, but the measured diameter was more than twice the nominal diameter. On one side, the diagram reported in Figure 5.27 already proved that very high errors can be expected for sphere/circle diameters equal and below 1 voxel. On the other side, steel spheres are affected by scattering and beam hardening. These tests confirm the difficult practical application of the VDI/VDE 2617-13 method.

Figure 5.28 compares the percentage errors obtained by measuring the ruby spheres diameters and the multiple vertical distances on the ruby ‘Hourglass’ standard (see procedure in Figure 5.24). The two methods do not seem to be in good agreement, especially for very small dimensions. For example, the ‘Hourglass’ standard allowed measuring also distances equal to 1 voxel. A similar result was obtained by means of simulated CT scans.

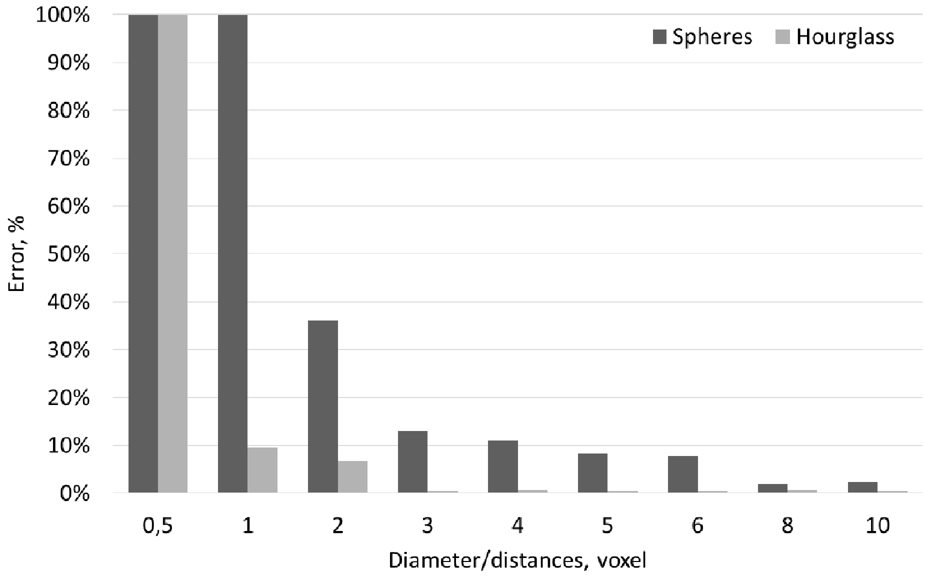

Figure 5.28: Comparison between errors obtained with the spheres method (VDI/VDE 2617-3) and the ‘Hourglass’ method. Spheres diameters and distances measured on the ‘Hourglass’ are expressed in voxels (i.e. number of voxels).

Hourglass *vs.* Edge-based method

In the edge-based method [65] (method iii., Section 5.1) the MSR is evaluated through the radius r fitted to the cutting edge border, while in the 'Hourglass' method through the height h of the cylindrical distorted zone. An equivalent height h can be defined in the former method, as well as an equivalent radius r can be defined in the second one, as shown in Figure 5.29. The two formulas in Figure 5.29 are equal when the following equation is satisfied:

$$\frac{4Rh - h^2}{4(2R - \sqrt{4Rh - h^2})} = \frac{h}{2}\left(\frac{\cos\alpha}{1 - \sin\alpha}\right) \qquad \text{(Eq. 5.7)}$$

where R is the radius of the 'Hourglass' spheres, h is the measured height of the distorted contact region and α half angle of the sharp edge.

At first, this equation was applied in the simplified 2D case represented in Figure 5.30. A simulated CT scan (using Scorpius XLab) of a 'Hourglass' standard with 8 mm spheres and a cone with angle α calculated by (Eq. 5.7) was performed for further validation of the relation (see Figure 5.31). The cone was selected as a simple geometry to approximate a sharp-edge object. It can be observed that the resulting heights are in both cases equal to the voxel size.

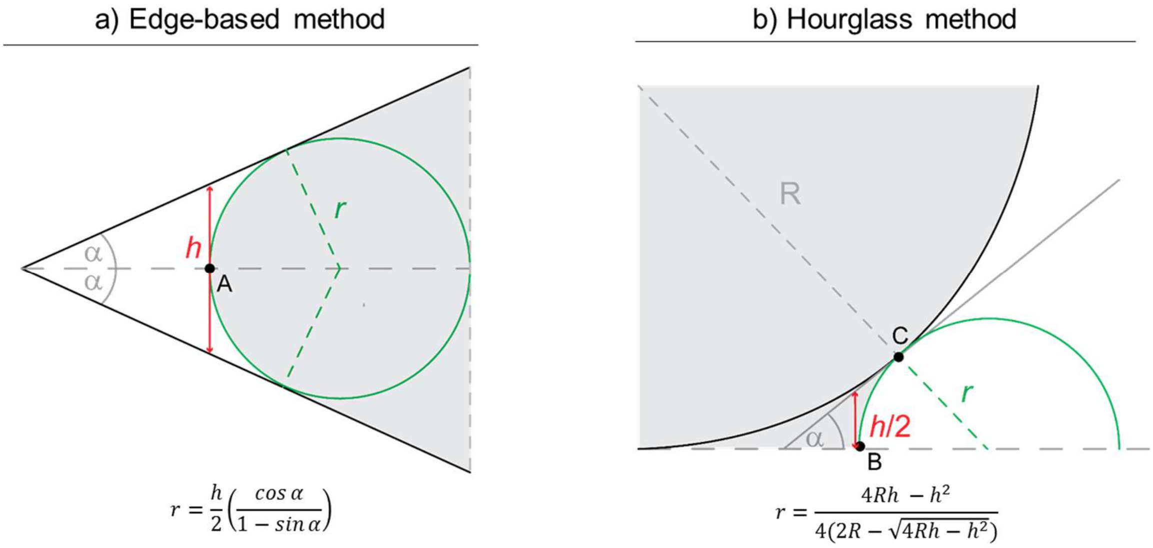
a) Edge-based method

$$r = \frac{h}{2}\left(\frac{\cos\alpha}{1 - \sin\alpha}\right)$$

b) Hourglass method

$$r = \frac{4Rh - h^2}{4(2R - \sqrt{4Rh - h^2})}$$

Figure 5.29: Edge-based method concept (a) where r is the radius of the circle fitted to the actual edge and h the equivalent height passing through the point A. Hourglass method concept (b) where h is the height of the actual distorted region and r the radius of the circle passing through B (intersection of h with the horizontal dashed line departing from the spheres touching point) and C (tangent point). Grey regions are those obtained by CT reconstruction in both methods. Black full lines represent the nominal geometries.

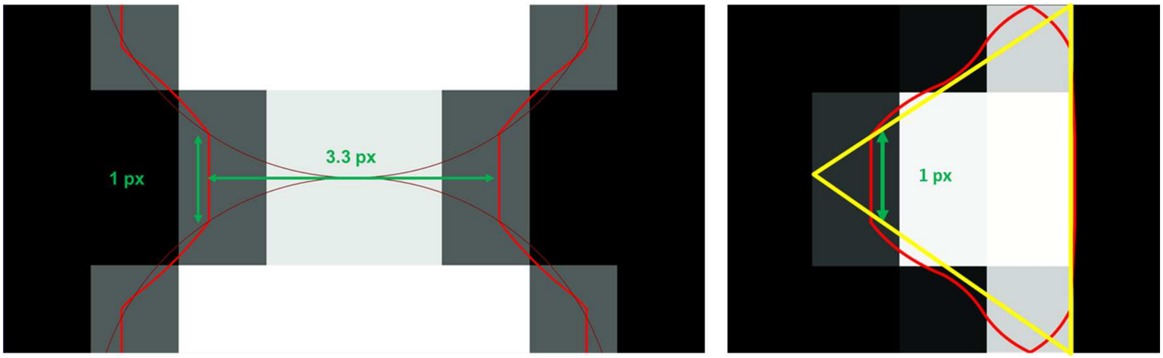

Figure 5.30: 2D simulation of 'Hourglass' standard (left) and cutting edge (right). The 'Hourglass' spheres diameter is equal to 6 pixels and the measured height (h) 1 pixel. The cutting edge angle is 76°, as calculated from equation (Eq. 5.7). The resulting height is equal to 1 pixel also in this case.

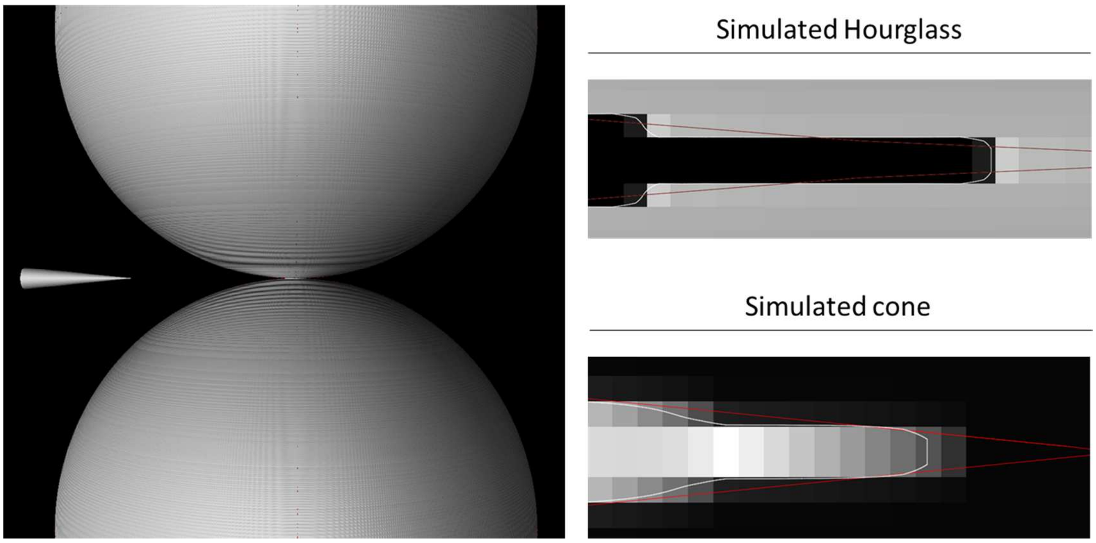

Figure 5.31: 3D reconstruction of simulated 'Hourglass' standard and cone (left). Zoomed 2D sections showing the resolution effect on both Hourglass and cone (right): the heights are in both cases equal to the voxel size.

Hourglass *vs.* PTB reference standard

The PTB method concerning the measurement of curvature radius on a calibrated round edge structure (method iv. Section 5.1 [91]) is based on the principle of the *curvature transfer function* (Figure 5.32), for which there is a one-to-one relation between the actual curvature radius and the measured curvature radius down to the resolution limit. In this limit regime the measured curvature is increased. The authors assumed that the cause is a Gaussian broadening that can be determined from the ratio between the measured and the calibrated radius of a reference standard with a circular rounded edge.

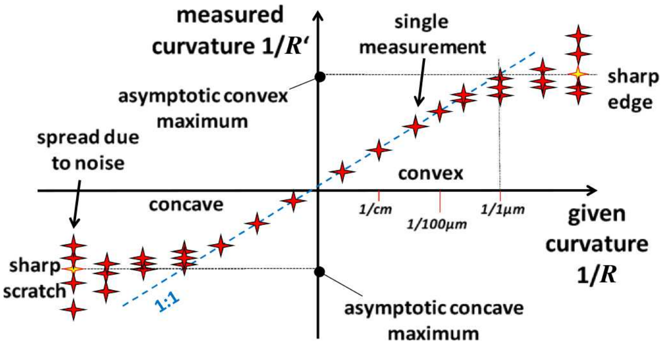

Figure 5.32: Principle sketch of the curvature transfer function between the actual curvature and the measured curvature [91].

The concept of *curvature transfer function* applies well also to the 'Hourglass' method, as illustrated in Figure 5.33-a. In this case, instead of a calibrated radius of a circular rounded edge, the limit measurable dimension is zero in correspondence to the spheres touching point. Figure 5.33-b shows that curves extracted from a CT reconstructed 'Hourglass' standard are very similar to those obtained with the PTB reference standard (Figure 5.22-right).

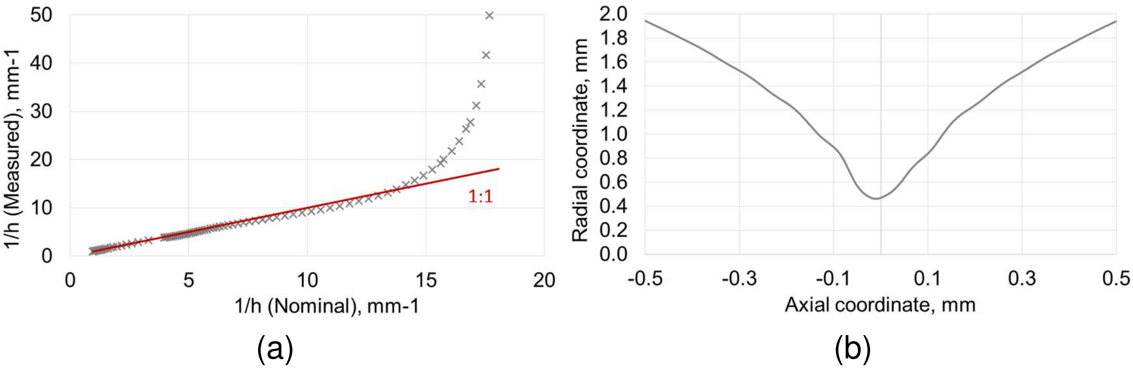

Figure 5.33: Concept of the "Curvature transfer function" applied to the 'Hourglass' standard between the actual and measured height h (a) and surface points extracted from the CT reconstructed 'Hourglass' standard in radial coordinates (b).

Finally, methods based on the frequency response analysis [92, 93] lead to results of a different nature with respect to the 'Hourglass' standard. The obtained results can be considered as a sort of MTF applied to the entire CT dimensional measurement chain. However, differently from the 'Hourglass' method, this kind of MSR statement is not in the unit of length (meter).

5.3.4 Factors influencing the 'Hourglass' method

Influence factors that could affect the 'Hourglass' method implementation should be distinguished from factors influencing the structural resolution regardless of the used method. In this Section, the attention is focused on the factors of the first type, which can be connected to the sample design (e.g. Hertzian contact between spheres, spheres material and dimensions), to the presence of CT particular effects (e.g. Feldkamp effect, ring artifact and partial volume effect) and to the measurement strategy (e.g. sample orientation, thresholding procedure, scanning parameters, etc.).

In the following, some of these influence factors are described and quantified by experimental and/or simulation analyses.

Hertzian contact between spheres

The Hertzian theory of elastic deformation [96] allows evaluating the dimension of the circular contact area existing in practice between two spheres, and depending from elastic deformation properties of materials (Figure 5.34). In particular, the radius of the circular contact area can be evaluated by the equation reported in Figure 5.34.

The force F was approximated to the weight exerted by the top spheres on the bottom one: i.e. $8.7 \cdot 10^{-3}$ N. Finally, using the Young modulus (E) and the Poisson coefficient (ν) of alumina (which are respectively 60 GPa and 0.2) the radius a was found to be equal to $1.4 \cdot 10^{-4}$ µm. Hence the influence of the Hertzian contact area can be neglected in this case.

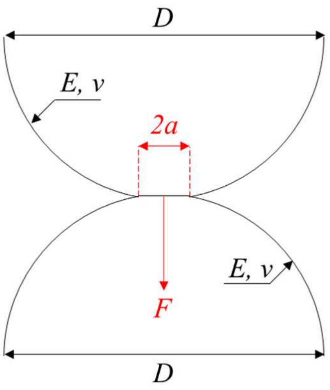

$$a = \sqrt[3]{\frac{3}{8} FD \frac{(1-\nu^2)}{E}}$$

Figure 5.34: Hertzian contact between spheres: *F* is the force generated by the top sphere weight, *D* is the spheres diameter, *E* the Young modulus, *v* the Poisson coefficient and *a* the radius of the contact circle.

Spheres material

As stated by the VDI/VDE 2617-13 [33], "the manufacturer specifies the material for testing the size probing error P_S and form probing error P_F. Testing the structural resolution for dimensional measurements must be performed with a sphere made from the same material." This implies that material has to be considered as an important factor when evaluating the MSR.

An experimental test was performed by CT scanning three 'Hourglass' standards made of different materials: glass, ruby and alumina in one single acquisition with voxel size equal to 0.1 mm. As illustrated in Figure 5.35, a correlation between the measured heights and the material density was found. Further tests are needed to consider, for example, different magnifications and multiple repetitions.

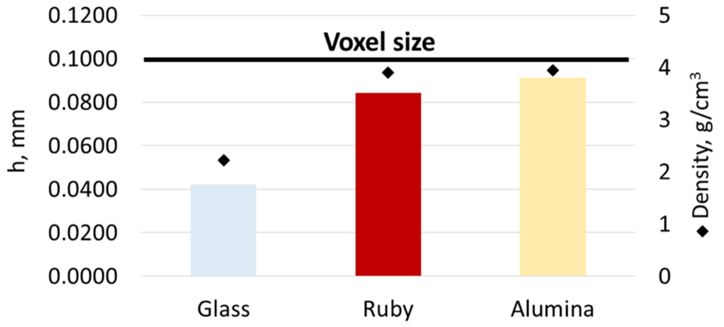

Figure 5.35: Metrological structural resolution evaluated on three Hourglass standards made by glass, ruby and alumina. Material densities are plotted as rhomboidal points.

Spheres dimensions

The influence of spheres diameter was assessed by three simulations performed using the commercial software Scorpius XLab, with fixed scanning parameters, constant voxel size of 9.5 um and three different spheres diameters: 8 mm, 4 mm and 1 mm. As illustrated in Figure 5.36, the dimension d of the distorted contact zone decreases as the spheres diameters decrease, while the measured height h resulted to be always the same. Therefore, spheres diameter is not influencing the MSR results, provided that MSR is evaluated by measuring heights (not diameters) of the distorted contact zone.

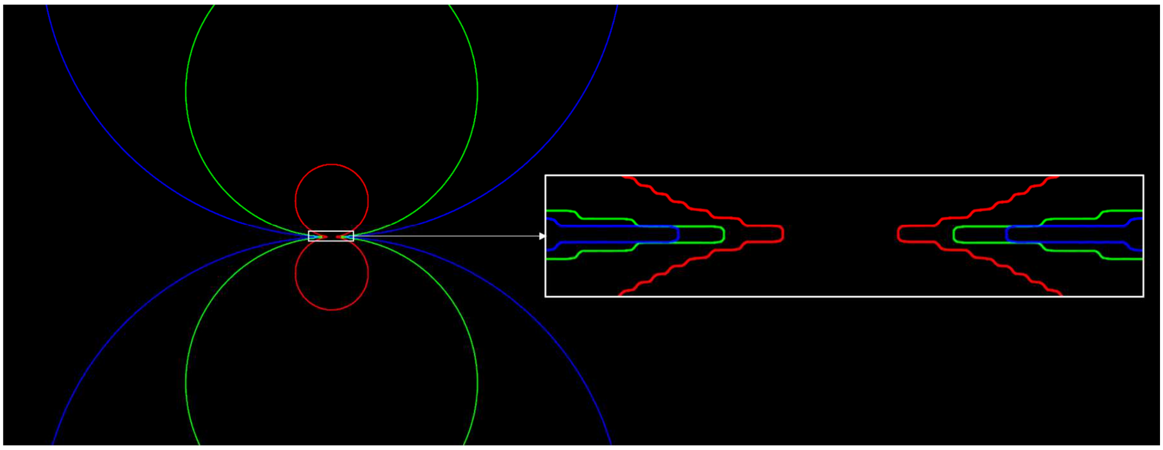

Figure 5.36: Determined surfaces of three simulated 'Hourglass' standards characterized by different spheres diameters and scanned at the same magnification. The height of the distorted contact region remains the same.

Feldkamp effect

When using a cone beam CT system, the Feldkamp algorithm [19] is normally applied for three-dimensional volume reconstruction and can lead to the so-called Feldkamp effect (see Section 3.3). The resulting artefact affects the quality of measurements for those regions of the workpiece which are scanned near to the detector borders. Before assembling the 'Hourglass' standard, the bottom sphere was CT scanned alone for quantifying the influence of Feldkamp effect on the contact zone. In Figure 5.37, the Feldkamp artifact is visible only on the lower part of the sphere, corresponding to the lower border of the detector. The Feldkamp effect can be considered negligible in the contact region provided that the contact region is positioned in correspondence of the detector center line.

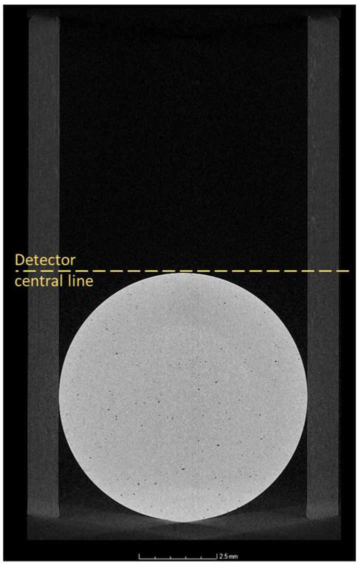

Figure 5.37: 2D section of one sphere of the 'Hourglass' standard scanned alone under the detector central line. The Feldkamp effect is visible only on the bottom side.

Beam hardening

Beam hardening (described in Section 3.3) is a phenomenon that leads to an image artifact typical of CT systems emitting a polychromatic radiation. To evaluate the sensitivity of the 'Hourglass' method to the beam hardening, 27 CT scans were performed with different parameter settings (but constant voxel size equal to 9.5 µm) and were all reconstructed three times, applying three different beam hardening corrections. These corrections were obtained using a linearization technique based on polynomial curves of maximum fourth order (implemented in the software used for reconstruction: CT Pro 3D):

$$Y = a(b + cX + dX^2 + eX^3 + fX^4) \qquad \text{(Eq. 5.8)}$$

where X represents the initial grey value of a pixel in an X-ray image, Y represents the corrected (linearized) grey value, and a through f represent coefficients that can be fine-tuned in order to obtain reduction of the beam hardening effect on images.

Coefficients of the three applied polynomial curves are listed in Table 5.4.

Table 5.4: Coefficients used in Eq. 5.8 for the three applied beam hardening corrections.

Coefficients	BHC1	BHC2	BHC3
a	1	1	1
b	0	0	0
c	1	0.75	0.5
d	0	0.25	0.5
e	0	0	0
f	0	0	0

As it can be observed in Figure 5.38-a, correcting the beam hardening leads the MSR (represented here by the height h) to decrease for the majority of scans. A mean reduction of 0.5 µm can be observed between each correction (Figure 5.38-b). These results suggest that the beam hardening influences the MSR measurement conducted by the 'Hourglass' method.

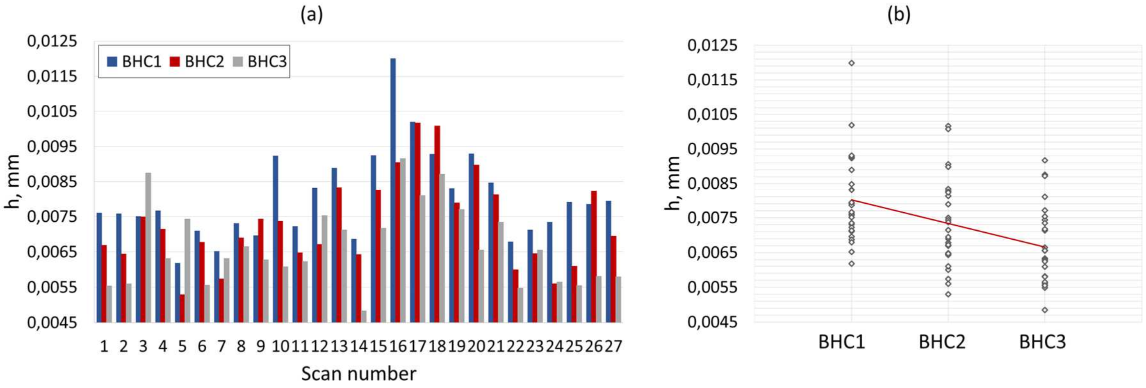

Figure 5.38: Beam hardening effect on MSR (here height, h) evaluated on 27 scans (voxel size 9.5 µm) of an alumina 'Houglass' standard (a) and average values (red line) confirming that beam hardening correction can improve the MSR (b).

Object orientation

Another factor that can influence the 'Hourglass' method is the orientation of the object. Two possible orientations are *vertical* (when the line connecting the spheres centers is parallel to the rotation axis) and *horizontal* (when the line connecting the spheres centers is perpendicular to the rotary axis). They are schematized in Figure 5.39.

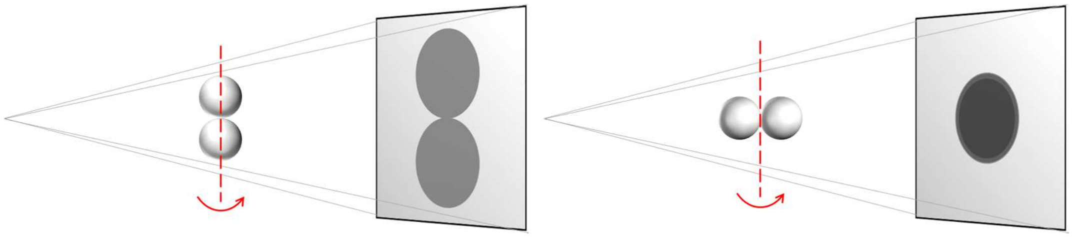

Figure 5.39: Vertical (right) and horizontal (left) orientation of the 'Hourglass' standard during CT acquisition.

In the first case, the length of the material to be traversed by the radiation is constant during the whole CT scan, whereas in the second case, it varies during the acquisition up to *2D* (*D* = spheres diameter). Since the horizontal orientation is more affected by noise and artifacts, results obtained with different orientations can be difficult to compare. To evaluate the influence of object orientation, these two orientations (horizontal and vertical) were tested. A higher voltage (i.e. 210 kV) had to be used with respect to the voltage used for the other tests (see Table 5.6 in Section 5.3.5), in order to achieve an acceptable penetration for both the orientations. Maximum differences of 2 µm were found between the two orientations, for both *h* and $\mathrm{MSR}_{20\%}$. In addition, simulations were performed with an ideal X-ray beam emitted by a single point and in absence of noise.

Figure 5.40 compares the contact sections obtained with both experimental and simulated scans, showing that similar dimensions were achieved by simulated and actual scans but with different aspects. Further work is needed to better quantify and understand this influence.

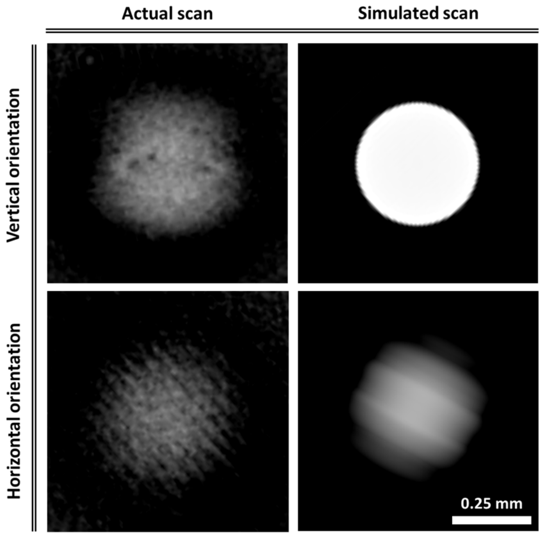

Figure 5.40: Visual comparison between contact sections obtained by actual and simulated scans considering two orientations of the ‘Hourglass’ standard: horizontal and vertical.

Partial volume effect

After performing the 3D reconstruction of the ‘Hourglass’ standard, the contact point between spheres can lie in different positions inside the reconstructed voxel matrix, as shown in Figure 5.41.

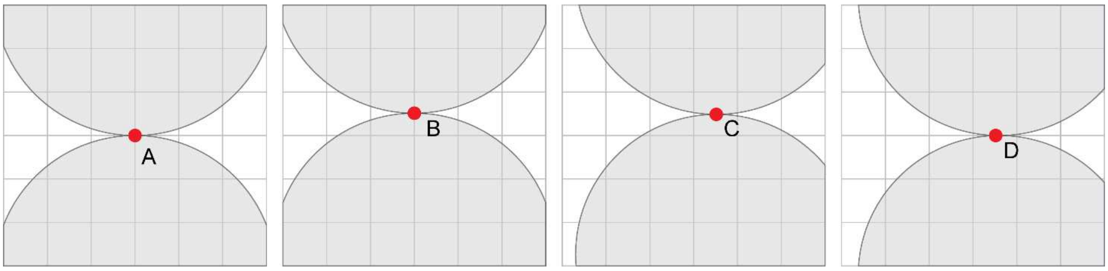

Figure 5.41: Four examples of spheres touching point coordinates inside the detector pixel grid.

Depending on these positions, the partial volume effect [12] can produce different results (see Figure 5.42). Consequently, the evaluated surface as well as the calculated *h* can vary as demonstrated by the simplified 2D example illustrated in Figure 5.42. CT simulations performed with Scorpius XLab confirmed this observation on an alumina ‘Hourglass’ standard with spheres diameter equal to 8 mm. In particular, one simulation was performed with the contact point corresponding exactly to the detector central point for all the acquired projections and another with contact point positioned half voxel above the detector central point. The resulting *h/voxel size* ratio varied between 0.4 and 1.

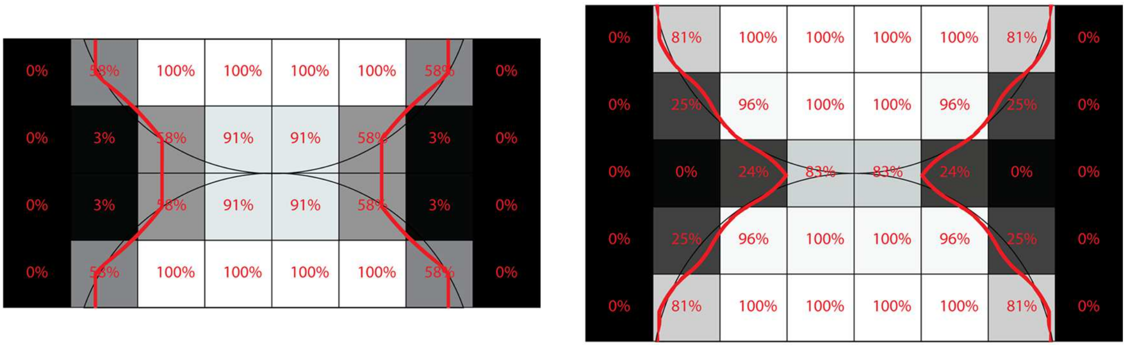

Figure 5.42: Example of two possible positions of the 'Hourglass' standard inside the detector pixel grid with resulting determined surface (in red), leading to different dimensions of the distorted contact region. Percentages refers to gray values of pixels where 0% stays for air and 100% for material.

Thresholding process

The influence of the surface determination procedure (explained in Section 2.3) on the 'Hourglass' method is here addressed by following an approach inspired by [23]. For two touching spheres, the threshold can be considered optimal when the sum of measured spheres radii $(r_1 + r_2)$ is equal to the measured center-to-center distance (SD). Figure 5.43 shows this concept, defining the threshold calibration error Δ as:

$$\Delta = r_1 + r_2 - SD \qquad \text{(Eq. 5.9)}$$

A CT scan of the alumina 'Hourglass' standard was performed with voxel size 7.4 µm. The starting threshold value was changed progressively. This procedure was applied using both global and advanced (local) surface determination. Diagrams reported in Figure 5.44 summarize the obtained results. It can be observed that the global method has a bigger influence on measurements of sphere radii with respect to the local method, while center-to-center distances seem to be less affected by the surface determination procedure. The resulting Δ is constant for the local method, while it follows a descendent trend for the global one.

As far as the MSR (here measured in terms of height *h*) is concerned, its trend shows a similar slope for the two tested surface determination modes, proving that the MSR evaluated by means of the 'Hourglass' method is in general affected by the thresholding procedure. Moreover, a systematic reduction of about 2 μm was achieved with the advanced/local surface determination with respect to the global method.

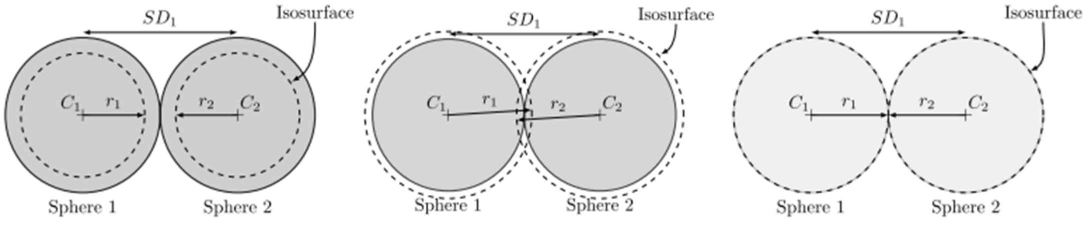

(*a*) (*b*) (*c*)

Figure 5.43: Influence of threshold value on threshold calibration error Δ. C_i sphere centre, r_i sphere radius determined from threshold value and SD_i distance between sphere centres. (a) $\Delta = r_1 + r_2 - SD_1 < 0$, (b) $\Delta = r_1 + r_2 - SD_1 > 0$, (c) $\Delta = r_1 + r_2 - SD_1 = 0$ [23].

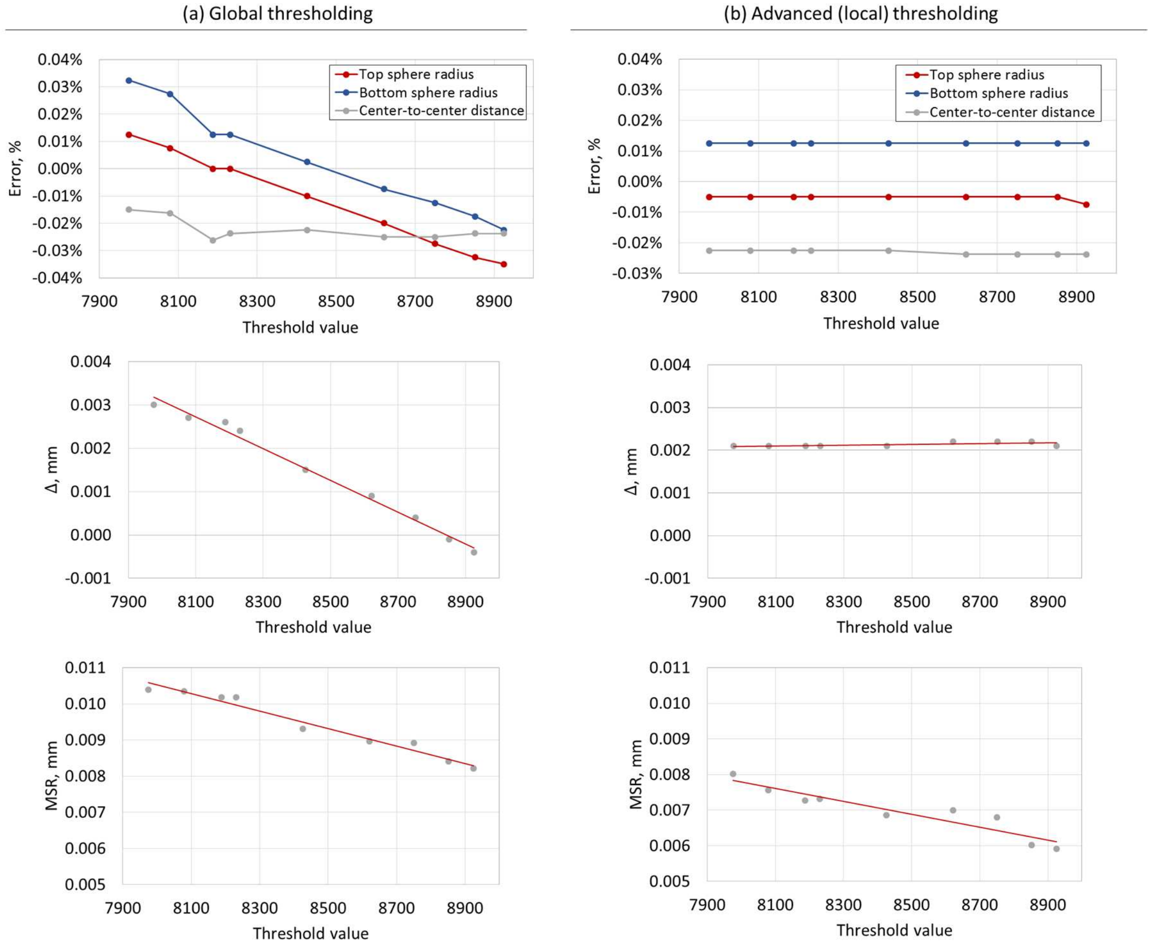
(a) Global thresholding

(b) Advanced (local) thresholding

Figure 5.44: Effect of threshold value selection on percentage measurement errors of sphere radius and spheres center-to-center distances, threshold calibration error Δ and MSR for both global thresholding (a) and advanced/local thresholding (b).

Scanning parameters

Following an experimental design, 27 CT scans of the alumina 'Hourglass' standard were performed with fixed magnification (voxel size equal to 9.5 µm). Three scanning parameters (voltage, current, number of projections) were varied, as shown in Table 5.5. The step-size variation was chosen in order to trigger distinguishable process responses, so some settings cannot be considered optimal. However, parameters were chosen in order to avoid saturation (too bright images) or not-complete penetration of the object (too dim images). The response factor is the metrological structural resolution (MSR), evaluated in this case by the height h of the distorted contact region of the reconstructed 'Hourglass' standard. A repeatability test was conducted during the same day with additional 5 repeated scans (fixed parameters). The resulting standard deviation was 0.2 µm.

Table 5.5. CT scanning parameters variation for the 'Hourglass' method.

CT scanning parameter	*low*	*center*	*high*
Voltage [kV]	100	150	200
Current [µA]	35	66	100
Number of projections	750	1500	3000

Figure 5.45-a shows the distribution of the calculated MSR values: the mean MSR was found to be equal to 8 µm. The number of projections was found to exert the most significant influence on the MSR, while there is not an evident trend concerning voltage and current (Figure 5.45-c). However, it can be observed that center values (150 kV and 66 µA) seem to optimize the MSR. Indeed, 100 kV could be a too low voltage for a perfect penetration of alumina spheres and 200 kV could worsen the MSR if associated with high current due to a slight image saturation (e.g. 100 µA).

(a) Histogram

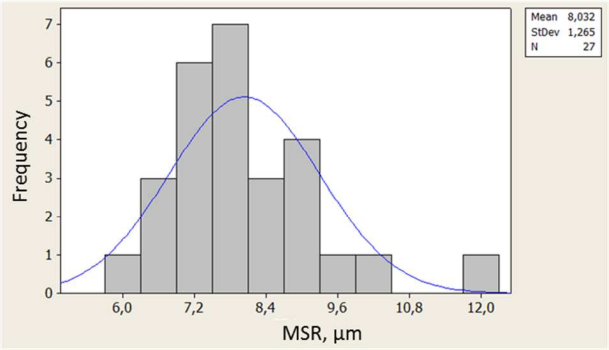

(b) Interaction plot for MSR

(c) Main effects plot for MSR

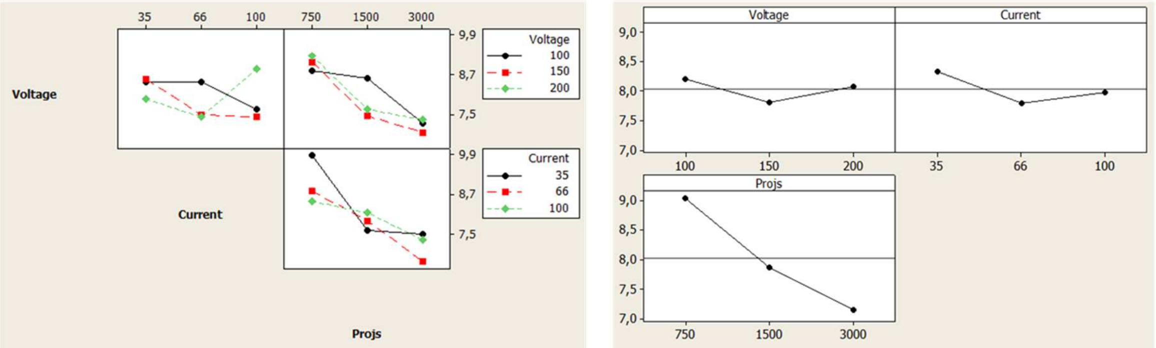

Figure 5.45: Histogram of MSR obtained on 27 scans with different parameters settings (a). Experimental design results (b)-(c) showing the influence of voltage, current and number of projections on data scatter for calculation of MSR by the 'Hourglass' method.

5.3.5 MSR verification tests by Hourglass method

A series of MSR verification tests was performed on the metrological CT system described in Section 1.4.1, using the 'Hourglass' standard made of alumina. Magnifications ranging from 11x to 70x were evaluated. The other scanning parameter are reported in Table 5.6.

Table 5.6: CT scanning parameters

Voltage	170 kV
Current	58 µA
Projections	1500
Exposure time	1000 ms
Scanning time	25 min
Orientation	Vertical

The software VGStudio MAX was used to analyze the obtained voxel-based volumes. The local adaptive thresholding method with search-distance equal to 4 voxels was employed for surface determination of all the reconstructed volumes investigated in this Section.

Besides computing the height *h* by equation (Eq. 5.6), the metrological structural resolution was evaluated using the improved measurement procedure (described in Section 5.3.2) by measuring 100 vertical distances with step-size of 2 µm. Measured distances were compared with the corresponding reference values. Metrological structural resolution (MSR) was then evaluated as the smallest dimension that can still be measured within a specified error limit.

A non constant *h/voxel size* ratio was obtain experimentally as shown in Figure 5.46. The measured height (*h*), representing the smallest measurable distance, was found to be below the voxel size for all the investigated magnifications.

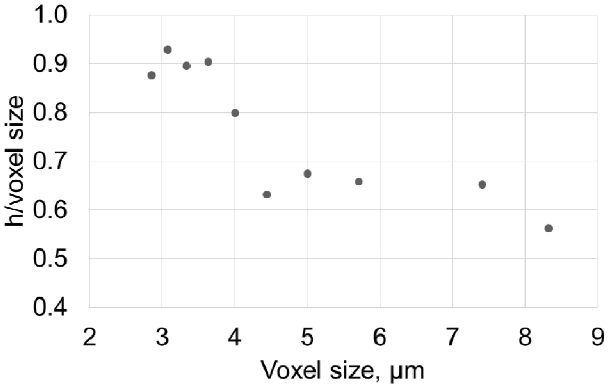

Figure 5.46: Ratio between measured *h* and voxel size plotted against the voxel size.

Figure 5.47 compares the multiple measured distances (plotted against reference values) obtained at two different magnifications taken as example: 18× and 27× with voxels sizes 11.1 and 7.4 µm respectively. It can be observed that, when the measured distance approaches zero, the deviations between measured and reference values increase significantly. As explained above, the MSR can be evaluated from these deviations based on a specified error limit. Figure 5.48 shows the relative measurement errors obtained for the two abovementioned magnifications. In this work, the limit was set at 20% of the relative measurement error, since it was observed to be well-representative of the rapid increase of errors considering all the investigated magnifications. In the two reported cases, for example, the MSR determined as the smallest dimension that can still be measured within an error limit of 20% ($MSR_{20\%}$) was found to be 26 and 18 µm for voxel size 11.1 and 7.4 µm respectively. Considering all the investigated magnifications, a non-linear relationship between MSR and voxel size was obtained.

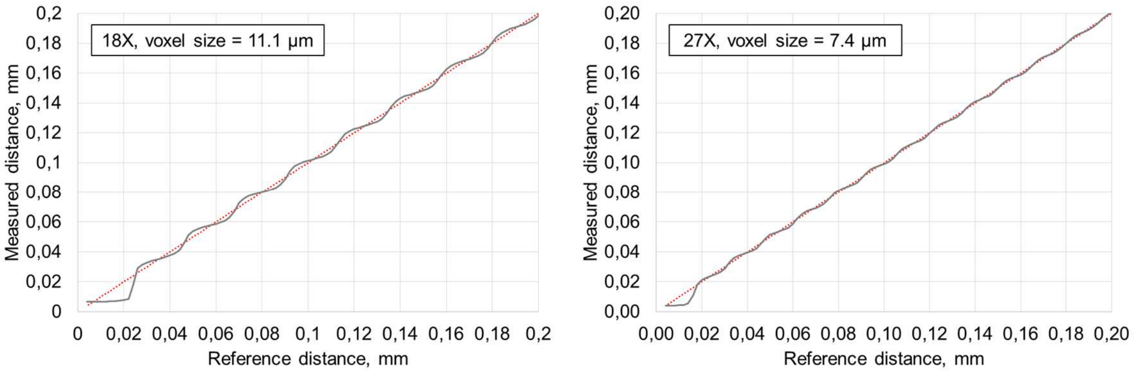

Figure 5.47: Measured values of one-hundred vertical distances (step-size 2 µm) plotted against reference values. Two magnifications are compared.

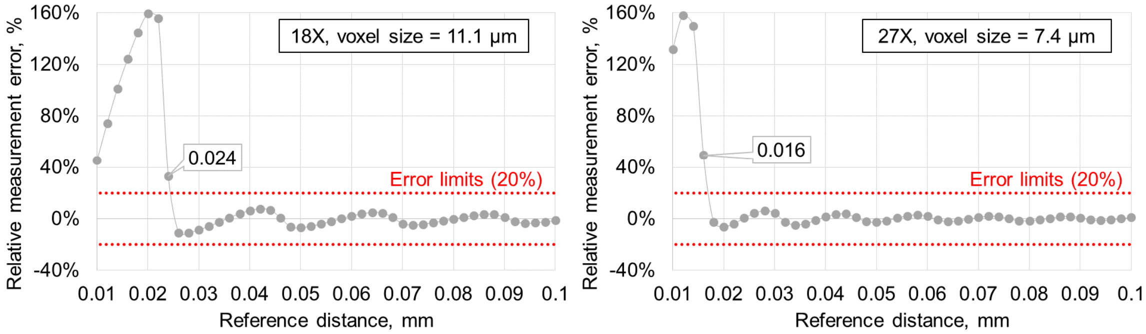

Figure 5.48: Relative measurement errors calculated for two magnifications. Horizontal lines represent the selected error limits.

5.3.6 Conclusions

In this Section, investigations on the metrological structural resolution of industrial CT systems were presented. MSR is an important metrological characteristic to be assessed during CT performance verification, together with length measurement errors and probing errors of size and form. In fact, it allows achieving additional information that are fundamental especially when scanning micro-components or part containing micro-features. The 'Hourglass' method, developed by the University of Padova, was improved by a new measurement strategy: multiple distances are measured and the MSR is evaluated by an adapted version of the definition proposed by the VDI/VDE 2617-13 [33]. Moreover, the 'Hourglass' method was compared with other proposed methods and the advantages connected to its application were pointed out in detail. Finally, a selection of influence factors affecting the method were evaluated by experimental and/or simulation analyses. At this moment, the ISO standard dedicated to industrial CT is under development and a standard test to evaluate the metrological structural resolution has still to be defined. As a conclusive remark, the ‘Hourglass’ method has proven to be an efficient, simple and fast method, allowing the evaluation of the MSR in conformity with the VDI/VDE 2630-1.3 definition.

Chapter 6

Porosity analysis of metal additive manufactured parts

This Chapter presents an experimental research work done in collaboration with the University of Twente, Netherland. Experimental analysis performed on Ti6Al4V SLM specimens were aimed at evaluating the accuracy of CT porosity analysis through comparison with well-established inspection techniques, such as Archimedes method, Gas Pycnometer and microscopic analysis of cross-sections. Influence factors affecting CT porosity analysis were identified and sphericity was investigated as morphology descriptor.

6.1 Background

Additive Manufacturing (AM) is a core technology for future high-value engineered products and is expected to change the landscape of industrial production in the coming years [97 98]. It has a great potential for producing complex, fully-customized parts in small scale-series [99]; however, standardized guidelines and methods for qualification assurance and verification need to be developed [100]. In fact, quality in AM of metals is still affected by high variability, showing limitations with respect to dimensional tolerances, surface finish and internal defects, thereby limiting its broad acceptance in several industrial applications. This variability can be minimized through process control. However, adequate measurement solutions are not available yet because of several metrological challenges, including the complexity of freeform shaped AM parts, high surface roughness, undercuts, voids and entrapped particles (see Figure 6.1). The development of accurate measuring methods would allow the production of higher quality AM parts accelerating the proliferation of their adoption into high-value sectors, such as aerospace, energy, medical devices, tooling and others. The implementation of innovative CT solutions in such AM industrial applications is highly relevant (see Figure 6.1), since it enables non-destructive analyses of geometrical features that in most cases are impossible with traditional measuring techniques (e.g. characterization of internal structures, complex freeform features and defects detection).

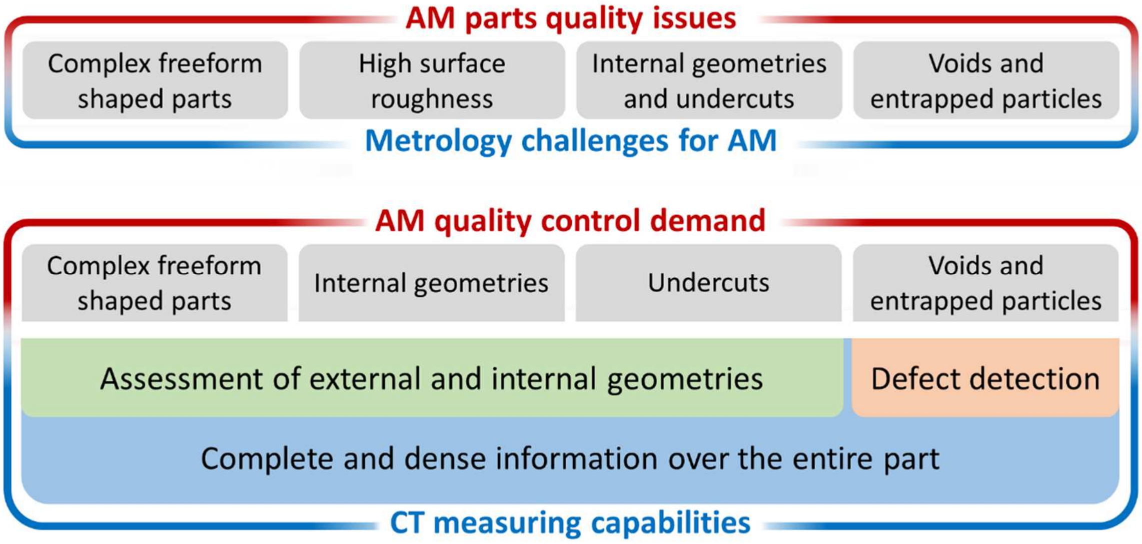

Figure 6.1: Scheme of AM parts quality issues that are challenging for metrology and AM quality control needs that can be addressed by CT.

This Chapter is focused on defect detection and porosity analysis. Selective Laser Melting was chosen (SLM) as metal-based AM technology for its versatility and capability to produce near full-dense parts. The SLM process selectively melts metallic powder using a focused laser beam. The melted powder attaches to the previous layer or support structure and solidifies in a short time. After that, a layer of new powder is recoated upon the current layer for the following layer melting [101] (Figure 6.2).

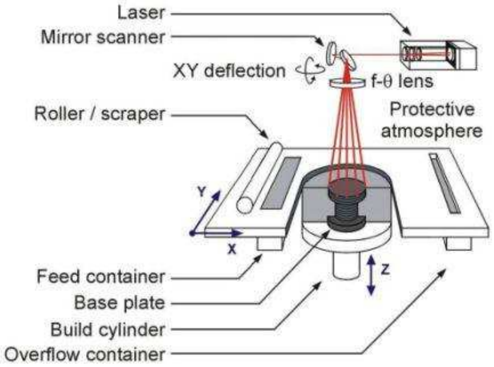

Figure 6.2: Schematic representation of Selective Laser Melting (SLM) technology.

Final part properties strongly depend on the in-layer scan strategy and the layer-to-layer properties [102], but due to the distinguished layer adding process and rapid cooling rate, SLM exhibits special microstructures and outstanding mechanical properties. Ti6Al4V powders are widely used in SLM for their inherent properties of fracture resistance, fatigue behavior, corrosion resistance and biocompatibility [103]. However, although SLM is capable of building high-density parts close to the nominal density, due to process instabilities gas bubbles, oxides and unmolten particles may be entrapped in Ti6Al4V AM parts [104-106]. In particular, pores cannot be avoided completely and may act as nuclei for cracks leading to possible reduced mechanical properties [107]. Size and distribution of pores are indicative for the process conditions, and are therefore useful for quality assessment. Moreover, the morphology of the pores is related to the type of defect [108]. For example, relative round pores are an indication of entrapped gas typically due to local overheating. In contrast, irregular shaped pores are an indication of unmolten particles typically due to insufficient energy (e.g. hatch pattern defects) (Figure 6.3).

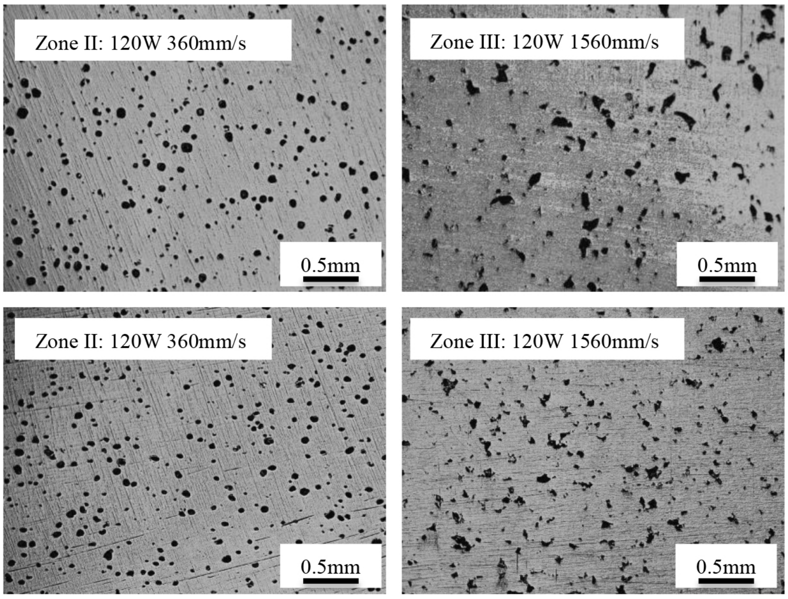

Figure 6.3: Cross-sections of SLM-produced specimens showing different types of defect due to overheating (left) and under heating (right) [108].

All of these porosity characteristics should be investigated for understanding pores effects on material properties. Since AM process can be also utilized to fabricate porous parts, a well-established knowledge about pores morphology, size and distribution can be useful to create structures that exhibit extreme flexibility in structural diversity and controlled porosity characteristics.

Internal defects can be evaluated by means of several inspection techniques. Non-destructive testing techniques such as (i) ultrasonic testing, (ii) Archimedes theoretical versus actual density, (iii) pycnometer and (iv) X-ray computed tomography are the most favourable, since SLM is still relatively expensive and one-off (high-value) products are more economically feasible than large series production. However, also destructive microscopic analyses of cross-sections (metallography) are performed quite often. Archimedes method and gas pycnometry are easy to be applied, but they are not capable of analysing fundamental porosity characteristics such as pores distribution and morphology, while metallography only allows investigations on a limited number of 2D cross-sections.

On the other hand, over the last years, quality control by CT scanning has emerged as an innovative possibility for AM parts, due to its unique capability of performing non-destructive porosity analysis and dimensional measurements of inner features. Consequently, CT has the potential to quantitatively evaluate the entire part for total pore volume, pore morphology and pore location and distribution.

6.2 Porosity testing methods

The porosity testing methods studied in this work can be subdivided into two groups in relation to the measurement type: (i) density-based testing methods (Section 6.2.1) allow an indirect evaluation of internal porosity, complementary to the measured part density while (ii) porosity-based testing methods (Section 6.2.2) lead to a direct evaluation.

6.2.1 Density-based testing methods

Two density-based testing methods were studied: Archimedes method and gas pycnometry.

The Archimedes method is based on the difference in buoyancy of an object's weight measured in air and submerged into a fluid (Figure 6.4). Advantages of the Archimedes method are that it is non-destructive, simple to be performed with commercial instrumentation, relatively inexpensive and quick. It can however only be used to determine a global density value relative to the reference fluid. To compute the part porosity, the measured density (obtained by (Eq. 6.1)) has to be compared to the material's nominal reference density (i.e. 4.43 g/cm^3). A lower density value results from increased part porosity. Localized porosities, due to e.g. process instabilities, can however not be assessed individually. Internal defects should be closed to avoid fluid to infiltrate the submerged part.

$$Density = \frac{W(air) \cdot \rho(fluid)}{W(air) - W(fluid)} \qquad \text{(Eq. 6.1)}$$

with $W(air)$ weight of solid in air, $W(fluid)$ weight of solid in fluid and $\rho(fluid)$ density of used fluid.

In gas pycnometry, a pycnometer computes part density in an absolute sense by measuring part volume and mass separately. Part volume is determined by gas displacement (Figure 6.5). An object of unknown volume is placed into a sealed sample changer of known volume. After sealing, the pressure within the sample chamber is measured. Then, an isolated reference chamber of known volume is charged to a certain pressure, greater than that of the sample chamber. A value isolating the two chambers is opened and the pressure of the system is allowed to equilibrate. The gas law (PV = nRT) is applied to determine the sample volume. Advantages of gas pycnometry are similar to the Archimedes method, although the equipment is a bit more expensive. The downside is the limited detection volume, allowing only relatively small parts to be measured. Analogously, only a global part density is measured, part porosity is computed by correlating a nominal reference density, and localized defects cannot be detected individually.

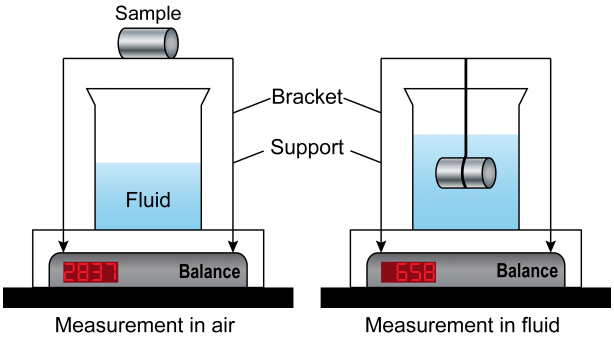

Figure 6.4: Typical setup employed for the Archimedes method.

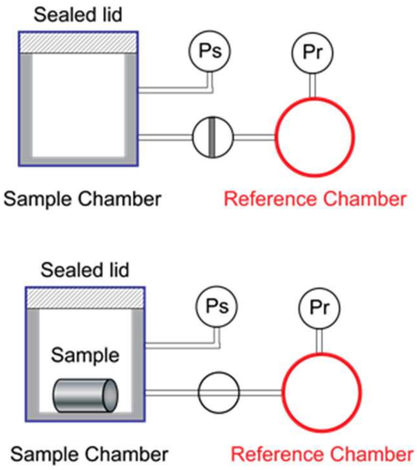

Figure 6.5: Schematic of a pycnometer that uses a gas displacement technique.

6.2.2 Porosity-based testing methods

In addition to the described density-based testing methods, two porosity-based testing methods are studied as well: microscopic analysis of cross-sections and X-ray CT.

In the first method (Figure 6.6), the sample is cut, embedded in epoxy resin, grinded, sanded with abrasive paper and finally polished. A microscope is used to capture micrographs that are analyzed by image processing software and, possibly, capable of automatic image stitching.

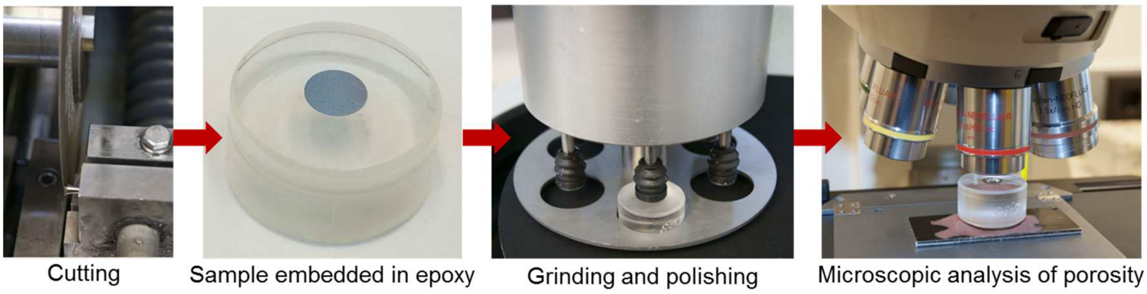

Figure 6.6: Operations needed for microscopic analysis of porosity.

A pre-elaboration of the image is required to remove any residual scratch of the polishing procedure and to get a binarized image after the selection of an appropriate threshold value. The porosity percentage can be calculated as the ratio between black pixels count and white pixels count, while the pore's area can be evaluated by knowing the pixel size of the image. This testing method allows the assessment of pore size and distribution, giving more information than the density-based methods, but confined to specific sections of the specimen. Thus, for non-homogeneous distributions of pores, the obtained results are not representative of the entire part. However, the most relevant disadvantage is the destructive nature of this method together with the high cost in terms of material and time usage.

The second method, X-ray CT, has been recently utilized as innovative non-destructive measuring technique for internal porosity detection thanks to its capability of providing a complete analysis of size, shape, volume and distribution of pores/defects within the entire analyzed volume. As explained in Section 2.3 of this thesis, after the 3D volume reconstruction, advanced segmentation algorithms can be applied through setting of a grey value threshold to discriminate between air and the object material, and information about internal porosity can be extracted. Relevant drawbacks are the high cost and the high time usage. Moreover, the establishment of metrological traceability of CT porosity measurements is still a challenging task [57]. CT volumes reconstructed in this work have a voxel size of 9 µm. The total CT porosity volume is measured using the defect detection module implemented in the software package VGStudio MAX.

6.3 Comparison of porosity testing methods

Previous works have dealt with the comparison of CT with other well-established inspection techniques such as Archimedes method and microscopic analysis [109, 110]. However, reference porosity measurements were not available in these works, although they are necessary for measurement errors assessment. In the present Section, CT is compared with the other abovementioned methods for porosity detection considering both volume-based analysis with respect to pycnometer and Archimedes methods (Section 6.3.2) and area-based analysis regarding the metallographic method (Section 6.3.3) as schematized in Figure 6.7.

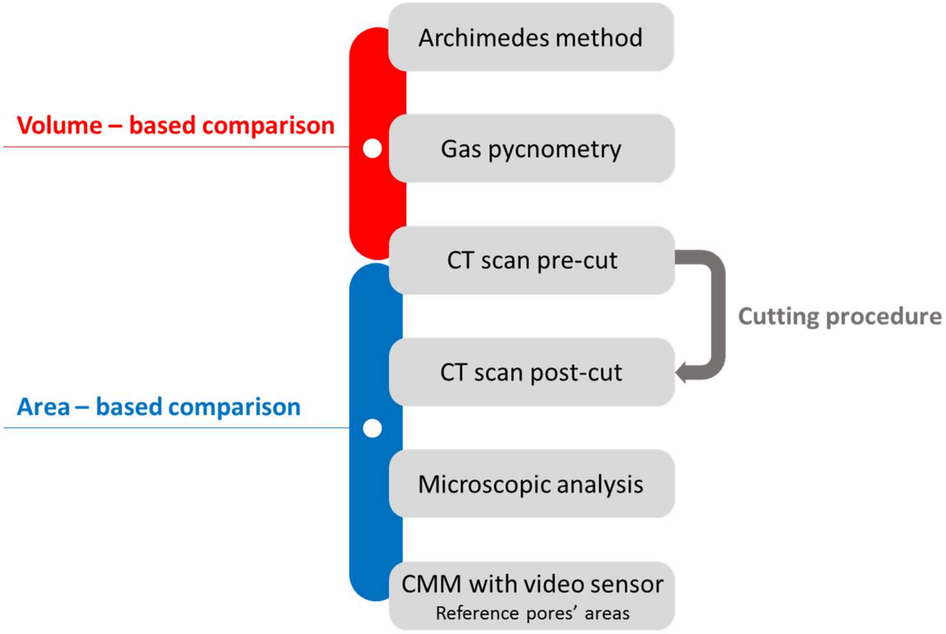

Figure 6.7: Procedure for the comparison between methods.

Figure 6.8 summarized the characteristics of these methods.

	Archimedes	Pycnometer	Metallography	X-ray CT
Non-destructive technique	●	●	○	●
Global porosity (entire part)	●	●	○	●
Pores distribution	○	○	●	●
Pores morphology	○	○	●	●
Volume-based analysis	●	●	○	●
Area-based analysis	○	○	●	●
Density-based analysis	●	●	○	○
Porosity-based analysis	○	○	●	●
Limited part size	○	●	○	◕
Complex procedure	○	◔	◕	◑
Fast procedure	●	◕	○	◔
Cheap procedure	●	◕	◔	○

● Fullfield ○ Not fullfield

Figure 6.8: Comparison of different aspects for porosity testing methods.

6.3.1 SLM test part production

Following an experimental design, a total of 40 SLM tensile test specimens were produced by the University of Twente, Netherland. Titanium alloy Ti6Al4V (grade 5) was selected as build material for its wide interest in aerospace, biomedical and industrial fields. The build layer thickness was 50 µm. One set of test specimens was oriented horizontally; the other set was oriented vertically with respect to the platform, as shown in Figure 6.9. In Figure 6.10-a the printed specimens are shown for the vertically produced test sets. After production, full annealing was performed at 735 °C for 2 h. Then, after fast cooling under a protective atmosphere, the parts were removed from the build plate. Thereafter the parts underwent a solution heat treatment (928 °C for 1 h) and aging heat treatment (538 °C for 3 h) followed by fast cooling under a protective atmosphere. Finally a post processing operation by machining was performed. A selection of 6 parts (3 for vertical orientation named V8, V12 and V20 and 3 for horizontal orientation named H1, H17 and H18) was selected to be analysed by the aforementioned porosity testing methods, after tensile testing (Figure 6.10-b).

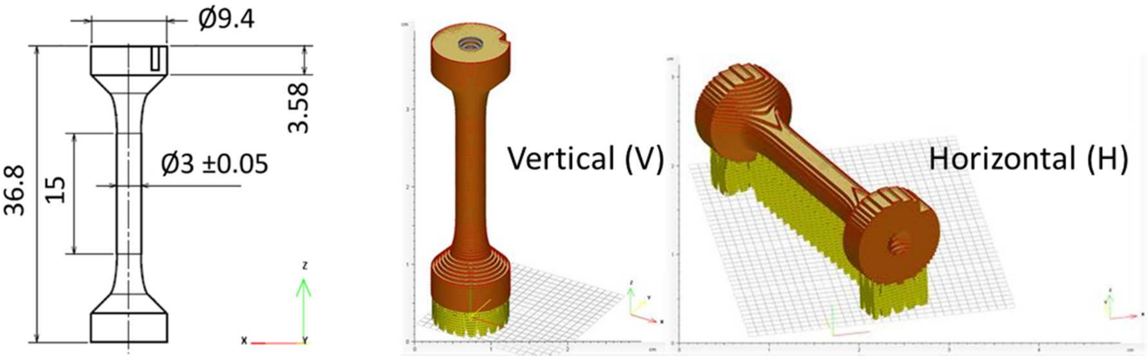

Figure 6.9: Test part geometry (left); vertical and horizontal building orientations (right).


(a)

(b)

Figure 6.10: 20 tests parts manufactured with vertical orientation (a); example of specimen after tensile testing (b).

6.3.2 Volume-based porosity testing methods

6.3.2.1 CT vs Archimedes method

In this study, for the Archimedes method, ethanol is used as reference fluid and a Sartorius R200D electronic semi-microbalance is used to measure the samples weight. The metrological CT system used for this work was already introduced in Section 1.4.1. Figure 6.11 shows two representative CT reconstructed volumes (samples V12 to the left and H17 to the right), with a 50% transparency in order to allow the visualization of internal defects distribution.

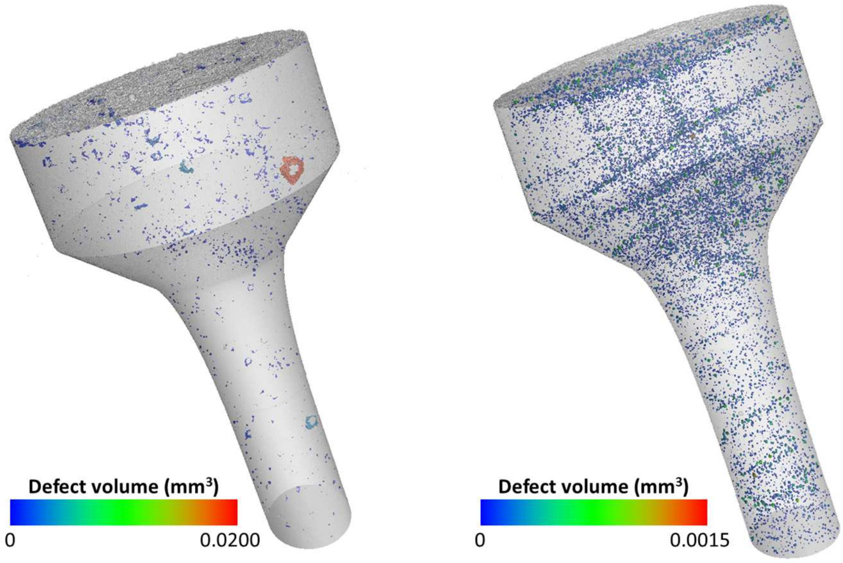

Figure 6.11: CT porosity analysis of sample V12 (left) and sample H17 (right).

Comparative results between Archimedes method and CT are plotted in Figure 6.12. The computed relative densities are reported on the vertical axis. As visible, both methods show the same trend. However, the Archimedes density is systematically lower (0.2 - 0.4 %) than the density measured by CT. This is likely due to the inherent differences between the two testing methods. Archimedes can be considered accurate in absolute density measurements, but for deriving the relative density, as well as the porosity percentage, it is necessary to take the nominal density of Ti6Al4V (4.43 g/cm3) as reference. This density, however, cannot be considered reliable for non-homogeneous parts as AM produced parts. On the other hand, CT results are influenced by several image artefacts (e.g. due to X-ray beam hardening and scattering), by the achieved resolution (e.g. pores with sizes lower than the spatial resolution cannot be detected) and by the surface determination procedure. Further research work is needed to evaluate the measurement uncertainty of CT porosity analysis.

Finally, unmolten powder residue can be another source of diversity. The effect of CT resolution, surface determination procedure and presence of entrapped powder residue will be further discussed in Section 6.4.

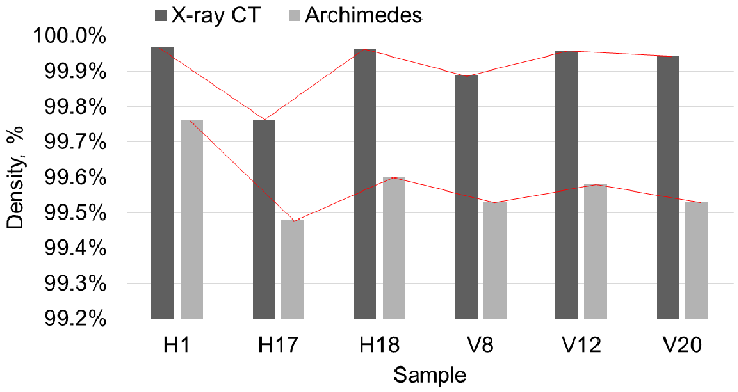

Figure 6.12: Comparison of Archimedes methods and CT for density analysis.

6.3.2.2 CT vs pycnometer

In this study, a Quantachrome Instruments Ultrapyc 1200e pycnometer (University of Padova) was used. The pycnometer is accurate in measuring part volumes. On the contrary, the part density evaluation is affected by the used balance for mass measurement and by the use of nominal density as reference (as already discussed for the Archimedes method). Results reported in Figure 6.13 show that volumes measured by pycnometer are almost equal to those measured by CT. This is evident for samples V8 and V20, while for sample H1, H18 ad V12 a systematic difference occurs. This difference can be explained from the fact that samples V8 and V20 have smaller heights, so it was possible to fit them totally inside the detector field of view during CT scans. The end part of the other three samples fell out of detector borders so the CT computed volume, as expected, is systematically smaller than pycnometer's. However, Figure 6.14 shows that densities evaluated by the two methods are not in good agreement and pycnometer sometimes calculate a density higher than 100%. These results were confirmed in a second test with another pycnometer at another laboratory (University of Twente). The disparity is likely due to insufficient accuracy for such small porosity percentages and due to the poor reliability of the nominal reference density for non-homogeneous parts.

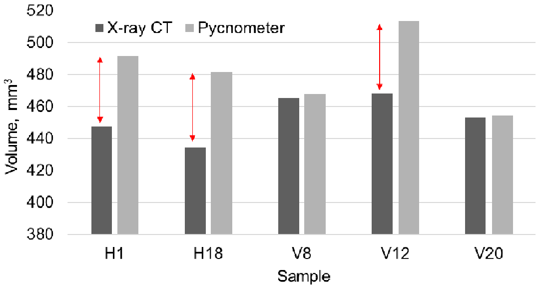

Figure 6.13: Comparison of pycnometer and CT for volume measurements.

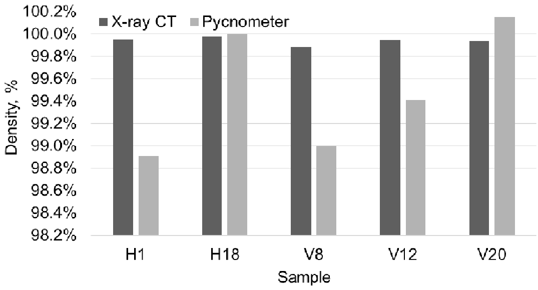

Figure 6.14: Comparison of pycnometer and CT for density analysis.

6.3.3 Area-based porosity testing methods

6.3.3.1 CT vs Microscopic analysis of cross-sections

A Zeiss Axioplan 2 microscope is used in this work to capture micrographs, which were then analyzed by Axiovision image processing software capable of automatic image stitching.

First of all, three specific cross-sections were selected on one half of each tensile tested component, as shown in Figure 6.15 (left), and computed porosity contents were averaged to obtained percentage densities. The obtained results are reported in Figure 6.15 (right) and compared with CT results. It can be observed that, even if some results have a very good agreement (e.g. H1 and V20), there is not a similar trend. The most probable explanation is that three cross-sections cannot be sufficiently representative for the global porosity content. On the other hand, analyzing more sections would mean more cutting operations to be performed and increased labour cost and time. Moreover, another source of diversity can be that the cross-sections were taken on one half of the tensile tested components, while CT analyses were performed on the other half part.

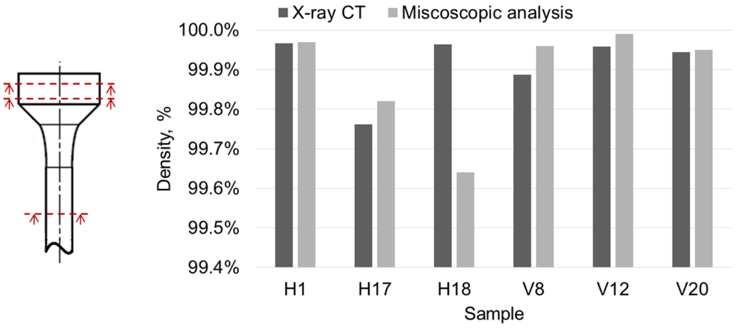

Figure 6.15: Cross-sections considered for density analysis (left); comparison of microscopic analysis and CT for density analysis (right).

The comparison between CT and microscopic analysis of micrographs was further investigated through a new developed procedure, schematized in Figure 6.7 (area-based comparison). The entire specimen was CT scanned to identify the coordinates of a section of interest (e.g. a layer showing irregularities) before performing the cutting procedure. After cutting procedure and microscopic analysis of the obtained cross-section, a second CT scan was conducted on the cut part. Then, a best fit alignment with the pre-cut scanned volume was addressed to identify the exact location of the cross-section in the pre-cut volume (Figure 6.16), where a 2D CT defect analysis was performed (same algorithm and thresholding parameters applied for the 3D defect analysis). In this way, differently from other works dealing with a similar comparison, the cross-section analyzed by microscope can be compared with the corresponding cross-section in CT volume and, furthermore, the same cross-section can be evaluated both before and after cutting and polishing procedures (see Figure 6.17). Finally, specific pores lying on the cross-section of interest were measured using a high accuracy multisensory CMM equipped with image processing sensor (Werth Video-Check-IP 400; maximum permissible error, MPE, equal to (1.8+L/250) µm, with L in mm) to get reliable reference values for pore areas. Coordinates (x, y) of pores contour were extracted and contained areas calculated with Matlab (Figure 6.18). Moreover, a calibrated 1 mm optical line pattern was measured at the same magnifications to verify if the MPE of the system was respected (Figure 6.18).

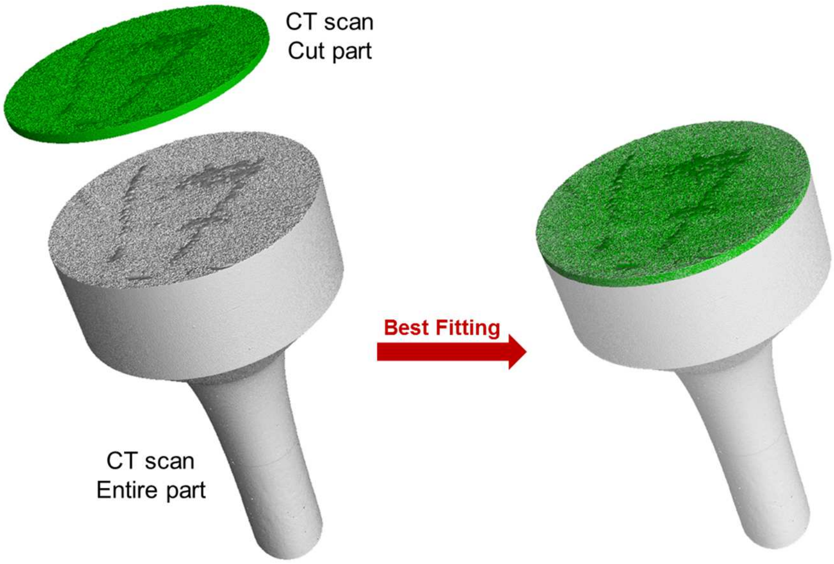

Figure 6.16: Best fit alignment between CT reconstructed volumes of entire part and cut part.

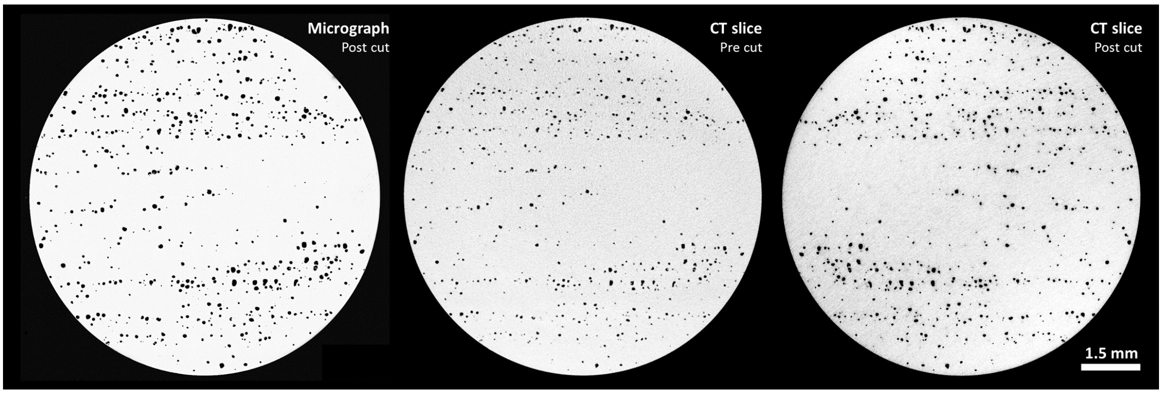

Figure 6.17: Comparison between micrograph and corresponding CT slices obtained before and after cutting operations (Part H17).

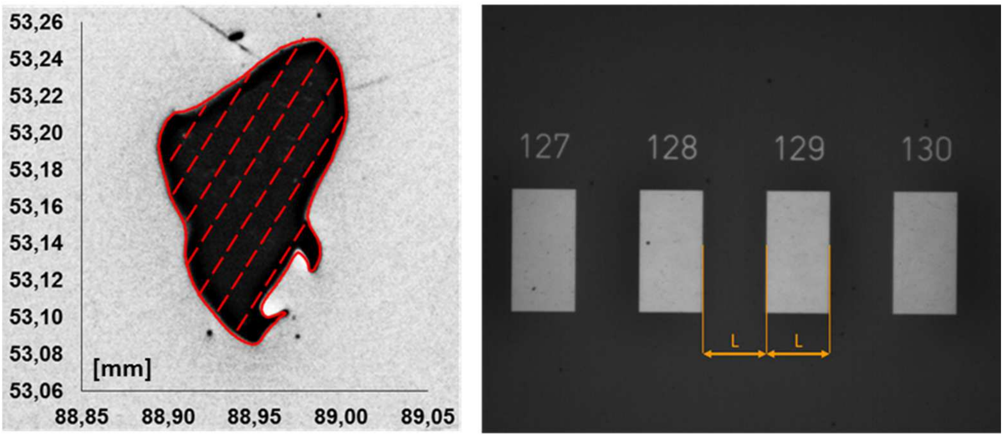

Figure 6.18: Example of pore measured by means of a CMM equipped with video sensor (left): coordinates of pore contour can be extracted and the contained area can be measured with high accuracy. Calibrated 1mm-line pattern (L = 0.5 mm) measured at the same magnification (right) to verify if the MPE of the machine is respected.

The aforementioned procedure was applied on three different specimens. Figure 6.19 shows two different cut directions, the first for parts H1 and H17 and the other for part V20. The two directions were chosen in order to consider different dynamics with regard to the presence of entrapped powder residue inside voids (see Section 6.4).

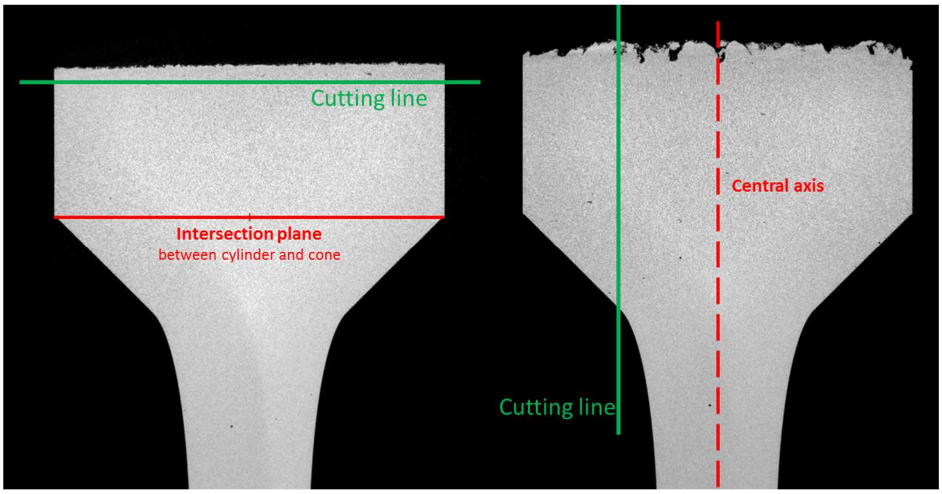

Figure 6.19: Two different cutting direction used for the comparison between micrographs and CT.

The diagram in Figure 6.21 shows the area measurements of 24 pores lying in one cross-section of Part H17, obtained by CT (pre-cut and post-cut), microscopic analysis and CMM equipped with video sensor. Cross-sections on the other two specimens were analyzed as well and confirmed these results. The microscopic analysis results are very close to the CMM results, while CT always measures smaller areas. This is visually confirmed by Figure 6.17, in which one micrograph is compared with the corresponding CT slice (pre-cut and post-cut). Both optical techniques and CT are influenced by several factors which could partially explain the observed diversity. The CT main influences were already discussed in Section 6.3.2.1; while optical measurements can be influenced by light and focus settings, stitching operations, thresholding and binarization. Other possible causes can be deformations due to cutting/polishing operations and the presence of entrapped unmolten powder residue that may fall out during the cutting operation. These causes find an evidence in the difference between CT pre-cut and CT post-cut results: CT pre-cut area measurements are systematically lower compared to CT results obtained after cutting. A number of internal sections were compared as well to demonstrate that this difference regards only the cut sections.

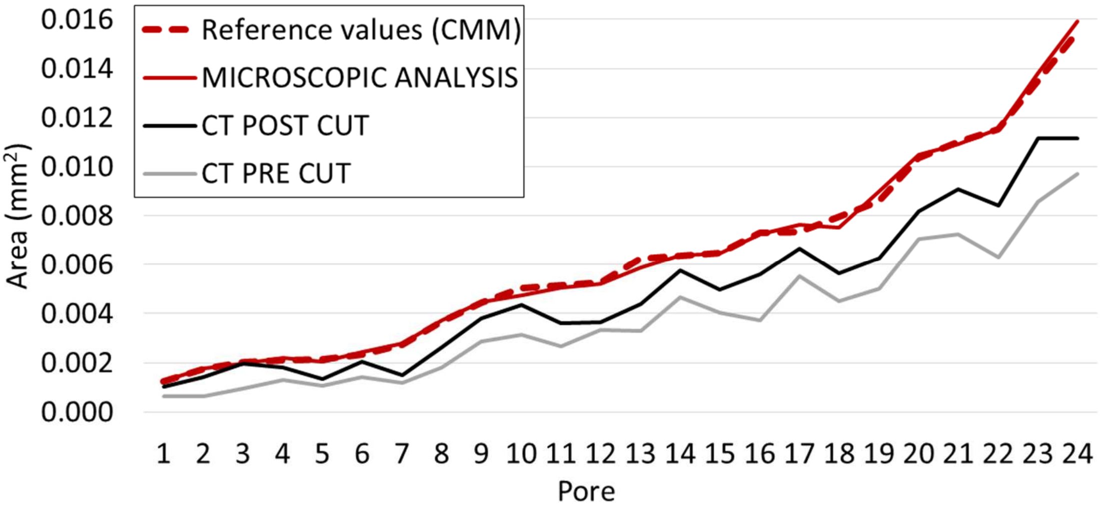

Figure 6.21: Pore size comparison for CMM, micrograph and pre/post-cut CT.

6.4 Investigation on influence factors for CT porosity analysis

6.4.1 Surface determination procedure

For each analyzed component, two different surface determination methods were compared. In both cases an advanced locally-based surface determination procedure was applied, but two different starting threshold values were selected: ISO50% value and manual value. Comparative results are shown in Figure 6.22. With the manual threshold value, CT densities were found to be closer to densities computed by Archimedes method (as seen in Section in 6.3.2.1) The manual value was selected by averaging the grey values of a number of ROIs (Region of Interest) representing the material and the background (in this case the inner part of pores). This procedure allows minimizing errors in pores volume measurements, since the threshold value is optimized based on gray values of pores, which could be different than the external background. The improvement due to the manual threshold value was further confirmed by simulation of ideal spherical pores with known nominal volume.

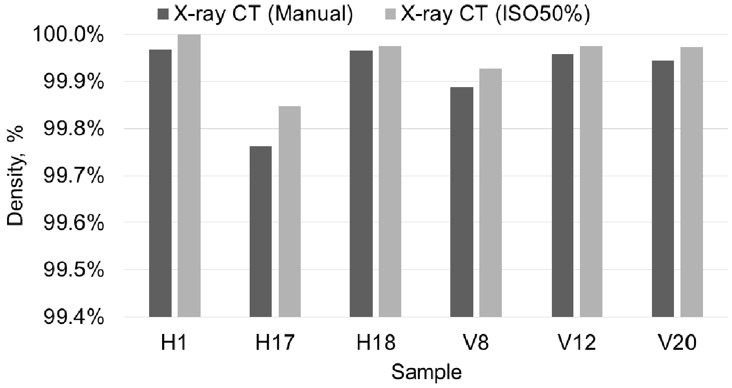

Figure 6.22: Comparison of CT percentage densities obtained with two different thresholding approaches.

6.4.2 CT resolution in terms of voxel size

The CT resolution in terms of voxel size can affect the CT porosity analysis: pores with diameter below two times the voxel size are difficult or even impossible to be measured, while larger pores but with diameter still close to the voxel size can lead to significant volume measurement errors. To evaluate the influence of the voxel size, a simulation was performed with voxel size equal to 9 µm, absence of noise and focal spot approximated to a single point. A Ti6Al4V cylinder with diameter 10 mm and height 3 mm was simulated, containing a total of 21 spherical pores with *pore diameter/voxel size* ratios ranging between 0.5 and 15 (cylinder dimensions as well as pores size range were chosen to be similar to the real case of specimen H17). As illustrated in Figure 6.23, 7 different pore sizes were considered and repeated in 3 planes contained in the simulated cylinder. Figure 6.24 show percentage deviations of volume measurements computed as measured volume minus nominal volume. Pores with *pore diameter/voxel size* ratio equal to 1 or lower were not detected so they are not reported in the diagram, while pores with ratio equal to 2 have an average error higher than 40% with a high standard deviation too. Errors signs are negative, meaning that the resolution effect can be reasonably considered one of the causes of systematic deviations observed in the comparison with the other methods.

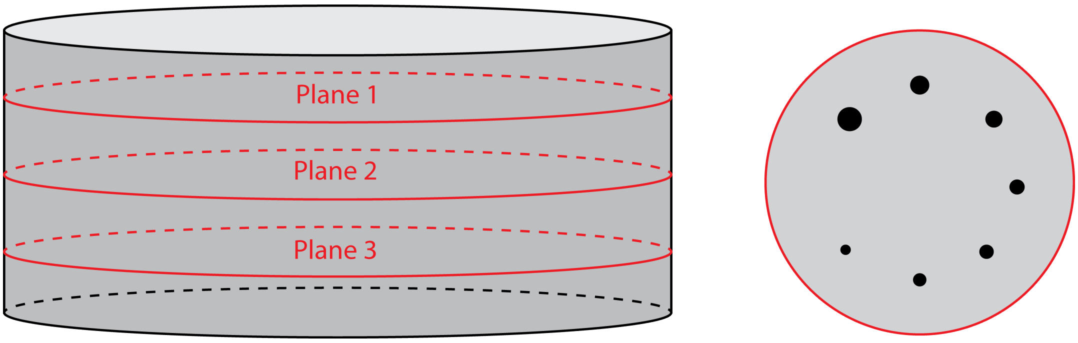

Figure 6.23: Schematic representation of the simulated cylinder containing 21 spherical pores distributed over 3 planes (left); example of pores position in each plane (right).

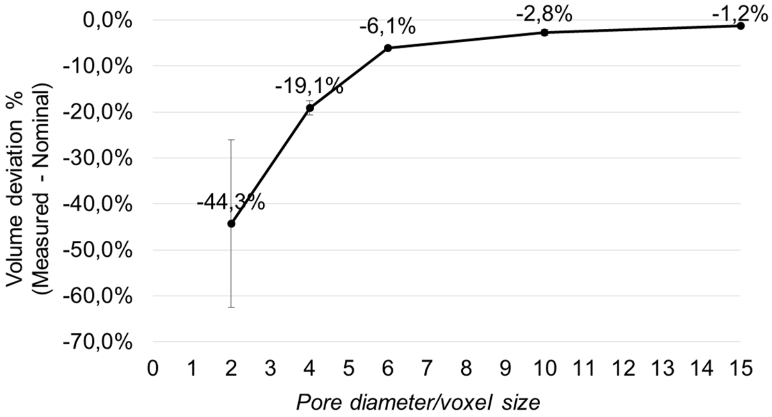

Figure 6.24: Volume measurement deviations for pores with *pore diameter/voxel size* ratio ranging between 1 and 15.

6.4.3 Entrapped unmelted powder residue

Figure 6.25 compares one micrograph and the corresponding CT slice (pre-cut) of part V20, which was cut along the vertical direction. This direction was chosen in order to analyze the presence of entrapped powder residue, e.g. visible inside the big pore located to the right part of the section. The image in Figure 6.26, acquired by Scanning Electron Microscope (SEM), shows this specific pore magnified, confirming the presence of entrapped unmelted powder.

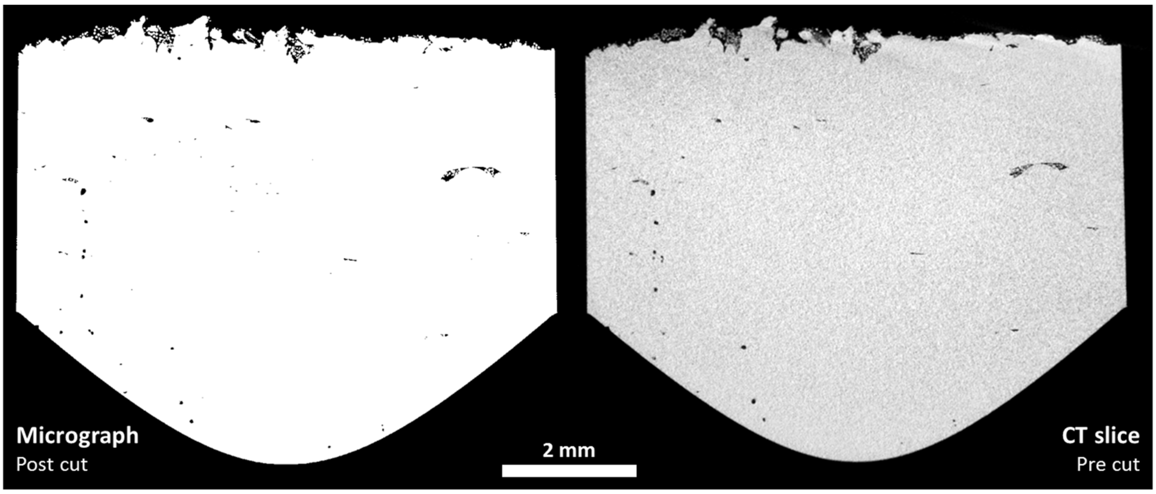

Figure 6.25: Comparison between micrograph and corresponding CT slices obtained before cutting operations (Part V20).

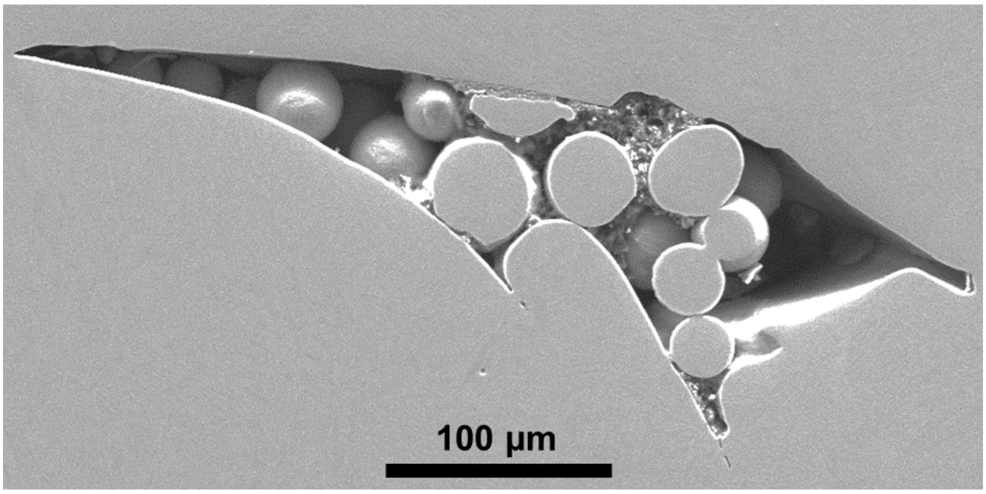

Figure 6.26: SEM image showing unmelted powder residue entrapped inside an internal pore.

Figure 6.27 illustrates how the presence of powder residue inside voids can contribute to the systematic difference between the different methods presented in previous sections. For example, CT can measure smaller volumes in comparison with Archimedes method due to resolution limits. After cutting and polishing operations, some particles may fall out. Consequently, pores areas measured by CT would be smaller than the same areas measured by microscope. Moreover, this can be one explanation of the difference between pores areas evaluated by CT before and after cutting.

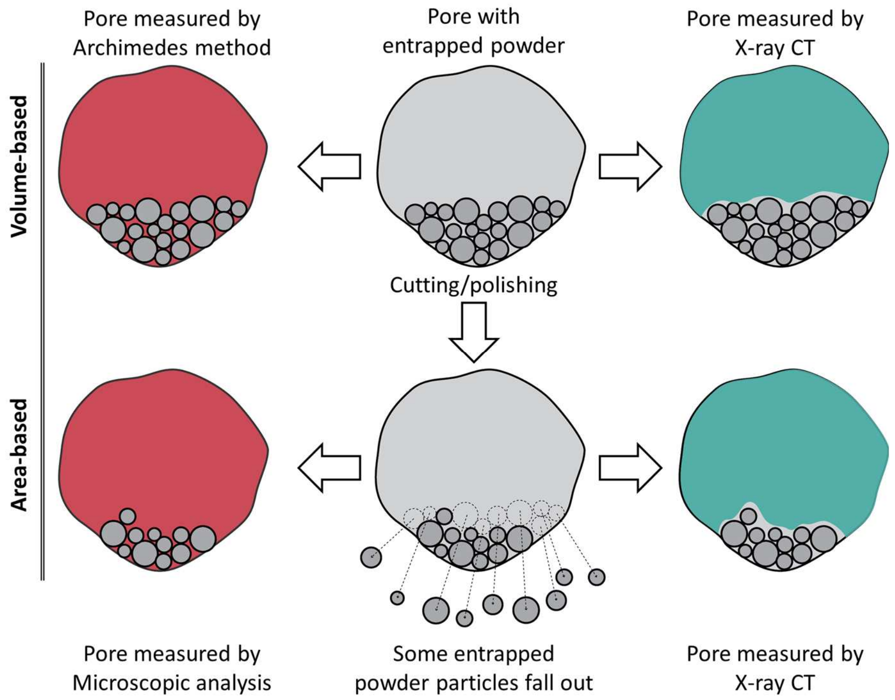

Figure 6.27: Effect of entrapped unmelted powder particles on results obtained by volume-based and area-based porosity testing methods.

To further understand the effect of unmelted powder residue entrapped into voids, simulations of two types of void with same volume (contained in a Ti6Al4V cylinder) was done: one void was characterized by the presence of 4 entrapped spherical particles, the other was empty. Two magnifications were considered in order to add the effect of the voxel size to the evaluation. The obtained voxel sizes were 6 µm and 9 µm. Table 6.1 reports dimensions of simulated cylinder, voids and entrapped particles.

Table 6.1: Dimensions of simulated cylinder, voids and entrapped particles.

Cylinder	Height (Hc) = 3 mm
	Diameter (Dc) = 10 mm
Void 1 (Empty)	Radius (R1) = 0.0182 mm
	Volume (V1) = 0.000025 mm^3
Powder particles	Radius (Rp) = 0.0100 mm
	Volume (Vp) = 0.000004 mm^3
Void 2 (Entrapped particles x 4)	Radius (R2) = 0.0215 mm
	Volume (V2_empty) = 0,000042 mm^3
	Volume (V2) = V2_empty-4*Vp V2 = V1 = 0.000025 mm^3

Results obtained for simulated voids are depicted in Figure 6.28 for the two considered magnifications. Two surface determination modes (ISO50% and manual), already explained in Section 6.4.1, were applied. It can be observed, that the presence of entrapped powder particles causes an increase of percentage errors (all with negative sign) for both magnifications. However, at the highest magnification (voxel size 6 µm) deviations are far less pronounced. With voxel size equal to 9 µm and ISO50% thresholding mode, void 2 is not even detected by the defect detection module of the used software, so the deviation is 100%. As seen in Section 6.4.1, the manual surface determination mode is confirmed to decrease measurement errors, but concerning void 2 and voxel size 9 µm the percentage deviation remains high (about 50%).

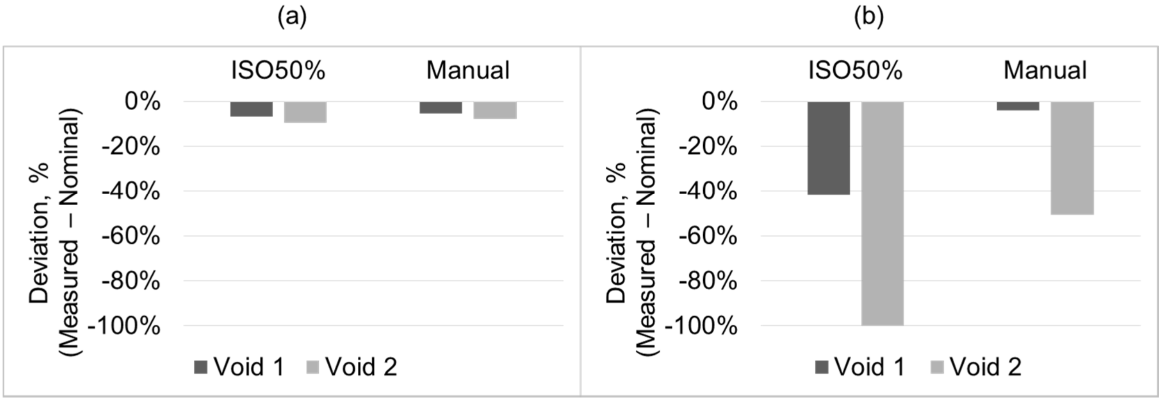

Figure 6.28: Simulation of two voids with the same volume: Void 1 is empty, while void 2 contains 4 entrapped particles of powder. Two thresholding modes (ISO50% and Manual) were applied and two different voxel sizes were considered: 6 µm (a) and 9 µm (b).

6.5 Sphericity

Sphericity is a measure of how spherical (round) an object is. As such, it is a specific example of a compactness measure of a shape. Defined by Wadell in 1935 [111], the sphericity (ψ) of a particle is the ratio of the surface area of an ideal sphere with the same volume of the given particle to the measured surface area of the particle:

$$\psi = 4\pi\left(\sqrt[3]{\frac{3V}{4\pi}}\right)^2 \cdot \frac{1}{S} \qquad \text{(Eq. 6.2)}$$

with V measured pore volume and S measured pore surface.

The sphericity of a sphere is unity by definition and, by the isoperimetric inequality, any particle which is not a sphere will have sphericity less than 1 as shown in Figure 6.29.

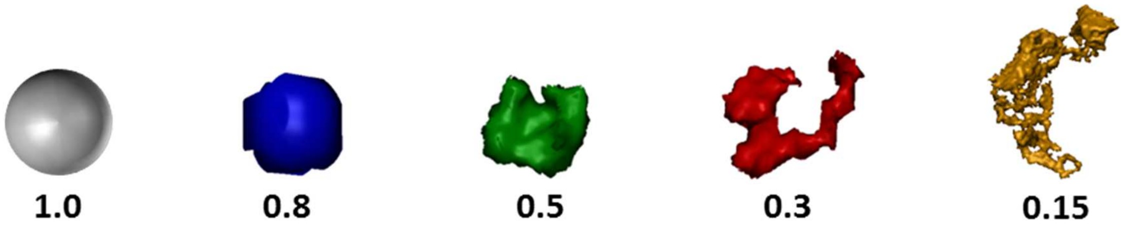

Figure 6.29: Example of pores with different morphology coupled with their relative sphericity value.

The Wadell's sphericity definition is included in the standard ISO 9276-6:2008 [112] concerning the shape and morphology of particles. Moreover, the standard says that, according to Cauchy's theorem for convex particles, if the particle (in this case the pore) is projected in average position, then its surface area can be approximated by 4 times the mean projection area. As suggested in [113], in order to reduce errors, this approximated area can be used to calculate sphericity as:

$$\psi = \frac{4 \cdot mean(PX, PY, PZ)}{S} \qquad \text{(Eq. 6.3)}$$

with PX, PY, PZ pore projection areas (provided by the Defect Detection module of VGStudio Max) and S pore surface.

The accuracy of this definition can be improved by using more projections, for example by a rotation of the coordinate system and a repeated determination of three projection areas applying Defect Detection [113]. However, this improved procedure will require a high amount of time.

Both (Eq. 6.2) and (Eq. 6.3) were applied to the SLM tensile specimens studied within this Chapter. Figure 6.30 shows results obtained on two parts (H1 and H17) taken as examples: sphericity is plotted against the voxels contained in the pore volume. It can be observed that using the definition 1 (Eq. 6.2) the maximum measurable sphericity is 0.81, which corresponds to the sphericity of a cube. This limit is due to the fact that Defect detection algorithm has only voxel size accuracy. On the contrary, with Definition 2 (Eq. 6.3) sphericity higher than 0.81 can be obtained. However, sphericity occurred to be even higher than 1 for small pores containing less than 50 voxels.

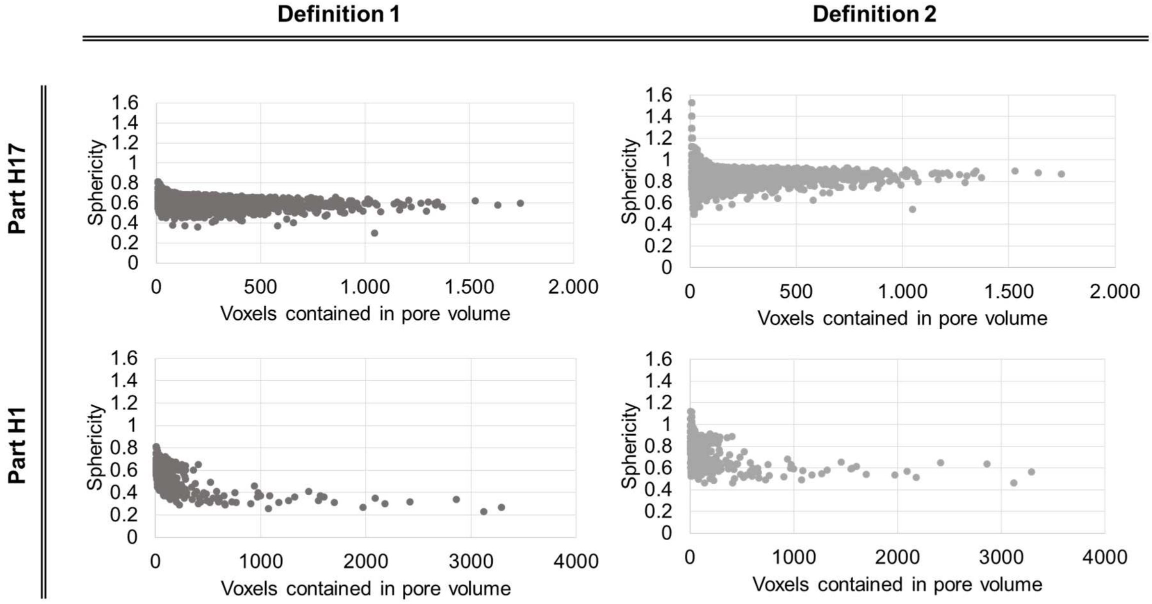

Figure 6.30: Sphericity of part H1 and part H17 computed by definition 1 (Eq.6.2) and definition 2 (Eq. 6.3).

The simulation described in Section 6.4.2 and Figure 6.23 was used again in order to apply the sphericity definitions on ideal spherical pores with known size and to get a better understanding on the accuracy of such definitions. Figure 6.31 compares results obtained from the Defect Detection algorithm and from the determined surface, in both cases using the definition 1. From this comparison, it’s clear how the accuracy of the Defect Detection algorithm, (which is limited to the voxel size) affects measurements of volume, surface and sphericity. In particular, surface measurement errors were found to be very high, while volume measurement errors increase for very small pores (diameter ≤ 4 voxels). Consequently, sphericity deviations are constantly around 30% if the pore diameter is higher that 2 voxels. On the contrary, sphericity deviations obtained from the determined surface are almost equal to zero, thanks to the sub-voxel accuracy offered by the advanced thresholding procedure. The situation is slightly different for pores with diameter equal to 2 voxels, for which sphericity percentage errors are around 20% in both cases (but with opposite signs). Moreover, definition 2 led to the same results achieved with the determined surface (see Figure 6.32-a). These simulation results were confirmed also by real scans of high-precision ruby spheres of different materials. The reconstructed spheres volumes were imported in the elaboration software with an inverse ramp filter in order to be treated as pores by the Defect Detection algorithm. Results fit well to simulation results, as seen in Figure 6.32-b.

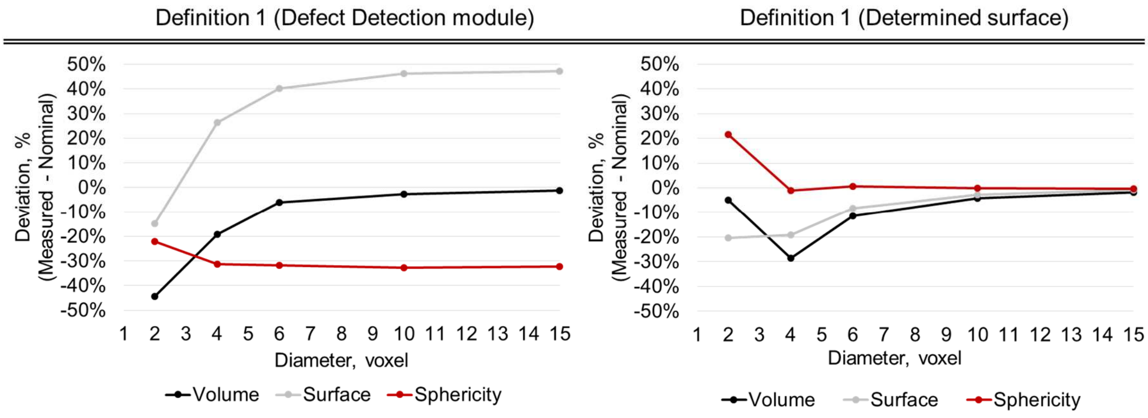

Figure 6.31: Volume, surface and sphericity deviations obtained by applying definition 1 using the Defect Detection module (left) and the determined surface (right).

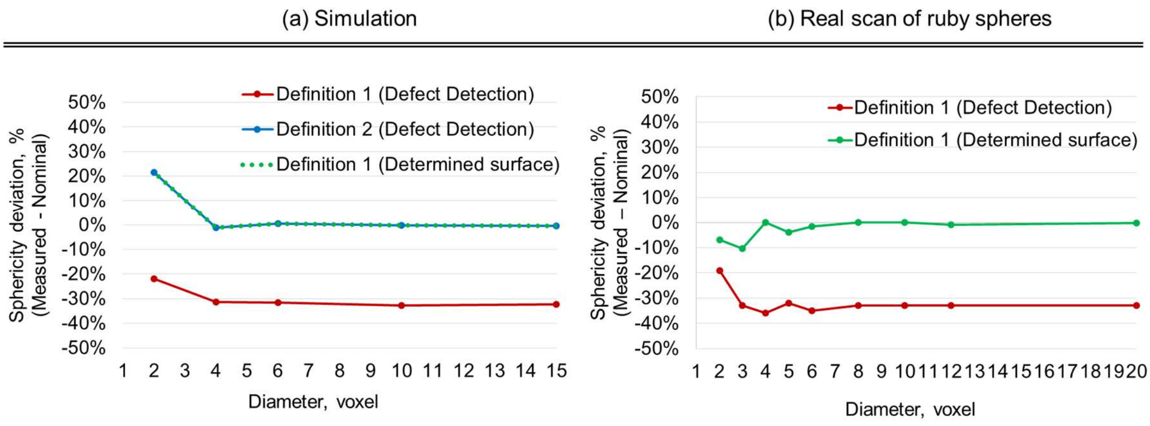

Figure 6.32: (a) Comparison of sphericity deviations obtained with simulations by definition 1 applied both using the Defect Detection algorithm and the determined surface and definition 2. (b) Comparison of sphericity deviations obtained by Defect Detection algorithm and determined surface (definition 1) on real CT scanned ruby spheres.

Since real pores have often non-spherical shapes, another simulation was performed featuring four non-spherical shaped pores (L-shaped, ellipsoidal, cylindrical and cubic) and one spherical pore. Table 6.2 lists nominal volume, surface and sphericity for these pores and Figure 6.33 compares the nominal sphericity of each pore with sphericity measured by definition 1 and 2. Sphericity errors made by the Defect Detection module (definition 1) were found to be again around 30%. Sphericity calculated by the determined surface is closer to the nominal sphericity than the one calculated with the Defect Module (definition 1). Also definition 2 leads to results near to the nominal sphericity, except for the cubic pore (sphericity > 1). It can be concluded that, except for pores with diameter equal to 2 times the voxel size (volume containing 8 voxels), the error made by the Defect Detection module of elaboration software VGStudio Max in calculating pores sphericity is systematically equal to -30%.

Table 6.2: Nominal volume, surface and sphericity of 5 simulated different-shaped pores.

Pore shape	**Volume, mm^3**	**Surface, mm^2**	**Sphericity**
“L” shaped	0.0008	0.0668	0.38
Ellipsoid	0.0004	0.0400	0.64
Cylinder	0.0004	0.0339	0.75
Cube	0.0004	0.0316	0.81
Sphere	0.0004	0.0254	1.00

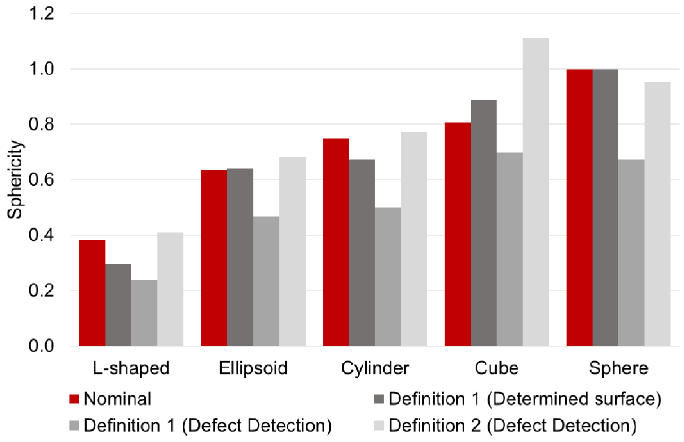

Figure 6.33: Comparison between nominal and measured sphericity of 5 pores with -different shapes.

6.6 Conclusions

In this Chapter a collaborative work with the University of Twente, Netherland, is presented. Ti6Al4V tensile specimens made by SLM were produced in order to compare different porosity testing methods such as X-ray CT, Archimedes method, pycnometry and destructive optical measurements. Gas pycnometry proved not to be accurate enough for testing parts with porosity percentages lower than 0.5%. Archimedes results are instead comparable with CT results, although CT predicts systematically higher relative density values (0.2-0.4%). These systematic deviations can be attributed to the presence of entrapped unmelted powder residue and to intrinsic limits of both methods. On one side, the nominal material density, used as reference for Archimedes' relative density evaluation, cannot be considered reliable, especially for non-homogeneous parts. On the other side, CT measurements can be influenced by image artefacts due to the interaction between X-rays and material, by the resolution and by the thresholding procedure. The comparison between CT and microscopic analysis of cross-sections resulted in a systematic difference as well. In particular, results by microscopic analysis are very close to the CMM results, while CT always measured smaller areas. CT is influenced by the above-cited factors, while micrographs can be affected by light and focus settings, stitching operations, thresholding and binarization. A systematically lower area measured by CT post-cut with respect to CT pre-cut can be observed with regard to the cut-section. Possible causes were identified in (i) deformations due to cutting/polishing operations and (ii) presence of entrapped unmolten powder residue that may fall out during the cutting. Finally, the accuracy of CT assessment of pore sphericity was investigated showing that a systematic error of -30% is obtained by the Defect Detection module of the used software (VG Studio Max). The main cause was determined to be the accuracy limited to the voxel size which leads to big errors especially when measuring pores surface. Another definition was applied and simulation analyses proved that an improved accuracy can be obtained using this definition.

Chapter 7

Wear evaluation of polymeric prosthetic components

This Chapter presents an experimental research work done in collaboration with the "Istituto Ortopedico Rizzoli" (IOR), orthopedic institute in Bologna, Italy. The main objective was to develop a CT-based method for wear evaluation of polyethilene's hip joint prosthetic components.

7.1 Background

The hip joint is made up of two major parts: the hip socket (acetabulum) and the beginning part of femur, allowing the joint to move smoothly in multiple directions. Total hip arthroplasty (THA) is surgery to replace all or part of the hip joint with an artificial joint, called prosthesis (see Figure 7.1). The artificial hip joint has 4 parts:

- A socket that replaces the old hip socket, usually made of metal.
- An insert that fits inside the socket to allow the hip to move smoothly. It is usually plastic, but can be also ceramic or metal.
- A metal or ceramic ball that will replace the round head of femur.
- A metal stem that is attached to the shaft of the bone.

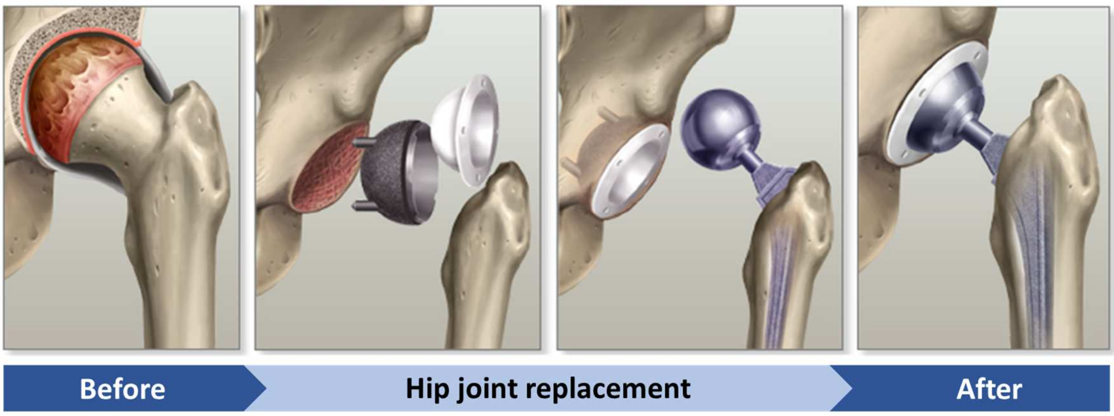

Figure 7.1: Schematic representation of hip joint replacement: a metal ball and stem are inserted in the femur and a plastic socket is placed in the enlarged pelvis cup [adapted from 114] .

Total hip arthroplasty has completely revolutionized the nature in which the arthritic hip is treated, and is considered to be one of the most successful orthopedic interventions of its generation [115]. For patients with hip pain due to a variety of conditions, THA can relieve pain, can restore function, and can improve quality of life. As the number of successful operations has increased, the goal of developing alternate bearing surfaces has been to create a joint with decreased friction and wear rates but with increased strength. Moreover, techniques have become standardized and the average age of those receiving hip replacements has reduced. However, higher failure rates in young patients justify plenty of caution in spite of significant improvements in the quality of bearing surfaces. Since ideal bearing surfaces for THA are still being continuously sought [116], the search for an ideal bearing surface, which is important for the longevity of THA, is receiving more attention: the bearing surface should have superior wear characteristics and should be durable, bioinert, cost-effective, and easy to implant. Ultra-high molecular weight polyethylene (UHMWPE) is a unique polymer with outstanding physical and mechanical properties. Most notable are its chemical inertness, lubricity, impact resistance, and abrasion resistance. Thanks to these characteristics, since 1962, UHMWPE has been used in orthopedics as a bearing material in artificial joints. However, although UHMWPE has a good wear behavior with respect to other polymeric materials (see Figure 7.2), UHMWPE implants have only a finite lifetime: wear and damage of the UHMWPE components is one of the factors limiting implant longevity [117]. In in vitro research studies, strong efforts have been made to improve the design, the material properties, and the method to improve the wear measurements [118-121].

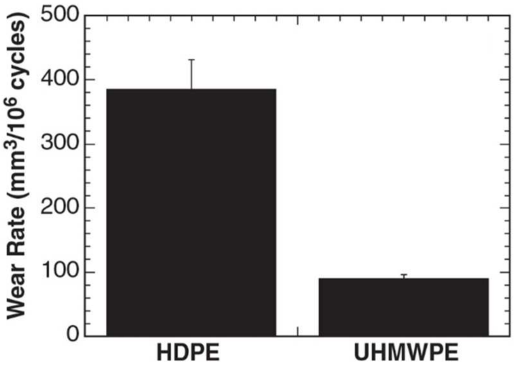

Figure 7.2: Comparison of wear rates of HDPE and UHMWPE in a multidirectional hip simulator [117].

At the state of the art, wear of hip joints prosthetic components can be evaluated by gravimetric method and volumetric method [122]. The former method is the standard measurement practice adopted by orthopedic industry: using a high-resolution microbalance the component weight is measured by following the procedure commanded by ISO 14242-2:2000 [123] before and after the wear test performed in accordance with ISO 14242-1:2014 [124]. The weight loss is then measured as the difference of the two measurements. On one side this method has proven to be sufficiently accurate to globally quantify the worn material; on the other side, it presents important limitations: it cannot provide information about the local distribution of wear over the worn surface and damages not involving material loss as possible plastic deformations cannot be assessed. The volumetric method based on tactile coordinate measuring machines (CMMs) is an alternative to the gravimetric method, allowed by ISO 14242-2:2000 [123]. This method has the advantage of enabling also accurate location and assessment of wear, besides quantification of wear volume. Moreover, Carmignato et al. [125] established an approach for uncertainty determination and validation of CMM measurement method in comparison with the gravimetric method. However, as a relevant drawback, tactile CMMs are not suitable for measuring polymeric prosthetic components. In fact, possible damages and unwanted deformations can be caused to the specimen by clamping and probing forces, hence increasing the measurement uncertainty [126].

More recently, CT has been used for wear evaluation of prosthetic components thanks to the capability of obtaining a three-dimensional (3D) model of the entire scanned object geometry with the possibility of conducting measurements in a non-destructive and non-contact way. Not only CT allows evaluating both global wear volume and local wear distribution and deformations but, differently from contact CMMs, it can also be considered particularly suited for analyzing polymeric components since it does not induce any damage to the component [127]. However, although CT has emerged as metrological instrument allowing high-accuracy measurements, as long as the measurement uncertainty is not determined the actual reliability of the achievable results cannot be known for the specific measurement task. In particular, traceability for volume measurements is a relevant issue to deal with. In fact, the volume of polymeric prosthetic components is difficult to be measured in an accurate way with well-established measuring methods. For example, contact CMMs cannot be used for the reasons explained above; laser scanning could be problematic for possible reflections and/or absorption due to the material properties and Archimedes method can lead to inaccurate results because of possible liquid absorption.

The research study presented in this Chapter is a collaboration with the Istituto Ortopedico Rizzoli (IOR), Bologna, Italy, focused on wear evaluation of different polyethylene's acetabular cups (vitamin E-stabilized XLPE, XLPE, and standard UHMWPE) by microCT including volumetric wear and wear surface distribution. Investigations are aimed at validating the CT-based method through comparison with the gravimetric method.

7.2 Materials and methods

Components used in this work were 9 acetabular cups made by three different types of UHMWPE (see dimensions in Figure 7.3 and real components in Figure 7.4) most used in the orthopaedic field nowadays [128]: vitamin E-stabilized cross-linked PE (hereinafter called XLPE_VE), cross-linked PE (hereinafter called XLPE), and standard bars made of GUR 1020 (Polymax, Adler, Milan, Italy). XLPE acetabular cups were obtained from a cylindrical bar, firstly γ-ray irradiated to 75 KGy (±10%), then thermally treated at 150 °C, in order to remove free radicals formed during irradiation. After these treatments, the cups were machined to their final shape. Similarly, Vitamin E-containing (0,1%), XLPE acetabular cups were machined from a Vitamin E-blended UHMWPE bar (Polymax, Adler, Milan, Italy), after electron beam irradiation to 75 KGy (±10%), followed by a thermal treatment at 150 °C under nitrogen for 12 hours. All polyethylene acetabular cups were pre-soaked for four weeks prior the wear tests.

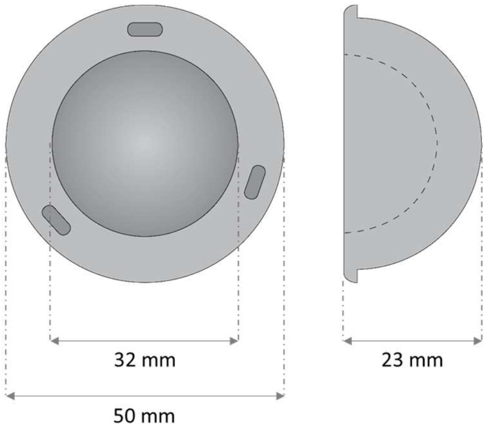

Figure 7.3: Nominal dimensions of hip joint components investigated in this work.

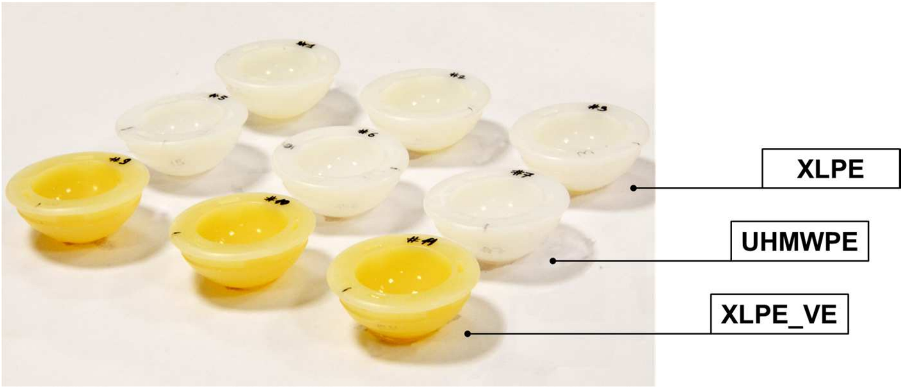

Figure 7.4: Nine hip joint components made by three different types of polyethylene used for experimental tests.

Wear test was performed using a 12-station hip joint simulator (IORSynthe, Bologna, Italy). The simulator utilized hydraulic actuators to apply the cyclic vertical compressive loads (oscillating between 102 and 3000 N applied perpendicular to the acetabular components as recommend by the International ISO 14242). The lubricant used was 25% (v/v) new born calf serum balanced with distilled water, with 0.2% sodium azide in order to retard bacterial growth and 20 mM EDTA (ethylene-diamine-tetracetic acid) to minimize precipitation of calcium phosphate. All the procedures to clean and weight the components were performed following international guidelines (ISO 14242-2 [123]) and consolidated internal IOR protocols [129, 130].

Each cup was measured before and after the wear test by two methods: X-ray computed tomography and gravimetric method. The gravimetric method is the so-called ‘golden standard’ which consisted of measuring the weight loss using a microbalance (SARTORIUS CUBIS MSE 225 S-000-DU, Germany) with resolution of 0.01 mg, by averaging the results of three repetitions conducted for each component. Tomographic measurements were conducted using the system described in Section 1.4.1. The optimized CT scanning parameters used in this work are reported in Table 7.1. To minimize the actual focal spot size on the X-ray target, an electron beam power of 9 watts was selected out of possible 225 watts. An appropriated stand was adapted to the prosthesis geometry. The positioning was studied in order to minimize the Feldkamp effect (see Section 3.3), typical of cone beam CT systems, and to localize the resulting artifacts over regions not interested by wear (Figure 7.5). The stand was made by polystyrene, since it is low absorbing for the radiation and does not compromise the measurement.

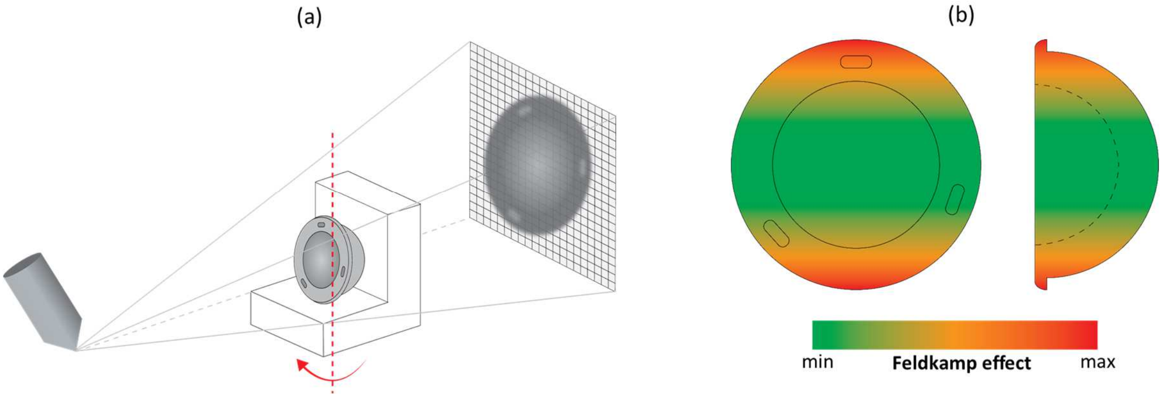

Figure 7.5: Schematic representation of one hip joint component as it was positioned during the CT acquisition (a). The stand is made by polystyrene. This placement allows the Feldkamp artifact to be localized in regions not affected by wear (b).

Since the acetabular cups were retained in an appropriate liquid, they were carefully cleaned, dried and let stabilize inside the CT cabinet for 100 minutes before each CT scan. The X-ray 2D projections obtained from the acquisition step were then used in the reconstruction step for obtaining a 3D volume of the investigated components by means of a filtered back-projection algorithm. Adaptive methods were applied to determine the surface location of the reconstructed model with high accuracy. The commercial elaboration software VGStudio Max was used to: (i) measure the volumetric wear calculated as the difference in volume between the 3D models obtained before and after the wear test and (ii) create deviation maps showing local wear and deformations as they are distributed over the worn surfaces (see example in Figure 7.6).

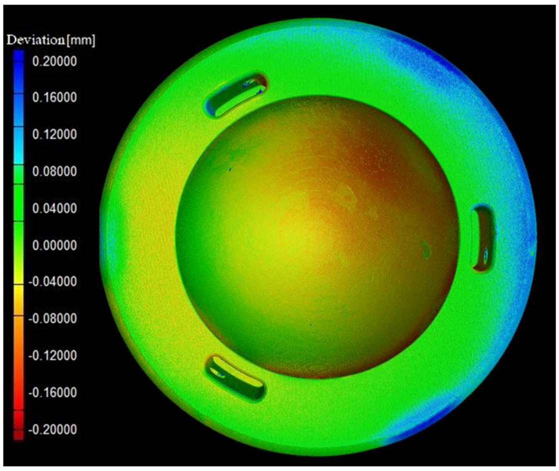

Figure 7.6: Wear map of one of the nine acetabular components investigated in this work. Wear can be appreciated over the internal calotte surface (yellow-red colored), while deformations are localized over the external circular crown (blue colored) most probably due to the wear test set-up.

Table 7.1: CT scanning parameters optimized for UHMWPE acetabular cups.

Voltage	194 kV
Current	46 µA
Exposure time	1415 ms
Projections	1500
Scanning time	35 min
Voxel size	31 µm
Physical filtering	No

The metrological behavior of the CT system was periodically verified using calibrated objects, in order to check and correct measurement errors, including scale errors. In fact, it is well known that temperature control and metrological performance verification, as well as systematic errors correction, are necessary to reduce measurement errors and to allow metrological use of CT systems. In this work, a specific procedure for the scale correction of the CT system was implemented during experimental tests before each batch of scans in order to check and fix possible scale errors due to uncorrected source-to-detector and source-to-object distances.

7.3 Results

7.3.1 Volumetric wear assessment

The volume of a CT reconstructed object can be easily quantified as the product of number of voxels contained within the determined surface and the known volume of a single voxel. The number of voxels is not necessarily represented by an integer, since intra-voxel interpolation is used for edge detection to cope with partial volume effect (see Figure 2.15). The volumetric wear was assessed by CT scanning each component before and after the wear test, and subtracting the respective obtained results. This type of evaluation does not need alignment operations to be done, so every volume can be processed separately. The volumetric wear of the nine tested acetabular cups measured by micro-CT are listed in Table 7.2 together with gravimetric results, after conversion to milligrams (mg) using constant value for UHMWPE density (0.945 mg/mm^3). Both methods show that the XLPE's acetabular cups are the less affected by wear, while UHMWPE's are the most affected, when tested at 2 millions of cycles. XLPE_VE's components have a wear behavior similar to standard polyethylene's.

Table 7.2: Gravimetric and CT wear measurement results for specimens tested at 2 Mc.

	Volumetric wear (mg)		
Acetabular cup	**CT**	**Gravimetric**	**Difference**
UHMWPE_1	23.26	20-37	2.89
UHMWPE _2	21.38	23.06	-1.69
UHMWPE _3	19.24	17.77	1.47
XLPE_1	2,97	5.40	-2.42
XLPE_2	4,91	6.86	-1.95
XLPE_3	9,83	9.51	0.32
XLPE_VE_1	21.89	23.94	-2.06
XLPE_VE_2	13.79	16.43	-2.64
XLPE_VE_3	15.04	18.41	-3.37

7.3.2 Wear local distribution analysis

The capability of acquiring a wear map is one of the main advantages of the CT method for this specific application. Prosthetic components scanned after the wear test must be aligned to their respective component scanned before the wear test. The alignment procedure is required to be as accurate as possible to obtain reliable wear maps. However, the optimal alignment is difficult to be achieved, due to wear and possible deformations which can modify the surface topography. In this work, a two-step alignment procedure was applied:

(i) Preliminary rough alignment: registration of each single component according to a primary, a secondary and a tertiary datum reference. For each step, a geometrical element was defined on unworn and non-deformed surface regions and the axis/origin coordinate specified by that geometrical element was chosen.

(ii) Fine adjustment of the previous alignment based on the current position of the objects (i.e. best-fit refinement constrained to the preliminary alignment, allowed by VGStudio MAX).

After the alignment operations, local wear distribution mapping on internal calottes of all the acetabular cups was obtained and is shown in Figure 7.7. The wear maps show the distribution of wear on the internal calotte of each acetabular cup, confirming the outcomes of the volumetric measurement. The wear is localized to specific areas that are strictly dependent on the load configuration and positioning adopted during the wear test.

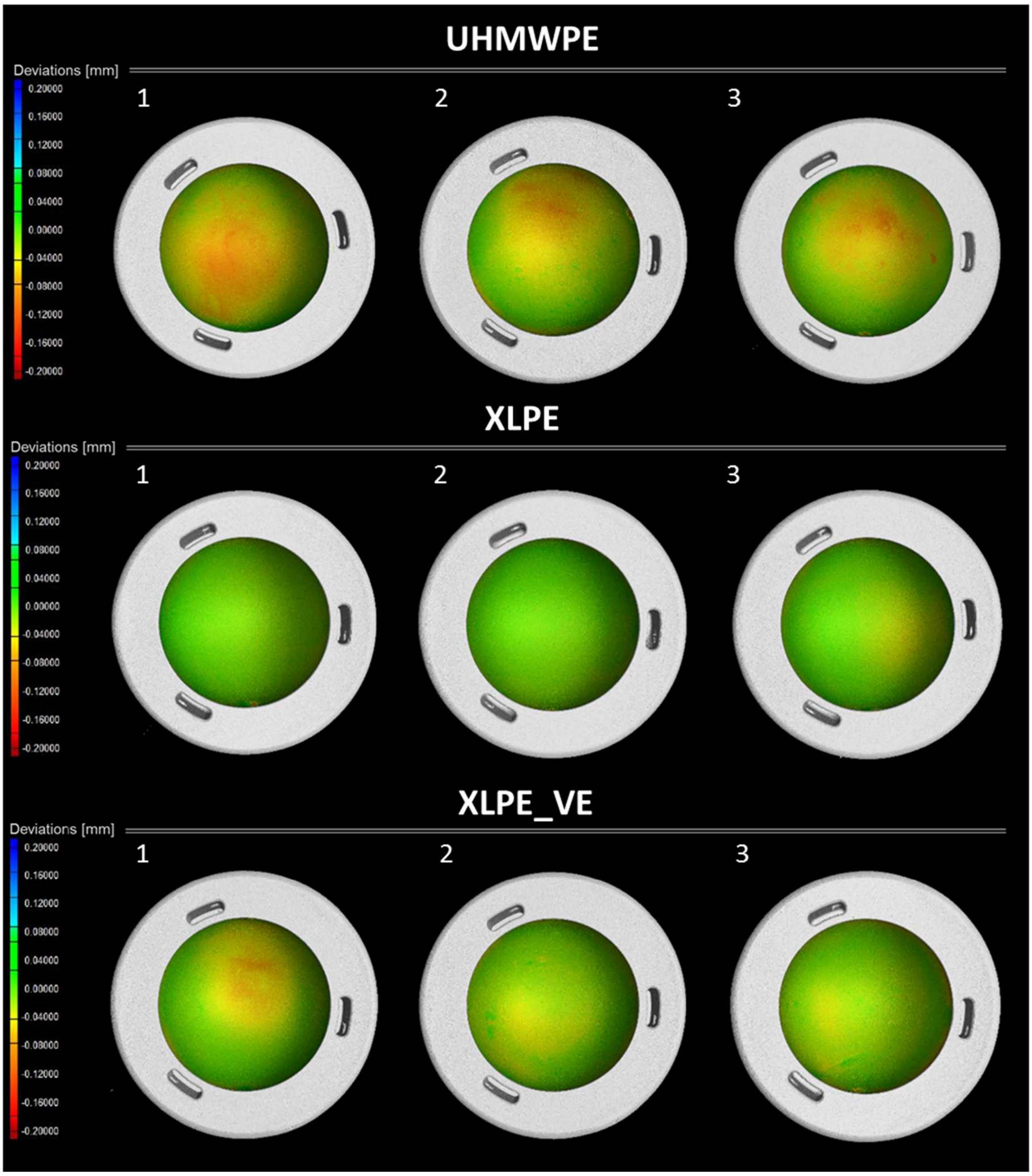

Figure 7.7: CT wear maps of nine hip joint components made by three different types of polyethylene. Every color corresponds to a specific deviation (in mm) due to wear.

7.4 Validation of the CT-based method

The comparison between volumetric wear measurements obtained by CT and by the well-established gravimetric method was investigated for validating the new tomographic measurement method. For a combined graphical/statistical interpretation of the comparison of micro-CT and gravimetric methods, two common approaches were chosen: a scatter plot with correlation and regression analysis and a difference plot (Bland-Altman plot [131]) with 95% limits of agreement. Linear regression quantifies goodness of fit with the coefficient of determination (R^2). Although the correlation quantifies if two variables are related, a high correlation does not necessary mean a good agreement between the two methods. Thus, the Bland-Altman (B&A) plot was used to describe the agreement between the two quantitative measurements. It consists of a diagram in which the difference of the two measurements is plotted against the mean of the two measurements. To check the assumption of normality of distribution of differences, a Shapiro-Wilk test [132] was done (normality occurs when $p > 0.05$).

Figure 7.8-a compares CT results with gravimetric ones, showing a good linear correlation with coefficient of determination, R^2, equal to 0.9219. The Bland-Altman plot illustrated in Figure 7.8-b demonstrates the agreement between the two measuring techniques. Differences were calculated as CT volumetric wear minus gravimetric equivalent volumetric wear. The mean difference (bias) was found to be -1 mg with ±1.96 S.D. (3.1—5.2 mg), which is related to a confidence interval of 95%. A Shapiro-Wilk test ($p = 0.14$) confirmed the normality of distribution of differences.

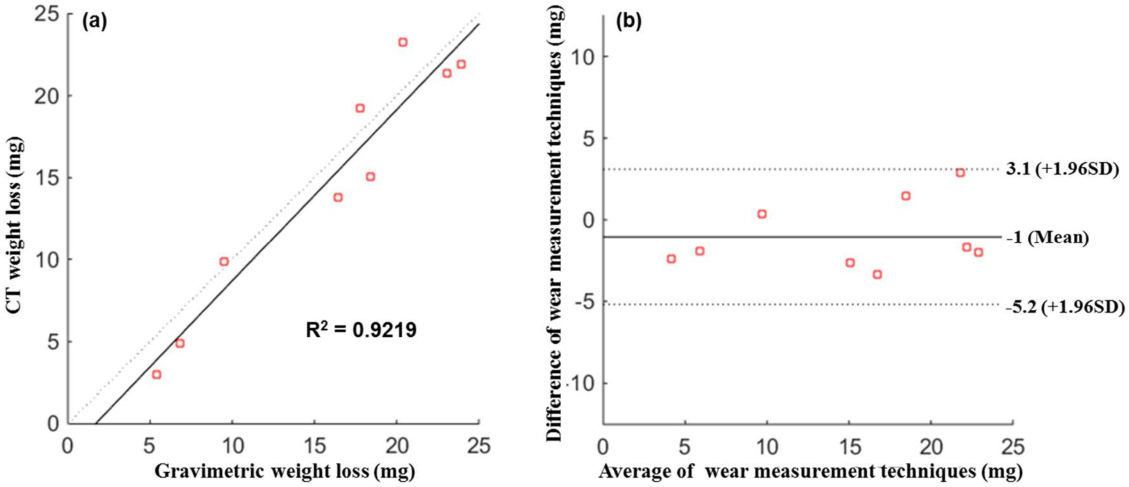

Figure 7.8: (a) Linear regression analysis between volumetric CT and gravimetric wear evaluations; (b) Bland-Altman plot to evaluate the consistency between CT and gravimetric wear.

7.5 Discussion and conclusions

This Chapter was focused on the validation of a CT-based method for volumetric wear measurement and evaluation of wear distribution over the worn surface of polymeric hip prosthetic components. Experimental investigations were conducted on 9 different polyethylene's acetabular cups (vitamin E-stabilized XLPE, XLPE, and standard UHMWPE): each component was measured before and after the in vitro wear test by CT and gravimetric method. The CT-based method was validated through comparison with gravimetric method: the two methods were found to be correlated and in agreement with a mean difference in the order of 11%. The highest percentage difference (≅ 45%) was registered for the least worn component (XLPE_1). The differences are not only due to the uncertainty of CT wear measurements, but also to the uncertainty of the density value. Furthermore, although the gravimetric method is currently considered the gold standard, it is also unavoidably affected by uncertainties of measurements.

For a good metrological practice, future works should focus on the determination of CT wear measurement uncertainty and the extension of the approach here presented to other cases, e.g. wear evaluation of knee polymeric joints.

Chapter 8

Conclusions

This Chapter contains the main conclusions and final remarks about the PhD project

This thesis presented the main outcomes of the PhD project entitled: “X-ray computed tomography for coordinate metrology and industrial applications”. A brief introduction of the project is provided in Chapter 1. X-ray computed tomography was described in detail in Chapter 2, starting from the historical background. Before being employed in the industrial environment, CT was used for medical applications. Then, the tomographic technology was adapted to perform non-destructive material analyses of industrial objects. More recently, CT has emerged as advanced tool for dimensional metrology. The state of the art was illustrated in Chapter 2 with main focus on industrial CT systems used in the field of coordinate metrology. In particular, the most typical characteristics and setups were presented, followed by a description of the CT measurement procedure and by an overview of industrial case studies, most of which were personally addressed during the PhD period. The main advantages and limitations of CT were pointed out as well. CT has become an attractive alternative to other well-established coordinate measuring systems thanks to several unique capabilities. It allows obtaining a complete three-dimensional model of the scanned workpiece with high information density in a relative short time. Moreover, CT gives the opportunity of performing non-destructive and non-contact measurements of both outer and inner features and geometries. However, this technology has not already gained a wide acceptance in industry due to several drawbacks, such as the lack of international standard procedures for acceptance test and performance verification and the challenge represented by the determination of task-specific uncertainty. Chapter 3 described the procedures that are currently used for metrological performance verification and measurement uncertainty determination. Most of them are provided by the German guideline VDI/VDE 2617-13. This guideline will be the base for the development of the future ISO standard for CT. The ISO working group responsible for the standard development is still discussing about several aspects. Two of these aspects were addressed during the PhD project. In particular, Chapter 4 described the experimental study about material influence on length measurement errors, which was part of a test survey organized by the ISO working group. Tests using an aluminium hole plate were recommended, since it allows measuring both uni-directional and bi-directional lengths with significant material effect. A ruby ball plate was also investigated as reference object with negligible material influence and dimensions similar to the hole plate. The outcomes of these tests, together with results obtained by the other research institutions involved, were useful to establish the use of hole plate as reference object for length measurement errors evaluation, with no need to complete the analysis with other tests and/or reference objects. Chapter 5 provided a description of experimental investigations focused on the evaluation of the image quality of 2D projections acquired by CT and on metrological structural resolution. A specific method was designed in collaboration with the National Physical Laboratory (NPL), UK, to measure the focal spot drift, considered on of the main influences affecting the image quality. A maximum drift of 0.2 pixels was observed for a well-behaving system and higher then 1 pixel for a system facing instability issues (e.g. overheating of the X-ray tube). Warming-up the system can further decrease the drift in the first case, while can even increase the focal spot movement in the second case. Moreover, a new method was developed to assess the actual focal spot size through comparison between actual and simulated radiographs of objects like a tungsten cutting edge and the JIMA test chart. Further works are needed in order to improve the match between simulated and experimental projections. The 'Hourglass' method, developed by the University of Padova, was used to evaluate the metrological structural resolution. The methods was improved with a new measurement strategy and by applying an adapted version of the definition provided by the VDI/VDE 2617-13: "the metrological structural resolution is the smallest distance that can still be measured within an error to be specified". The concept of this method was then compared with concepts of other proposed methods and the main influence quantities were identified and evaluated by experimental and/or simulation analyses.

As said above, one of the main limits of CT is the complex establishment of metrological traceability due to difficulties in evaluating task-specific uncertainty and in determining metrological performances of CT systems. On the other side, CT is a very attractive solution for several industrial fields, but the accuracy of the obtained results has to be assessed carefully. In this context, the comparability of CT with other well-established measuring methods becomes crucial. In this project, two applications involving the comparison of CT with other methods were addressed. Chapter 6 have dealt with an experimental study on the accuracy of CT porosity analysis for metal additive manufactured parts. Ti6Al4V specimens made by SLM were produced by the University of Twente, Netherland. CT porosity analysis was compared with Archimedes method and with gas pycnometry. The pycnometer was found to be not sufficiently accurate for the small porosity content of the analysed specimens, while Archimedes and CT results were found to follow a similar trend but with a systematic difference. A systematic difference was observed also when comparing CT with microscopic analysis of cross-sections. For this comparison, a new method involving pore areas calibration by multisensory CMM was developed. The causes of systematic differences were identified, investigated and discussed in Chapter 6. Chapter 7 presented another case study. A CT-based method for wear evaluation of polymeric hip prosthetic components was developed and validated through comparison with the gravimetric method. Experimental investigations were conducted on 9 different polyethylene's acetabular cups, each measured before and after the in vitro wear tests by CT and gravimetric method. A good agreement between CT and gravimetric method was demonstrated.

References

[1] http://www.nikonmetrology.com/en_EU/Products/X-ray-and-CT-Inspection/Metrology-CT/MCT225-for-Metrology-CT-Absolute-accuracy-for-inside-geometry (Accessed 15-10-2016).

[2] http://www.volumegraphics.com/ (Accessed 15-10-2016).

[3] http://www.iis.fraunhofer.de/en/ff/zfp/leist/scorpiusxlab.html (Accessed 15-10-2016).

[4] Buzug T.M. (2008). Computed tomography: from photon statistics to modern cone-beam CT. Springer, Berlin.

[5] Carroll Q.B. (2011). Radiography in the digital age. Charles C Thomas, Springfield (IL)

[6] Hsieh, J., (2009). Computed Tomography: Principles, Design, Artifacts, and Recent Advances, Second Edition (SPIE Press Book) ISBN: 9780819475336.

[7] Hounseld, G.N., (1973). Computerized transverse axial scanning (tomography): Part1. description of system. British Journal of Radiology, 46:1016 1022.

[8] Weckenmann A., Kramer P. (2013). Computed tomography in quality control: chances and challenge. Proc. IMechE Part.B: J Engineering Manufacture Vol. 227, Issue 5, pp 634-642.

[9] Oldendorf, W. H., (1978). The quest for an image of brain: a brief historical and technical review of brain imaging techniques. Neurology, 517-33

[10] Bartsher M., Hilpert U., Hartig F., Neuschaefer-Rube U., Goebbels J., Staude A. (2008). Industrial computed tomography, an emerging coordinate measurement technology with high potential. Proc. Of NCSL International Workshop and Symposium.

[11] Mitchell K. W. (1989). A Generalized approach to wall thickness measurements in CT images. Topical Proc. Industrial Computerized Tomography, ASNT, 120-124. ISNB 0-931403-89-8.

[12] Kruth J.-P., Bartscher M., Carmignato S., Schmitt R., De Chiffre L., Weckenmann A. (2011). Computed tomography for dimensional metrology, CIRP Annals - Manufacturing Technology 60(2) pp. 821–842, doi:10.1016 / j.cirp.2011.05.006.

[13] Ketcham R. A., Carlson W. D. (2001). Acquisition, optimization and interpretation of X-ray computedtomographic imagery: Applications to the geosciences, Computers & Geosciences 27 pp. 381–400.

[14] Kerckhofs G., Schrooten J., Van Cleynenbreugel T., Lomov S. V., Wevers M. (2008). Validation of X-ray Micro-CT as an imaging tool for porous structures. Review of scientific instruments 79(1): 1-9. Article number 013711

[15] Kerckhofs G., Schrooten J., Wevers M. et al. (2006). Standardisation and validation of micro-CT for the morphological characterization of porous structures. Proc. 9th Eur. Conf. Non-destructive testing (ECNDT), Berlin, Germany, 25-29 September, 1-12.

[16] Kak A. C., Slaney M. (1988). Principles of computerized tomographic imaging. IEEE Press, New York.

[17] ASTM E 1441-11 - Standard Guide for Computed Tomography (CT) Imaging, ASTM International, United States.

[18] Cendre E., Duvauchelle P., Peix G., Buffiere J. Y., Babot D. (1999). Conception of a high resolution X-Ray Computed Tomography device; Application to damage initiation imaging inside materials, 1st World congress on industrial process tomography, Buxton, Grater Manchester.

[19] Feldkamp L. A., Davis L. C., Kress J. W. (1984). Practical cone-beam algorithm. Journal Optical Society of America, Vol. 1(6), pp. 612-619.

[20] Smith S. W. (1999). The Scientist and Engineer's guide to digital signal processing. California Technical Publishing (2nd edition).

[21] Otsu N. (1979). A threshold selection method from grey level histograms, IEEE Transactions on Systems, Man, and Cybernetics 9 (1) pp. 62–66.

[22] Carmignato S., Dreossi D., Mancini L., Marinello F., Tromba G., Savio E. (2009). Testing of x-ray microtomography system using a traceable geometrical standard, IOP Publishing- Meas. Sci. Technol. 20, 084021

[23] Leonard F., Brown S. B., Withers P. J., Mummery P. M., McCarthy M. B. (2014). A new method of performance verification for x-ray computed tomography measurements. Meas. Sci. Technol. 25, 10pp. doi:10.1088/0957-0233/25/6/065401

[24] De Chiffre L., Carmignato S., Kruth J. P., Schmitt R., Weckenmann A. (2014). Industrial applications of computed tomography. CIRP Annals - Manufacturing Technology, vol. 63, pp. 655 – 667.

[25] Savio, E., De Chiffre, L., & Schmitt, R. (2007). Metrology of freeform shaped parts. CIRP Annals-Manufacturing Technology, 56(2), 810-835.

[26] Brunke O., Hansen F., Stuke I., Butz F. F. (2012). A new concept for high speed atline and inlineCT for up to 100% mass production process control. 18 th World conference of nondestructive testing, Durban, South Africa.

[27] Kersting P., Carmignato S., Odendahl S., Zanini F., Siebrecht T., Krebs E. (2015). Analysing machining errors resulting from a micromilling process using CT measurement and process simulation. Proceedings of the 4M/ICOMM2015 Conference. Milan, Italy, 31 March - 2 April 2015. p. 130-133.

[28] Flisch A., Wirth J., Zanini R., Breitenstein M., Rudin A., Wendt F., Mnich F., Golz R. (1999). Industrial computed tomography in reverse engineering applications. DGZfP-Proceedings BB 67-CD.

[29] ISO 9001:2008. Quality management systems - Requirements, International Organization for Standardization, Geneva.

[30] ISO/IEC 17025:2005. General requirements for the competence of testing and calibration laboratories. International Organization for Standardization, Geneva.

[31] International vocabulary of metrology - basic and general concepts and associated terms VIM, ISO / IEC Guide 99 (2007).

[32] ISO 10360-2 - Geometrical product specifications (GPS) – Acceptance and reverification tests for coordinate measuring machines (CMM) – Part 2: CMMs used for measuring linear dimensions, International Organization for Standardization, Geneva (2009).

[33] VDI/VDE 2617-13 - Accuracy of coordinate measuring machines - Characteristics and their testing - Guideline for the application of DIN EN ISO 10360 for coordinate measuring machines with CT-sensors, VDI / VDE 2630-1.3 - Computed tomography in dimensional measurement - Guideline for the application of DIN EN ISO 10360 for coordinate measuring machines with CT-sensors, VDI / VDE Society for Metrology and Automation Engineering (GMA), Duesseldorf (2011).

[34] Borges de Oliveira F., Bartscher M., Neuschaefer-Rube U. (2015). Analysis of combined probing measurement error and length measurement error test for acceptance testing in dimensional computed tomography. Proc. of DIR 2015 in NDT.net

[35] ISO 10360-5 - Geometrical product specifications (GPS) -- Acceptance and reverification tests for coordinate measuring machines (CMM) -- Part 5: CMMs using single and multiple stylus contacting probing systems (2010).

[36] ISO/TS 23165 - Geometrical product specifications (GPS) -- Guidelines for the evaluation of coordinate measuring machine (CMM) test uncertainty (2006).

[37] ISO 14253-1 - Geometrical Product Specifications (GPS) – Inspection by measurement of workpieces and measuring equipment – Part 1: Decision rules

for proving conformance or non-conformance with specifications, International Organization for Standardization, Geneva (1998).

[38] JCGM 100:2008, Evaluation of measurement data—guide to the expression of uncertainty in measurement (GUM 1995 with minor corrections), JCGM, 2008.

[39] Wilhelm R. G., Hocken R., Schwenke H. (2001). Task specific uncertainty in coordinate measurement, CIRP Annals 50(2): 553-563.

[40] Bartscher M., Neukamm M., Hilpert U., Neuschaefer-Rube U., Härtig F., Kniel K., Ehrig K., Staude A., Goebbels J.. (2010). Achieving traceability of industrial computed tomography, Key Engineering Materials 437 pp. 79–83.

[41] ISO 15530-3 - Geometrical product specifications (GPS) – Coordinate measuring machines (CMM): Technique for determining the uncertainty of measurement – Part 3: Use of calibrated workpieces or measurement standards, International Organization for Standardization, Geneva (2011).

[42] Dewulf W., Kiekens K., Tan Y., Welkenhuyzen F., Kruth J.-P. (2013). Uncertainty determination and quantification for dimensional measurements with industrial computed tomography. CIRP Annals, 62/1:535–538.

[43] Carmignato S. (2012) Accuracy of industrial computed tomography measurements: Experi-mental results from an international comparison. CIRP Annals – Manufacturing Technology, 61-1: 491-494.

[44] ISO/IEC 17043:2010, Conformity assessment—general requirements for proficiency testing, ISO, Geneva.

[45] Angel J., De Chiffre L. (2014). Comparison on Computed Tomography using industrial items. CIRP Annals 63: 473–476.

[46] Stolfi A., De Chiffre L. (2016). Selection of items for “InteraqCT Comparison on Assemblies”, proc. of iCT 2016 in NDT.net.

[47] VDI/VDE 2630-1.2 - Computed tomography in dimensional measurement - Influencing variables on measurement results and recommendations for

computed tomography dimensional measurements, VDI/VDE Society for Metrology and Automation Engineering (GMA), Duesseldorf (2010).

[48] Müller P. (2013). Coordinate Metrology by Traceable Computed Tomography. PhD thesis. Department of Mechanical Engineering, Technical University of Denmark, Lyngby, Denmark.

[49] Dewulf W., Tan Y., Kiekens K. (2012). Sense and non sense of beam hardening correction in CT metrology. CIRP Annals – Manufacturing technology 61, pp 495-498

[50] Xue L., Suzuki H., Ohtake Y., Fujimoto H., Abe M., Sato O., Takatsuji T. (2015). Numerical analysis of the Feldkamp-Davis-Kress effect on industrial x-ray computed tomography for dimensional metrology. Journal of computing and information science in engineering, Vol.15.

[51] Heinzl C. (2008). "Analysis and visualization of industrial CT data", Ph.D. Thesis, supervised by E. Groeller, Vienna University of Technology, Institute of computer graphics and algorithms.

[52] Bartscher M., Hilpert U., Goebbels J., Weidemann G. (2007). Enhancement and proof of accuracy of industrial computed tomography (CT) measurements, CIRP Annals – Manufacturing Technology 56 (1) (2007) pp. 495–498.

[53] Bartscher M, Hilpert U, Härtig F, Neuschaefer-Rube U, Goebbels J, Staude A (2008). Industrial computed tomography, an emerging coordinate measurement technology with high potentials, Proc. of NCSL 2008 International workshop & symposium.

[54] Kiekens K., Welkenhuyzen F., Tan Y., Bleys Ph., Voet A., Kruth J.-P., Dewulf W.. (2011). A test object with parallel grooves for calibration and accuracy assessment of industrial computed tomography (CT) metrology, Measuring Science and Technology 22, 115502.

[55] Bartscher, M., Ehrig, K., Staude, A., Goebbels, J., Neuschaefer-Rube, U. (2011). Application of an industrial CT reference standard for cast freeform shaped workpieces. DIR Berlin.

[56] Cho Y., Moseley D. J., Siewerdsen J. H., Jaffray D. A. (2005). Accurate technique for complete geometric calibration of cone-beam computed tomography systems Med. Phys. 32 968–83.

[57] Hermanek P., Carmignato S. (2016). Reference object for evaluating the accuracy of porosity measurements by X-ray computed tomography. Case Studies in Nondestructive Testing and Evaluation.

[58] Muller P., Hiller J., Dai Y., Andreasen J. L., Hansen H. N., De Chiffre L. (2015). Quantitative analysis of scaling error compensation methods in dimensional X-ray computed tomography. CIRP Annals – Manufacturing Science and technology, Vol.10, pp 68-76.

[59] Bartscher M. (2013). ISO TC 213 WG 10 experimental study on material influence in dimensional computed tomography (CT), information on the test study. Physiklisch-Technische Bundesanstalt, Germany, 2013-10-28.

[60] Sato O. (2013). Instruction of hole plate measurement using the supplied templates. NMIJ, Japan, 2013-10-10.

[61] Bartscher M., Illemann J., Neuschaefer-Rube U. (2016). ISO test survey on material influence in dimensional computed tomography. Case Stud Nondestruct Test Eval,

[62] Kalender W. A. (2006). Computed Tomography: Fundamentals, System Technology, Image Quality, Applications, 2nd Edition, Wiley-VCH (2006).

[63] Van De Casteele E. (2004). Model-based approach for beam hardening correction and resolution measurements in microtomography. PhD Thesis, Supervised by Dirk van Dyck e Erik Raman, Università Antwerpen.

[64] Hecht, E. (2002) Optics 4th Edition, Addison Wesley, ISBN 0-321-18878-0.

[65] Bartscher M., Bremer H., Birth T., Staude A., Ehrig K. (2012). The resolution of dimensional CT - An edge-based analysis, Proceedings iCT, Wels, Austria.

[66] Carmignato S., Rampazzo P., Balcon M., Parisatto M. (2013). Practical method for determining the metrological structure resolution of dimensional CT. Proc. of the 13th euspen international conference, Berlin, Germany.

[67] Müller P., Hiller J., Cantatore A., Bartscher M., De Chiffre L. (2012). Investigation on the influence of image quality in X-ray CT metrology. Proc. of the Conference on Industrial Computed Tomography (ICT); pp. 229–238.

[68] Yang X., Meng Y., Luo Q., Gong H.. (2010). High resolution in vivo micro-CT with flat panel detector based on amorphous silicon, Journal of X-Ray Science and Technology, Vol 18/4, 381-392.

[69] ISO 15708-1:2002, Non destructive testing - Radiation methods - Computed tomography – Principles. ISO, Geneve, 2002.

[70] ISO 15708-2:2002, Non-destructive testing - Radiation methods - Computed tomography - Part 2: Examination practices, ISO Geneve 2002

[71] BS EN 16016-3:2011 Non destructive testing - Radiation method - Computed tomography Part 3: Operation and interpretation, British Standard

[72] Sun W., Brown S., Flay N., McCarthy M., McBride J. (2016). A reference sample for investigating the stability of the imaging system of x-ray computed tomography. Meas. Sci. Technol. Vol.27, 9 pp.

[73] Chaney E. L., Hendee W. R. (1974). Effects of x-ray tube current and voltage on effective focalspot size Med. Phys. 1 141–7.

[74] Flay N., Sun W., Brown S., Leach R., Blumensath T. (2015). Investigation of the focal spot drift in cone-beam industrial x-ray computed tomography Proc. of Digital Industrial Radiology and Computed Tomography (Ghent, Belgium).

[75] Hiller J., Maisl M., Reindl L. M. (2012). Physical characterization and performance evaluation of an X-ray micro-computed tomography system for

dimensional metrology applications Measurement Science and Technology 23, 085404.

[76] Vogeler F., Verheecke W., Voet A., Kruth J. (2011). Positional stability of 2D X-ray images for computer tomography International Symposium of Digital Industrial Radiology and Computed Temography (Proceedings) MO33.

[77] Fröba T., Steffen J. P. (2011). Assessing the effect of focal spot movement on the accuracy of CT results by using a simulation technique Website: - http://www.ndt.net/article/ctc2012/papers/253.pdf Accessed in March 2014.

[78] Canny, J. (1986). A computational approach to edge detection. IEEE Transactions on pattern analysis and machine intelligence, (6), 679-698.

[79] UNI EN 12543:2002. Characteristics of focal spots in industrial X-ray systems for use in non-destructive Testing. Parts 1 to 5. Ente Nazionale Italiano di Unificazione.

[80] ASTM E1165-12. Standard Test Method for Measurement of Focal Spots of Industrial X-Ray Tubes by Pinhole Imaging. ASTM International, West Conshohocken, PA.

[81] Bavendiek K., Ewert U., Riedo A., Heike U., Zscherpel U. (2012). New Measurement Methods of Focal Spot Size and Shape of X-ray Tubes. 18th World Conference on Nondestructive Testing. Durban, South Africa.

[82] Engelhardt M., Baumann J. (2006). Determination of size and intensity distribution of the focal spot of a microfocus X-ray tube using image processing. 9th European Conference on Non-Destructive Testing. Berlin, Germany. Th.2.5.4.

[83] Taubenreuther U. (2002). Korrektur Kalibrierverfahren für die Kegelstrahl (Mikro-CT), Dissertation, Friedrich-Alexander-Universität Erlangen-Nürnberg.

[84] Baumann J. (1984). Bestimmung des Fokusdurchmessers von Mikrofokus-Röntgenquellen mit Hilfe von Röntgen-Litographiemasken. Poster, DGZfP

Jahrestagung 1984, Deutsche Gesellschaft für zerstörungsfreie Prüfung (DGZfP), Essen.

[85] Jobst A., Kostka G. and Schmitt P. (2004). Neue Methode zur Charakterisierung von Brennflecken kleiner als 5 µm. DACH Jahrestagung 2004, Deutsche Gesellschaft für zerstörungsfreie Prüfung (DGZfP), Salzburg.

[86] http://www.jima.jp/content/pdf/catalog_rt_rc05_eng.pdf (Accessed 15-10-2016).

[87] Samei E., Flynn M. J., Reimann D. A. (1998). A method for measuring the presampled MTF of digital radiographic systems using an edge test device. Med. Phys. 25 (1), pp. 102-113.

[88] ASTM E1695-95:2013, Standard Test Method for Measurement of Computed Tomography (CT) System Performance, American Society for Testing and Materials, West Conshohocken, USA.

[89] Bartscher M., Sato O., Hartig F., Neuschaefer-Rube U. (2014). Current state of standardization in the field of dimensional computed tomography, Meas. Sci. Technol. Vol 25-56.

[90] http://www.qrm.de/content/pdf/QRM-MicroCT-Barpattern-Phantom.pdf (accessed 15-10-2016).

[91] Illemann J., Bartscher M., Jusko O., Hartig F., Neuschaefer-Rube U., Wendt K. (2014). Procedure and reference standard to determine the structural resolution in coordinate metrology Meas. Sci. Technol., 25.

[92] Flessner M., Vujaklija N., Helmecke E., Hausotte T. (2014). Determination of metrological structural resolution of a CT system using the frequency response on surface structures, Proceedings MacroScale, Vienna, Austria, 2014.

[93] Arenhart F. A., Nardelli V. C., Donatelli G. D. (2015). Characterization of the metrological structural resolution of CT systems using a multi-wave standard, XXI IMEKO World Congress, Prague, Czech Republic, 2015.

[94] Arenhart F. A., Baldo C. R., Fernandes T. L., Donatelli G D (2016). Experimental Investigation of the Influencing Factors on the Structural Resolution for Dimensional Measurements with CT Systems, Proceedings iCT, Wels, Austria, 2016.

[95] Carmignato S., Pierobon A., Rampazzo P., Parisatto M., Savio E (2012). CT for Industrial Metrology - Accuracy and structural resolution of CT dimensional measurements, Proceedings iCT, Wels, Austria, 2012.

[96] Hertz H. (1881). Über die Berührung fester elastischer Körper, Journal für die reine und angewandte Mathematik 92, 156-171

[97] Levy G. N., Schindel R., Kruth J. P. (2003). Rapid manufacturing and rapid tooling with layer manufacturing (LM) technologies. State of the art and future perspectives. CIRP Annals, 52(2): 589-609

[98] Huis in 't Veld B, et al (2015). Micro additive manufacturing using ultra short laser pulses. CIRP Annals, 64(2):701:724.

[99] Klocke F., et al (2014). Turbomachinery component manufacture by application of electrochemical, electrophysiscal and photonic processes. CIRP Annals, 63:703-726.

[100] US NIST (2013). Measurement Science Roadmap for Metal-Based AM.

[101] Thijs L., Verhaeghe F., Craeghs T., et al. (2010). A study of the microstructural evolution during selective laser melting of Ti-6Al-4V. Acta Materialia, 58(9), 3303-3312.

[102] Yadroitsev I., et al (2010). Selective laser melting technology: from the single laser melted track stability to 3D parts of complex shape. Physics procedia, 5: 551-560.

[103] Soboyejo W.O., Srivatsan T.S. (2006). Advanced Structural Materials: Properties, Design Optimization, and Applications. CRC Press, 359-400

[104] Kempen, K., Yasa, E., Thijs, L., Kruth, J.-P., Van Humbeeck, J., (2011). Microstructure and mechanical properties of Selective Laser Melted 18Ni-300 steel, Physics Procedia, Vol. 12, Part A, pp. 255-263.

[105] Vrancken B., Thijs, L., Kruth, J.-P., Van Humbeeck, J., (2012). Heat treatment of Ti6Al4V produced by Selective Laser Melting: Microstructure and Mechanical properties, Journal of Alloys and Compounds, Vol. 541(0), pp. 177-185.

[106] Vilaro, T., Colin, C., Bartout, J. D. (2011). As-Fabricated and Heat-Treated Microstructures of the Ti-6Al-4V Alloy Processed by Selective Laser Melting, Metallurgical and Materials Transactions A, Vol. 42(10), pp. 3190–3199.

[107] Kruth, J.-P., Levy, G., Klocke, F., Childs, T.H.C. (2007) Consolidation phenomena in laserand powder-bed based layered manufacturing. CIRP Annals – Manufacturing Technology, Vol. 56, pp. 730–759.

[108] Gong, H., Rafi, K., Karthik, N.V., Starr, T., Stucker, B. (2013). Defect Morphology in Ti-6Al-4V Parts Fabricated by Selective Laser Melting and Electron Beam Melting, 24rd Annual Int. Solid Freeform Fabrication, pp. 440-453.

[109] Spierings, A.B., Schneider, M., Eggenberger, R. (2011). Comparison of density measurement techniques for additive manufactured metallic parts, Rapid Prototyping Journal, Vol. 17(5), pp. 380-386.

[110] A. Slotwinski J. A., Garboczi E. J., Hebenstreit K. M. (2014). Porosity measurements and analysis for metal additive manufacturing process control. Journal of Research of the National Institute of Standards and Technology, Vol 19, pp 494-528.

[111] Wadell H. (1933). Sphericity and roundness of rock particles,The Journal of Geology, pp. 310-331.

[112] ISO 9276-6: 2008 (E) Descriptive and quantitative representation of particle shape and morphology, International Organization for Standardization, Geneva, 2008.

[113] Rothleitner C., Neuschaefer-Rube U., Illemann J. (2016). Size and shape determination of sub-millimeter sized abrasive particles with X-ray computed tomography. Proc. of 6th conference on Industrial Computed Tomograph iCT2016, Wels, Austria.

[114] http://pennstatehershey.adam.com/ (Accessed 15-10-2016)

[115] Knight S. R., Aujla R., Biswas S. P. (2011). Total Hip Arthroplasty - over 100 years of operative history. Orthop Rev (Pavia).

[116] Chang J. D. (2014). Future bearing surfaces in total hip arthroplasty. Clin Orthop Surg Vol.6:110–6.

[117] Kurtz S. M. (2004). The UHMWPE handbook: ultra-high molecular weight polyethylene in total joint replacement.

[118] Grillini L., Affatato S. (2013). How to measure wear following total hip arthroplasty. Hip Int 23:233–42.

[119] Affatato S., Zavalloni M., Spinelli M., Costa L., Bracco P., Viceconti M. (2010). Long-term in-vitro wear performance of an innovative thermo-compressed cross-linked polyethylene. Tribol Int 43:22–8.

[120] Affatato S., Bracco P., Costa L., Villa T., Quaglini V., Toni A. (2012). In vitro wear performance of standard, crosslinked, and vitamin-E-blended UHMWPE. J Biomed Mater Res A 2012;100:554–60.

[121] Gigante A., Bottegoni C., Ragone V., Banci L. (2015). Effectiveness of Vitamin-E-Doped Polyethylene in Joint Replacement: A Literature Review. J Funct Biomater 6:889–900.

[122] ISO 14242-2:2000. Implants for surgery – wear of total hip-joint prostheses – Part 2: methods of measurement, ISO, 2000.

[123] ISO 14242-2:2000. Implants for surgery – wear of total hip-joint prostheses – Part 2: methods of measurement, ISO, 2000.

[124] ISO 14242-1:2014. Implants for surgery - wear of total hip-joint prostheses - Part 1: loading and displacement parameters for wear-testing machines and corresponding environmental conditions for test, ISO, 2014.

[125] Carmignato S., Spinelli M., Affatato S., Savio E. (2011). Uncertainty evaluation of volumetric wear assessment from coordinate measurements of ceramic hip joint prostheses. Wear 270:584–90.

[126] Carmignato S., Balcon M., Zanini F. (2014). Investigation on the accuracy of CT measurements for wear testing of prosthetic joint components. Proc. of Int. Conf. on Industrial Computed Tomograph (iCT), Wels, Austria.

[127] Affatato S., Zanini F., Carmignato S. (2017). Micro X-Ray computed tomography mass loss assessment of different UHMWPE: A hip joint simulator study on standard vs. cross-linked polyethylene. PLoS ONE 12(1).

[128] RIPO. The Emilia - Romagna Register, Annual Report. Bologna: Istituto Ortopedico Rizzoli; 2012.

[129] Affatato S., Freccero N., Taddei P. (2016). The biomaterials challenge: A comparison of polyethylene wear using a hip joint simulator. J Mech Behav Biomed Mater 53:40–8.

[130] Affatato S., Zavalloni M., Taddei P., Di Foggia M., Fagnano C., Viceconti M. (2008). Comparative study on the wear behaviour of different conventional and cross-linked polyethylenes for total hip replacement. Tribol Int 41:813–22.

[131] Bland J. M., Altman D.G. (1999). Statistical Methods in Medical Research. Stat Methods Med Res 8:161–79.

[132] Shapiro S. S., Wilk M. B. (1965). An analysis of variance test for normality (complete samples). Biometrika 52:591–611.

Own publications

[I] Carmignato S., Balcon M., Zanini F. (2014). Investigation on the accuracy of CT measurements for wear testing of prosthetic joint components. Proceedings of Conference on Industrial Computed Tomography (iCT2014); 25-28 February 2014, Wels, Austria.

[II] Carmignato S., Zanini F., Balcon M., Savio E. (2014). X-ray Computed Tomography for wear measurement of prosthetic components. Proceedings of the 14th euspen International Conference; June 2014, Dubrovnik, Croatia.

[III] Kersting P., Carmignato S., Odendahl S., Zanini F., Siebrecht T., Krebs E. (2015). Analysing machining errors resulting from a micromilling process using CT measurement and process simulation. Proceedings of the 4M/ICOMM2015 Conference. Milan, Italy, 31 March - 2 April 2015.

[IV] Lutey A., Fortunato A., Carmignato S., Zanini F., Ascari A. (2015). Laser profiling of aluminum oxide grinding wheels. Proceedings of the ASME 2015 Manufacturing Science and Engineering Conference; 8-12 June 2015, Charlotte, USA.

[V] Zanini F., Hermanek P., Rathore F., Wits W. W., Carmignato S. (2015). Investigation on the accuracy of CT porosity analysis of additive manufactured metallic parts. Proceedings of International Symposium on Digital Industrial Radiology and Computed Tomography; 22-25 June 2015, Gent, Belgium.

[VI] Crema L., Lucchetta G., Zanini F., Carmignato S. (2015). Experimental Analysis of Fibers Orientation and Mechanical Properties in Injection Molding of Thermoplastic Reinforced Materials by Rapid Heat Cycle Molding. Proceedings of the Polymer Processing Society Conference 2015; 21-25 September 2015, Graz, Austria.

[VII] Lutey A., Fortunato A., Zanini F., Carmignato S., Ascari A., Liverani E., Guerrini G. (2016). Pulsed laser profiling of grinding wheels. 18th CIRP Conference on Electro Physical and Chemical Machining (ISEM XVIII). Tokyo, 19-22 April, 2016. Procedia CIRP.

[VIII] Hermanek P., Zanini F., Carmignato S., Savio E. (2016). Experimental investigations on the accuracy of X-ray computed tomography for porosity measurements of additive manufactured parts. Proceedings of the 16th euspen International Conference; May 2016, Nottingham, UK.

[IX] Rysava Z., Bruschi S. Carmignato S., Medeossi F., Savio E., Zanini F. (2016). Evaluation of Drillability of the Ti6Al4V Titanium Alloy Produced Through Additive Manufacturing. 7th HPC 2016 – CIRP Conference on High Performance Cutting, 31 May - 02 June 2016, Chemnitz, Germany. Procedia CIRP 2016.

[X] Hermanek P., Zanini F., Carmignato S., Savio E. (2016). X-ray computed tomography for additive manufacturing: accuracy of porosity measurements. Proceedings of the ASPE 2016 Summer Topical Meeting: Dimensional Accuracy and Surface Finish in Additive Manufacturing; 27-30 June, 2016, Raleigh, North Carolina, USA.

[XI] Khademzadeh S., Carmignato S., Parvin N, Zanini F., Bariani P. F. (2016). Micro porosity analysis in additive manufactured NiTi using electron microscope microscopy and micro computed tomography. Materials and Design, 90: 745–752.

[XII] Wits W. W., Carmignato S., Zanini F., Vaneker T. (2016). Porosity testing methods for the quality assessment of selective laser melted parts. CIRP Annals – Manufacturing Technology, 65(1): 201-204.

[XIII] Lutey A., Fortunato A., Zanini F., Carmignato S. (2016). Pulsed laser profiling of grinding wheels at normal and quasi-tangential incidence. Lasers in Manufacturing and Materials Processing, Vol. 3, Issue 3, pp 158–173.

[XIV] Wits W.W., Smit M., Hoen L., Carmignato S., Zanini F. (2016). Non-destructive testing of metal manufactured parts using 3D X-ray tomography. In NATO Specialists' Meeting Additive Manufacturing for Military Hardware AVT-258-RSM-042. 2016.

[XV] Affatato S., Zanini F., Carmignato S. (2017). Micro X-Ray computed tomography mass loss assessment of different UHMWPE: A hip joint simulator study on standard vs. cross-linked polyethylene. PLoS ONE 12(1).

[XVI] Zanini F., Carmignato S. (2017). Experimental investigations on the structural resolution in metrological computed tomography. Proceedings of Conference on Industrial Computed Tomography (iCT2017); 7-9 February 2017, Leuven, Belgium.

[XVII] Zanini F., Carmignato S., Savio E. (2017). Enhancing CT porosity measurements on metal additive manufactured parts. Proceedings of the 17th euspen International Conference; May 2017, Hannover, Germany.

[XVIII] Zanini F., Carmignato S., Savio E. (2017). Assembly analysis of titanium dental implants using X-ray computed tomography. Proceedings of the 17th euspen International Conference; May 2017, Hannover, Germany.

[XIX] Affatato S., Zanini F., Carmignato S. (Submitted). Quantification of wear and deformation in different configurations of polyethylene acetabular cups using micro X-ray computed tomography. Materials.

Ringraziamenti

Tre anni.

Tre anni di dottorato finiscono con questa pagina.

Tre anni sono pochi se confrontati con una vita.

Tre anni diventano importanti quando sono caratterizzanti per la tua vita.

Ringrazio per prime le persone che meriteranno sempre il primo posto: i miei genitori Nicla e Rino e mio fratello Riccardo. Il loro appoggio è stato e sarà sempre fondamentale.

Ringrazio mia nonna Tersilla che da sempre è un esempio di cosa vuol dire essere forti.

Ringrazio i miei zii Lucio e Lorena, perché so che ci saranno sempre per me.

Ringrazio gli amici veri, quelli che mi conoscono perfettamente e che mi vogliono bene per come sono.

Ringrazio Simone per essere stato il supervisore che tutti vorrebbero avere. Lo ringrazio, insieme ad Enrico, per gli insegnamenti tecnici e di vita che mi ha dato in questi anni.

Ringrazio i colleghi del laboratorio Te.Si. per il bel clima che mi hanno sempre fatto respirare. Un grazie particolare a Marco perché sa trovare sempre il modo di sdrammatizzare e farmi ridere.

Ringrazio questi tre anni per avermi fatto crescere, ma soprattutto conoscere meglio chi sono.

E, infine, ringrazio un po’ anche me stesso.